Department of Physics
Faculty of Science
University of Helsinki
Dissertationes Universitatis Helsingiensis
435/2025

# Gold Removal from E-waste by Ultrasound

Axi Holmström

ACADEMIC DISSERTATION

To be presented, with the permission of the Faculty of Science of the University of Helsinki, for public examination in the Festive Hall, University Language Centre, Fabianinkatu 26, on 17th December 2025, at 12 o'clock noon.

Helsinki 2025

**Pre-examiners**

Professor Emeritus Brutus (Pierre) T. Khuri-Yakub
Stanford University
Stanford, CA, USA

Professor Johan Carlson
Luleå University of Technology
Luleå, Sweden

**Custos**

Professor Edward Hæggström
Department of Physics, University of Helsinki
Helsinki, Finland

**Supervisors**

Professor Ari Salmi
Department of Physics, University of Helsinki
Helsinki, Finland

Professor Edward Hæggström
Department of Physics, University of Helsinki
Helsinki, Finland

**Opponent**

Professor Ayache Bouakaz
Institut National de la Santé et de la Recherche Médicale
Tours, France

Publisher: University of Helsinki
Series: Dissertationes Universitatis Helsingiensis 435/2025
Cover Image: Topi Pudas & Axi Holmström

ISBN 978-952-84-1620-3 (print)
ISBN 978-952-84-1619-7 (PDF)
ISSN 2954-2898 (print)
ISSN 2954-2952 (PDF)

Unigrafia / PunaMusta, Joensuu 2025

# Abstract

Technological development and increased digitalization of our societies have benefitted humanity immensely. Simultaneously, it has raised the demand for electronics, and hence the rare and precious metals required for their manufacture. One such metal is gold, which is becoming increasingly difficult and expensive to mine.

With increased use of electronics, more electronic waste (e-waste) is also generated – 62 Mt is generated globally each year, which is expected to increase to 82 Mt by 2030. Fortunately, e-waste is not useless. As rare and precious metals have already been concentrated into the electronics, e-waste is a valuable source for urban mining. Urban mining of gold from e-waste has already become more cost effective than virgin mining. However, current e-waste recycling methods, i.e. pyro- and hydrometallurgy, create toxic air pollutants, generate large amounts of wastewater, and require highly caustic substances. These drawbacks stem from the difficulty in separating the different metals from each other and from other non-metallic substances present in e-waste. For example, extracting gold, constituting approx. 0.1 ‰ of the mass but 60–70 % of the value in e-waste, requires, e.g., *aqua regia*.

This dissertation presents a novel and green gold recycling method for e-waste, which uses only ultrasound in water to remove gold from intact discarded printed circuit boards (PCBs). High-intensity focused ultrasound (HIFU) generates cavitation erosion to remove the gold. Due to the focusing of HIFU, material is removed only from the gold pads, not the adjacent fibreglass-epoxy substrate. The PCB can be imaged with the same HIFU transducer to locate the gold pads prior to gold removal. The first proof-of-concept of gold removal by HIFU was presented in paper A. This was followed by a more detailed study, paper I, which showed that the erosion depth could be controlled by the number of sonicated bursts. In paper II, improving the gold removal efficiency by a factor of 4.6 was achieved by decreasing the HIFU frequency from 11.8 MHz to 4.2 MHz. The HIFU method was also tested for machining of aluminium (papers B, C). Quantifying the removal volumes was done by a custom-built coded-excitation scanning acoustic microscope (CESAM). In paper III, the more extensive imaging capability of CESAM was demonstrated on a complex and soft sample: partially ossified bioactive-glass bone implants in rabbit bone.

With e-waste piling up and natural gold reserves running out, the presented gold removal method is a contribution towards a solution for both. While traditional e-waste recycling methods exist, they pose both environmental and occupational safety hazards. Thus, the presented HIFU method, using only ultrasound and water, represents a step towards a truly green and sustainable gold recycling technology for e-waste.

# Acknowledgements

The work constituting this dissertation was carried out at the Electronics Research laboratory (ETLA), at the Department of Physics, Faculty of Science, University of Helsinki. The work was funded by the Research Council of Finland (grants 347459, 349200). I extend my gratitude to all the aforementioned parties, who made this work possible. I also thank The Swedish Cultural Foundation in Finland, which granted me several years of funding for another project during my doctoral studies.

My journey towards a PhD has been long and fraught with mishaps, unforeseen delays, and a few too many restarts. But as they say, it is not the destination, but the journey that matters. And while the journey has been long, it has definitely been worth taking. During my time as a doctoral researcher in ETLA, I have experienced some incredible highs and met amazing people – not to mention all the physics I have seen, worked with, and learnt.

Throughout my PhD journey, only one thing has remained truly constant, my supervisor Prof. Edward Hæggström. He welcomed me to ETLA as a young second-year physics student. Ever since then, he has been a true mentor, teaching me not only physics, but many other skills as well. Despite Edward making the transition to become CEO of the start-up Nanoform Finland, and consequently decreasing his hours at the University, he has always found time for me. He gladly read and commented on my articles, this dissertation, and shared his insight on any troubling matter (physics or otherwise) throughout the years. I am truly grateful – for everything.

My other supervisor, Prof. Ari Salmi, has also accompanied me on this journey from the very beginning, but not always as a supervisor. When I came to the lab, I was lucky to befriend then M.Sc. Ari Salmi, whose own doctoral defence was the first one I experienced. We have walked our own, but often entwined, ETLA-paths together for 13 years, supporting each other in our endeavours. I am particularly grateful for your decision to move me to my current team (UIMAS-FUSUMIN) and task, i.e., material removal with ultrasound. Without that, this book would not exist.

Throughout the years I have worked with many amazing people. I cannot fit a comprehensive list into this acknowledgement, but I will name a few.

First, my sincerest thanks to the UIMAS-FUSUMIN team, with whom it has been a pleasure to delve into the world of ultrasound and cavitation. I owe so much to you, especially Mr. Topi Pudas, Mr. Jere Hyvönen, Mr. Tom Sillanpää, and Mr.

Joni Mäkinen. You are incredible physicists and our discussions on physics and anything else have made the days much brighter. Without Messrs. Pudas and Hyvönen the gold removal setup in this dissertation would not exist. Thank you! I am also grateful to Dr. Martin Weber, who has kindly helped out anytime possible.

I also wish to thank previous colleagues, who have since moved on from ETLA: Mr. Antti Meriläinen, Mr. Tuomo Ylitalo, Mr. Joonas Mustonen, and Dr. Daniel Veira Canle. Thank you all for many fruitful discussions and peer support! Antti took me under his wing when I joined ETLA, taught me a myriad of skills and helped me with anything and everything – literally, as the breadth of his skills continues to amaze me. Antti and Tuomo, I consider myself lucky to have you as close friends.

Naturally, I am also grateful to all other colleagues who have shaped me as a researcher: all my co-authors (in papers both included in and excluded from this thesis), Doc. Ivan Kassamakov, and my second supervisor during many thermoacoustic years, Dr. Markus Aicheler.

I also want to express my gratitude to the pre-examiners of this dissertation, Prof. Em. B. (Pierre) T. Khuri-Yakub and Prof. Johan Carlson, and to Prof. Ayache Bouakaz for agreeing to act as my opponent.

Special thanks are directed to the people in my life who, at an early stage, inspired me to learn and seek more knowledge. In primary school, Natalie Nylund, my friend since kindergarten, always wanted to study for tests with me. In upper secondary school, I met my friends – now Drs. – Kim Pöyhönen and Henri Puttonen, who have continued to provide friendship and spurred me on towards new challenges. Our physics teacher Jonas Waxlax was the one who inspired me to study physics. But ultimately, my eagerness to learn new things has its roots in my now deceased father, Peter Holmström. From a very early age, he made acquiring knowledge fun. For this, I owe an enormous debt to him.

At the end of the day, research is only one aspect of life. All my friends, relatives, the people close to me, and the wonderful people in the reservist/defence community, have given me strength and joy through the highs and lows of my PhD journey. Thank you to all of you!

Last but not least, my deepest gratitude goes to my family. My mother Åsa Nordlund has actually read all my articles, despite having no background in natural sciences. That is one small example of how she has shown her interest and support throughout my life. And to my husband Jere, thank you for being so incredibly wonderful. Even during the most stressful and dismal days, your support and love have filled me with calm, hope, and happiness. Thank you for making every day of my life better.

Helsinki, October 17th, 2025

Axi Holmström

# Contents

# List of abbreviations and symbols

**Abbreviations:**

| | |
|---|---|
| BAG | bioactive glass |
| CaP | calcium phosphate |
| CESAM | coded-excitation scanning acoustic microscopy/microscope |
| CT, µCT | computed tomography, micro-computed tomography |
| DES | deep eutectic solvent |
| EHG | electroplated hard gold |
| e-waste | electronic waste |
| FWHM+ | positive-pressure-amplitude full-width half-maximum |
| FWHM− | negative-pressure-amplitude full-width half-maximum |
| HA | hydroxyapatite |
| HIFU | high-intensity focused ultrasound |
| PCB | printed circuit board |
| PMMA | poly(methyl methacrylate), i.e. acrylic |
| PRF | pulse repetition frequency |
| RF | radio frequency |
| RPM | rare and precious metals |
| ROI | region-of-interest |
| SAM | scanning acoustic microscopy/microscope |
| SD | standard deviation |
| SEM-EDX | scanning electron microscopy with energy dispersive x-ray spectroscopy |
| Si | silica |
| SLR | side-lobe ring |
| SNR | signal-to-noise ratio |
| SWLI | scanning white light interferometry |
| ToF | Time-of-Flight |

**Symbols:**

| | |
|---|---|
| $\gamma$ | ratio of specific heats of the gas; standoff distance $d/R_{max}$ |
| $\lambda$ | wavelength |
| $\mu$ | dynamic viscosity of the liquid |
| $\rho$ | density |
| $\sigma$ | surface tension of the liquid |
| $\omega$ | angular frequency |
| $\omega_0$ | angular resonance frequency of a bubble |
| | |
| $A$ | area |
| $c$ | speed of sound |
| $C$ | stiffness |
| $d$ | distance between bubble centre and wall |
| $E$ | Young's modulus |
| $f$ | frequency |
| HK | Knoop hardness |
| HV | Vickers hardness |
| $m$ | mass |
| $P_0$ | hydrostatic/ambient pressure |
| $p(R)$ | pressure at the bubble-liquid interface |
| $p_\infty$ | pressure far away from the bubble |
| $P_v$ | vapour pressure of the liquid |
| $p_S(t)$ | time-dependent pressure of a sound wave |
| $P_A$ | positive pressure amplitude of a sinusoidal sound wave |
| $P_{Blake}$ | Blake threshold |
| $P_{B,min}$ | minimum liquid pressure at the bubble wall |
| $P_{reflected}$ | pressure amplitude of the reflected wave |
| $P_{transmitted}$ | pressure amplitude of the transmitted wave |
| $P_{PPP}$ | peak-positive-pressure |
| $P_{PNP}$ | peak-negative-pressure |
| $R$ | radius of bubble or coordinate for the bubble-liquid interface |
| $R_0$ | initial bubble radius |
| $R_{max}$ | maximum bubble radius |
| $\dot{R}$, $\ddot{R}$ | first and second time derivative of the radius (number of dots denotes the order of the derivative) |
| $R_P$ | reflection coefficient of pressure amplitude |
| $t$ | time |
| $T_0$ | initial ambient temperature |
| $T_{max}$ | maximum temperature inside bubble |
| $U_{PP}$ | peak-to-peak voltage |

| | |
|---|---|
| $V$ | volume |
| $V_{fa}$ | volume loss rate by fatigue fracture |
| $Z$ | acoustic impedance |
| $Z_X$ | acoustic impedance of X |

# List of original publications

This dissertation is based on the following publications:

I A. Holmström, T. Pudas, J. Hyvönen, M. Weber, K. Mizohata, T. Sillanpää, J. Mäkinen, A. Kuronen, T. Kotiaho, E. Hæggström, and A. Salmi, "Gold removal from e-waste using high-intensity focused ultrasound", *Ultrasonics Sonochemistry* 111, 107109 (2024).

II T. Pudas, A. Holmström, J. Hyvönen, T. Sillanpää, J. Mäkinen, M. Weber, K. Mizohata, A. Kuronen, T. Kotiaho, E. Hæggström, and A. Salmi, "Effect of HIFU frequency on gold removal efficiency from e-waste", submitted.

III A. Holmström, A. Meriläinen, J. Hyvönen, A. Nolvi, T. Ylitalo, K. Steffen, R. Björkenheim, G. Strömberg, H. J. Nieminen, I. Kassamakov, J. Pajarinen, L. Hupa, A. Salmi, E. Hæggström, and N. C. Lindfors, "Evaluation of bone growth around bioactive glass S53P4 by scanning acoustic microscopy co-registered with optical interferometry and elemental analysis", *Scientific Reports* 13, 6646 (2023).

**Peer-reviewed conference proceedings:**

A A. Holmström, T. Pudas, J. Hyvönen, T. Sillanpää, P. Lassila, J. Mäkinen, K. Mizohata, A. Kuronen, T. Kotiaho, A. Salmi, and E. Hæggström, "Identifying regions-of-interest and extracting gold from PCBs using MHz HIFU", 2022 IEEE International Ultrasonics Symposium (IUS), Venice, Italy, 10-13 October 2022, doi: 10.1109/IUS54386.2022.9957863.

B J. Hyvönen, A. Holmström, T. Pudas, T. Sillanpää, P. Lassila, J. Mäkinen, A. Kuronen, T. Kotiaho, A. Salmi, and E. Hæggström, "Focused-ultrasound-induced cavitation removes material in a controlled fashion", 2022 IEEE International Ultrasonics Symposium (IUS), Venice, Italy, 10-13 October 2022, doi: 10.1109/IUS54386.2022.9957310.

C T. Pudas, J. Hyvönen, A. Holmström, T. Sillanpää, P. Lassila, J. Mäkinen, A. Kuronen, T. Kotiaho, A. Salmi, and E. Hæggström, “Machining of aluminium with MHz high-intensity focused ultrasound”, 2022 IEEE International Ultrasonics Symposium (IUS), Venice, Italy, 10-13 October 2022, doi: 10.1109/IUS54386.2022.9957698.

The publications are referred to in the text by their roman numerals or capital letters.

## Author’s contributions

I The author planned and performed all gold erosion measurements, analysed all data, and performed all calculations. The author wrote the first draft of the article and edited it for final publication as corresponding author.

II The author and T. Pudas planned the experiments, and the author contributed to analysing and interpreting the results. The author supervised the M.Sc. thesis of T. Pudas, which formed the basis of this publication. The author also contributed to reviewing and editing the first draft of the manuscript before reviewing it with the other co-authors for submission.

III The author compiled and co-registered the measurement data from all three imaging modalities (coded-excitation scanning acoustic microscopy, scanning white light interferometry, scanning electron microscopy with energy dispersive x-ray spectroscopy), analysed and interpreted the results, and drew the conclusions. The author wrote the first draft of the manuscript and edited it for final publication as corresponding author.

A The author planned the experiments, performed all analyses, wrote the first draft of the manuscript, and edited it for final publication. The author gave an oral presentation at the IEEE International Ultrasonics Symposium (IUS), Venice, Italy, on 13 October 2022.

B The author supervised the M.Sc. thesis of J. Hyvönen, which formed the basis of this publication. In that capacity, the author contributed to planning the experiments, analysis, and presentation of results. The author also contributed to writing the first draft of the manuscript and subsequently reviewed it with the other co-authors.

C The author supervised the work and contributed to planning experiments and presentation of results. The author also contributed to writing the first draft of the manuscript and subsequently reviewed it with the other co-authors.

# 1 Introduction

To most people, ultrasound is an imaging method, familiar particularly from obstetrics. However, this is a very narrow view of the vast field of ultrasonic applications that exist today. Ultrasound is basically a pressure wave with a frequency exceeding 20 kHz. In broad terms, it can be used in solids, liquids, and even gases. Like light with a magnifying glass, ultrasound can be focused, but it can also be scattered from smaller particles, like light from e.g. smoke.

The main aim of this dissertation is to remove gold from electronic waste using only ultrasound – quite a jump from the mental picture of fetal images. This is, however, not as far-fetched as it appears at first glance; the field of ultrasonics is often divided roughly into these two very different purposes, sensing (imaging) and actuation. In ultrasonic imaging, the aim is to non-destructively characterise a sample (material, structure, body part, etc.), while in ultrasonic actuation the aim is to affect the sample in some desired way, e.g. by breaking, heating, melting, etc. In some cases, imaging and actuation can both be performed with one single setup. Such is the versatility of ultrasound.

In this dissertation, actuation and imaging both play a role. First, a novel application of ultrasonic actuation is demonstrated: removing gold from electronic waste (e-waste) for recycling purposes, using only ultrasound-induced cavitation without any added chemicals (papers A, I, II). Imaging with this setup is also shown, as the actuating transducer was used to acoustically image and locate the gold pads prior to gold removal. The applicability of the same method also for aluminium erosion and engraving is presented (papers B, C). To quantify the erosion holes and determine amount of removed gold or aluminium, a coded-excitation scanning acoustic microscope (CESAM) constructed in our laboratory was used. While erosion holes on a metal surface are simple to image, the more extensive capability of the CESAM is demonstrated in this dissertation on a complex and soft sample as well: partially ossified bioactive-glass bone implants in rabbit bone (paper III). This division into actuation and imaging is approximately followed throughout the chapters of this dissertation.

# 1.1 Gold removal from e-waste with ultrasound

## 1.1.1 E-waste and current gold recycling methods from e-waste

Current technological development, especially related to increased digitalization, has raised the demand for electronics and electronic devices. While this development has benefitted mankind tremendously, it has also generated a problem: In 2022, 62 Mt of e-waste was created globally, which is expected to rise to 82 Mt per year by 2030 [1]. Of the 62 Mt of e-waste generated in 2022, only 22 % (13.8 Mt) was properly recycled, with the recycling rate not keeping pace with e-waste generation [1]. While this development sounds bleak, there is a silver lining – as e-waste contains rare and precious metals (RPMs), e.g. gold, silver, and platinum, it has become a resource for urban mining [2]. Urban mining of e-waste has become more cost-effective than virgin mining [3], because the RPMs are already concentrated in the e-waste. For example, 1 t of e-waste contains the same amount of gold as 17 t of mineable ore [4].

While e-waste is piling up, natural gold reserves are running out. With approximately 64 000 t of unmined natural gold reserves and an annual global mining rate of approx. 3 300 t, mineable gold would run out in 20 years [5]. Currently, only about 25 % of annual gold production is from recycled sources [6], of which less than 5 % comes from e-waste [7]. Hence, there is both an economic and environmental benefit to urban mining of gold from e-waste.

Electronics are typically built on printed circuit boards (PCBs). PCBs contain mostly copper and a fibreglass-epoxy substrate, but also other elements, depending on the intended use and components. For example, gold is used in PCBs due to its corrosion resistance and high electrical conductivity. It is often used in gold pads in connectors (Figure 1a) and other surface elements that must be durable and conductive. Gold connectors have a layered structure with a copper bulk, a nickel layer (typically 3–6 µm thick) coated on the copper for durability, and then a thin gold layer (1–2 µm, or even less in certain types of gold pads) applied on top (Figure 1b).

Despite the low mass content of gold in PCBs (only 0.11 ‰), it still constitutes 66 % of the monetary value [8], making it well worth recycling. Unfortunately, current recycling methods, while more environmentally friendly than virgin mining, still have significant drawbacks. These stem from the difficulty in extracting gold – a noble metal – from a mixture of copper (and small amounts of other metals) and non-metallic substances, such as fibreglass and resin from the PCB substrate and plastics from component casings.

Figure 1 a) A discarded PCB with gold connectors. b) Schematic of the structure of a single gold pad (cross-section, not to scale). The thin gold layer is typically 1–2 µm thick and the nickel layer beneath 3–6 µm thick.

Current e-waste recycling is usually a three-step process: mechanical preprocessing, pyrometallurgy, and hydrometallurgy [2, 8, 9]. In mechanical preprocessing, valuable components (containing RPMs) are manually removed and PCBs are ground for further processing. In pyrometallurgy, the non-metallic elements are burnt off, but the remaining metals still need to be separated. The separation of metals is achieved through hydrometallurgy; desired metals are leached in a sequential manner. Unfortunately, pyrometallurgy creates toxic and volatile air pollutants in addition to large amounts of $CO_2$ [2, 9, 10]. Further, hydrometallurgy typically requires toxic or highly corrosive substances, e.g. piranha solution (a mixture of sulfuric acid and hydrogen peroxide, $H_2SO_4/H_2O_2$), cyanide, or *aqua regia*, whose safe and proper handling is difficult and creates large amounts of wastewater [2, 8, 10].

New, greener methods for gold recycling from e-waste are being developed. In bioleaching, microorganisms (e.g. cyanobacteria, fungi, algae) are used to extract gold [2, 8, 11]. While promising in lab scale, the bioleaching process is slow and sensitive. The microorganism populations are selective, i.e., one population recovers one substance, and the process can halt unexpectedly, as the microorganisms can perish from toxic substances generated in the leaching process [11]. More environmentally friendly solvents are also being developed, of which deep eutectic solvents (DES) have shown promise [10, 12]. DES, however, have long leaching times and high viscosity, thereby requiring higher temperatures than inorganic acids [12].

In an effort to speed up RPM recycling from PCBs using DES, a recent study applied a 20 kHz sonotrode [13]. In this manner, they managed to accelerate the process by a factor of 30 [13]. The sonotrode creates cavitation, i.e. imploding microbubbles, which in turn generate local high pressures, temperatures, and free radicals [14, 15]. Cavitation could therefore be a solution to more environmentally friendly gold recycling from e-waste.

### 1.1.2 Cavitation

Cavitation is a phenomenon in which small bubbles (nm–mm size) are formed in a liquid as a result of a decrease in pressure [14, 16]. A layman might be familiar with hydrodynamic cavitation, where, for example, cavitation bubbles created in high-speed flows in propellers cause reduced propulsion efficiency and even damage to the propeller blades. This phenomenon was discovered and discussed already in 1895 by Thornycroft & Barnaby, as they observed an unexpected inefficiency in propeller propulsion in the new *Daring*-class torpedo-boat destroyers [17]. Research into erosion of propeller blades and its causes was begun by Silberrad in 1912, as he investigated damage to propellers of the ocean liners *Mauretania* and *Lusitania*, specifically the effect of propeller materials on the observed damage [18].

Another type of cavitation is acoustic cavitation, where a sufficiently strong sound field in a liquid creates and interacts with bubbles. Sound (and ultrasound) is, at its core, pressure oscillations, causing a decrease in pressure during the rarefaction phase of the wave. As only acoustic cavitation was employed in this dissertation, further discussion about cavitation will refer to acoustic cavitation, unless explicitly stated otherwise.

Cavitation can be divided into two types, stable and transient cavitation, whose behaviour and effect on their surroundings differ. In stable cavitation, a bubble is formed, grows moderately, and subsequently pulsates in a stable manner with the pressure oscillations from the sound wave. The shear forces and microstreaming created around stable cavitation bubbles have been used e.g. in the medical field to improve drug delivery through the cell membrane [19] and the blood-brain barrier [20]. In transient cavitation, on the other hand, the bubble grows rapidly until it can no longer be sustained and subsequently collapses. This collapse can create very localized (in the order of the bubble size) and very high pressures and temperatures (thousands of kilopascals and kelvins), resulting in shock waves [14, 15, 21]. Transient cavitation can thus cause damage to materials, either detrimentally or – if used on desired surfaces – beneficially.

When using high-intensity focused ultrasound (HIFU), the rarefaction pressures at the focus can be sufficient to cause transient cavitation. Furthermore, a cloud of micrometer-sized bubbles is formed at the focus, which not only interact with and collapse due to the ultrasonic field, but are also affected by interactions with and collapses of neighbouring bubbles. The dynamics of cavitation clouds have thus been called “deterministically chaotic” by Lauterborn & Mettin [22, 23]. This term underlines that the sound field is deterministic, but the cloud dynamics can only be described statistically (i.e., it is stochastic) and cannot be described by simple analytical expressions. However, Apfel famously formulated three golden rules as a guide for any experimentalist attempting to determine when cavitation might occur: “know thy liquid”, “know thy sound field”, and “know when something happens” [21, 24]. These rules encompass the many factors affecting cavitation:

amount of dissolved gas in the liquid, size distribution of existing bubbles, size and spatial distribution of bubble nucleation sources (small particles), temperature, viscosity, surface tension, sound frequency, pressure amplitude, and pulse duration – to name a few.

Despite the complexity of cavitation clouds, theoretical frameworks have been created for single bubbles to gain at least some insight into cavitation. An early description of the dynamics of a single cavitation bubble was supplied in 1917 by Lord Rayleigh [25]. He assumed a spherical empty cavity in an infinite homogeneous incompressible liquid and derived an expression for the movement of the bubble surface, at radius $R$, depending on a static pressure far away from the bubble, $p_\infty$. Plesset expanded on this work in 1949 and included the pressure at the bubble wall, $p(R)$, which he defined as $p(R) = P_v - \frac{2\sigma}{R}$ , with $P_v$ being the vapour pressure of the liquid and $\frac{2\sigma}{R}$ the Laplace pressure, caused by the surface tension, $\sigma$, of the liquid [26]. This yielded the famous Rayleigh-Plesset equation for a single cavitation bubble:

$$\frac{3\dot{R}^2}{2} + R\ddot{R} = \frac{p(R) - p_\infty}{\rho} \qquad (1)$$

where $\dot{R}$ and $\ddot{R}$ are the first and second time derivatives of $R$, respectively, and $\rho$ is the density of the liquid.

Further developments of the Rayleigh-Plesset equation to include a time-varying acoustic field $p_S(t) = P_A \sin(\omega t)$ and the accompanying variations in gas pressure inside the pulsating bubble were made by Noltingk & Neppiras in 1950 [27]. ($P_A$ is the positive pressure amplitude of the sinusoidal acoustic wave with angular frequency $\omega = 2\pi f$, $f$ is frequency.) This gives the pressure far away from the bubble as $p_\infty = P_0 + p_S(t)$, with $P_0$ as the hydrostatic pressure. The viscosity of the liquid was added by Poritsky in 1951 [28, 29]. Combining these works yields the Rayleigh-Plesset equation in the form found today in topical textbooks (a clear and thorough derivation can be found in, e.g., [16]):

$$R\ddot{R} + \frac{3}{2}\dot{R}^2 = \frac{1}{\rho}\left[\left(P_0 + \frac{2\sigma}{R_0} - P_v\right)\left(\frac{R_0}{R}\right)^{3\gamma} + P_v - \frac{2\sigma}{R} - \frac{4\mu}{R}\dot{R} - P_0 - p_S(t)\right] \qquad (2)$$

where $R_0$ is the initial bubble radius, $\gamma$ is the ratio of specific heats of the gas, and $\mu$ is the dynamic viscosity of the liquid. As this equation still contains simplifications, more complex equations have also been developed including e.g. the compressibility of the liquid and enthalpy. Derivations and historical details on these can be found in, e.g., [30, 31].

In acoustic transient cavitation, where a bubble cloud is always formed, the details of single-bubble dynamics are of diminishing importance. Of more interest is to obtain some sense of when transient cavitation can be initiated. To achieve transient cavitation, the bubbles must reach unbounded growth caused by the rarefactive pressure of the wave. To describe this pressure threshold, the first calculations for a single quasi-static bubble were made by Blake in 1949 [32], yielding the Blake threshold:

$$P_{Blake} = P_0 - P_{B,min} = P_0 - P_v + \frac{4\sigma}{3}\sqrt{\frac{2\sigma}{3R_0^3\left(P_0+\frac{2\sigma}{R_0}-P_v\right)}} \tag{3}$$

where $P_{B,min}$ is the minimum static pressure at the bubble wall from which a further decrease in pressure will cause unbounded bubble expansion.

To calculate the Blake threshold, the initial bubble radius, $R_0$, is needed. In 1933, Minnaert discovered that a bubble tends to oscillate with a resonance frequency dependent on its size [33]. He formulated the following simple relationship between the angular resonance frequency, $\omega_0$, and bubble size, $R_0$:

$$\omega_0 = \frac{1}{R_0}\sqrt{\frac{3\gamma P_0}{\rho}} \tag{4}$$

This simple expression is useful and can be used the other way around, i.e., to calculate the initial size of bubbles most likely to cavitate (i.e., having a lower threshold) in a sound field of a certain frequency.

More detailed cavitation thresholds accounting for the frequency dependence of the bubble expansion, and thus very relevant for acoustic cavitation applications, have been calculated by Apfel [34, 35] and Holland & Apfel [36]. The frequency dependence arises because a higher frequency has a shorter rarefaction phase, which thus allows a shorter growth phase of the bubble before the pressure begins to increase and compress the bubble again. Hence, higher frequencies require higher pressure amplitudes to cause the unbounded growth in transient cavitation. The cavitation threshold calculated chiefly according to [36] for select frequencies are shown in Figure 2 (details about the calculation are given in Appendix 1, the maximum temperature inside the bubble is calculated as in [37], instead of assumed to be 5000 K as in [36]). The resonance sizes calculated according to Equation 4 are also shown, which correspond well to the initial bubble sizes with minimum cavitation thresholds. Frequencies 4.2 MHz, 7.3 MHz, and 11.8 MHz were used in paper II, 11.8 MHz in papers I, A, B, and C, 1 MHz and 20 kHz are shown for comparison. Many HIFU applications operate in the low MHz-range. The lower limit for ultrasonic frequencies is defined as 20 kHz and it is often used in sonotrodes, as was the case in [13], where a sonotrode was used to speed up RPM recycling in DES. As shown, the pressure threshold for bubbles with initial radii below 2 µm does not change significantly for frequencies below 1 MHz.

While graphs such as Figure 2 provide valuable insight, they still only describe a single bubble. To describe cavitation clouds, numerical methods are needed, with works existing in the literature (e.g., [38-40]). However, for practical acoustic cavitation applications, an empirical approach is often sufficient to determine suitable sonication parameters to achieve transient cavitation.

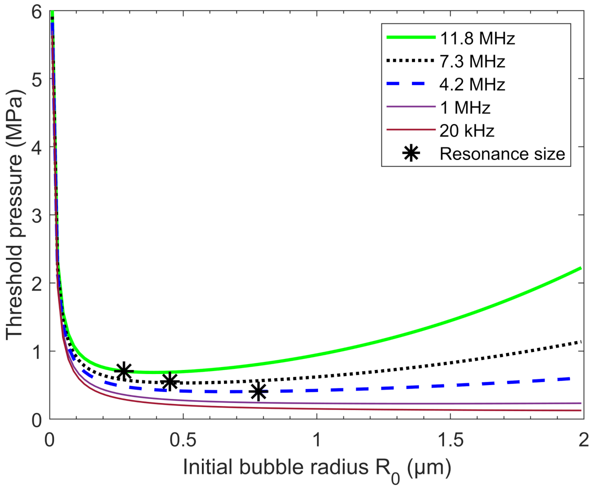

Figure 2 Cavitation thresholds in water as a function of initial bubble radii for select frequencies. Frequencies 4.2 MHz, 7.3 MHz, and 11.8 MHz were used in papers I, II, A, B, and C, 1 MHz and 20 kHz are shown for comparison. The cavitation threshold increases with frequency. Resonance sizes calculated with Equation 4 are shown with asterisks (not shown for 1 MHz and 20 kHz, out of range).

### 1.1.3 Cavitation erosion

When bubbles collapse, they emit a shock wave, which can damage materials. Qualitatively, the strengths of the collapse and subsequent shock wave depend on the final bubble radius: The larger the bubble has grown, the more energetic the collapse [41]. However, shock waves is not the only cavitation erosion mechanism. If the collapsing bubble is near a solid wall (or some other boundary), the collapse becomes asymmetric, resulting in not only a shock wave, but a water jet (microjet) towards the surface (Figure 3). The asymmetric collapse is caused by a pressure difference between the opposite sides of the bubble: The bubble partially reflects incoming sound, causing a lower pressure between the bubble and the solid wall. This pressure difference causes the bubble to collapse in on itself, creating a microjet towards the solid surface.

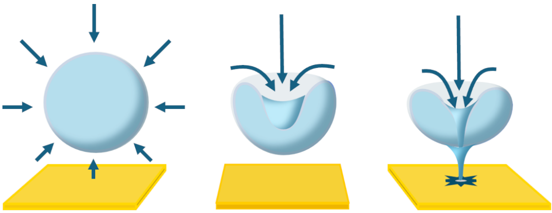

Figure 3 Asymmetric cavitation bubble collapse near a solid wall. The pressure farther away from the bubble becomes higher than that between the bubble and the surface, forcing the bubble in on itself, causing a microjet towards the surface. Drawing courtesy of Topi Pudas.

When the bubble collapse is violent enough, both the shock wave and the microjet can contribute to erode the solid surface. Determining the dominating erosion mechanism has been an ongoing discussion in the literature for several decades since the first proposal of eroding microjets by Kornfeld & Suvorov in 1944 [42]. For example, in 1986 Karimi & Martin [43] discussed both phenomena and their relative strengths as a function of standoff distance $\gamma = d/R_{max}$ ($d$ is the distance from the bubble centre to the wall, $R_{max}$ maximum bubble radius). In that same year, Tomita & Shima postulated that erosion was caused mainly by the microjet, and that observed ring-like erosion marks were created by tiny bubbles imploding in the bubble torus, which remains after the microjet has penetrated the initial bubble [44]. However, Philipp & Lauterborn refuted the microjet hypothesis in 1998 [45]. They measured the impact velocities of microjets from bubbles at different standoff distances and concluded that only for bubbles already in contact with the wall at the moment of collapse could the microjet cause erosion. They did, however, determine that tiny bubbles in the torus can indeed collapse almost simultaneously, producing shock waves and erosion marks. However, they pointed out and showed that also shock waves from the collapse of the main bubble cause erosion. The discussion about the dominant erosion mechanism has continued back and forth until the present day (see e.g. [46-48]), but as both microjets and shock waves are detected in the same experiments, the discussion seems to converge towards a consensus that both shock waves and microjets can play a role. This is especially true in acoustic cavitation, where bubble clouds are formed instead of single bubbles, with microjets and shock waves from collapsing bubbles interacting in complex ways (e.g. [49, 50]).

Regardless of dominant erosion mechanism, cavitation erosion has found practical applications, mainly in the field of medicine. Especially using HIFU in the low MHz-range has found uses in histo- and lithotripsy to break tissues and calculi (see e.g. [21, 51-55]). Cavitation erosion on harder materials, e.g. metals, alloys, composites, etc., has also been studied extensively. However, cavitation erosion of hard materials occurs most commonly as an undesired side effect in mechanical parts subjected to hydrodynamically cavitating flows, e.g., in propellers and pumps. Hence, much of the literature is focused on hydrodynamic cavitation, which causes very different damage than acoustic cavitation. As Karimi & Martin stated already in 1986 in their comprehensive review paper on cavitation erosion of different materials, “it appears difficult to compare the erosion curves of different types of cavitation” [43]. Hence, research relevant for determining the effect of acoustic cavitation on metals is restricted to single-bubble erosion studies (e.g. [44-46, 56]) or acoustic cavitation erosion studies (e.g. [48, 57-59]).

Despite the myriad of research on cavitation erosion of metals, practical applications of controlled metal removal with acoustic cavitation have yet to become widely available. There are, however, two recent studies on utilizing 20 kHz sonotrodes for metal recovery from e-waste: Jacobson *et al.* sped up the metal recovery from PCBs in DES 30-fold by adding the sonotrode [13] and Watt *et al.* removed gold nanoparticles from a SIM card in a two-surfactant system [60]. Alas, a sonotrode has poor spatial resolution, as the cavitation bubbles are created beneath the tip, which in both [13] and [60] was 6.4 mm wide. While this was sufficiently narrow for a SIM card, whose surface consists almost exclusively of gold, it is much too wide for gold connectors on PCBs (approx. 1 mm wide), as the PCB substrate would also be removed. It is also difficult to control the erosion depth using a sonotrode, which in [13] led to removal of not only gold, but the metal layers beneath (nickel, copper) as well. Removing the substrate and/or metals beneath the gold again necessitates additional separation steps. Thus, a more selective approach would be needed.

### 1.1.4 Controlled metal removal with HIFU-induced cavitation erosion

Unlike a sonotrode, HIFU uses a highly focused acoustic field (focal widths usually in the range of hundreds of µm to a few mm). By focusing the acoustic energy, high intensities (> 1 W/cm$^2$) are achieved at the small focus, but not in the intermittent medium in the near field. This is why HIFU has achieved such widespread medical use – one can use an extracorporeal transducer to affect a small area inside the body, without causing damage to the intervening tissue. Due to the tight focusing, HIFU-induced cavitation can be localized to desired regions also in other applications, e.g. by focusing sound onto the gold connectors on PCBs. That is what was done in the research of this dissertation: HIFU-induced cavitation erosion was used on PCBs in water immersion to remove the gold, without any added chemicals (papers A, I, II). The same method was also used to erode aluminium samples, including machining (papers B, C). Compared to other micromachining techniques, HIFU has the benefit of being contactless (i.e. no wearing of mechanical parts), inexpensive, suitable for thermally sensitive materials, and requiring no chemicals or slurries.

The tight focus of the HIFU transducer has the added benefit of enabling imaging (at low power levels). In papers A, I, and II, the PCB samples were imaged with the HIFU transducer prior to gold removal in order to locate the gold pads. This mitigates the problem with sonotrodes: Using HIFU, gold pads can be located and subsequently chiefly the gold layer can be removed, decreasing or even eliminating the need for further post processing. As HIFU-induced metal erosion can be performed in water, it could constitute a new, greener, and cleaner e-waste recycling method.

## 1.2 Coded-excitation scanning acoustic microscope (CESAM)

To quantify the gold removal in papers A and I, and the aluminium erosion in B and C, an in-house built coded-excitation scanning acoustic microscope (CESAM) was used. While the technical specifications and resolution of our CESAM has been previously reported on USAF resolution samples [61], its use on a complex sample, containing both soft and hard substances, was also explored in this dissertation to cement our confidence in its imaging capability: partially ossified bioactive-glass bone implants in rabbit bone (paper III). The ability to image soft samples with CESAM is not only relevant for biological applications. As flexible electronics are becoming more common in e.g. displays, smart phones, e-textiles, and biometrics, a need to quantify gold removal from soft substrates might also arise. Gold is used in flexible electronics as interconnects between device components [62]. While flexible electronics currently comprise only 3.6 % of the market share of consumer electronics [63, 64], it is a rapidly growing market expected to double in size to US$71 billion by 2032 [63].

Bone substitutes are needed in orthopaedic surgery in cases where bone tissue is missing beyond the bone's healing abilities. Autografts and allografts are still commonly used, but synthetic bone substitutes have the benefit that they do not require sourcing from a body. One synthetic bone substitute is bioactive glass (BAG), which has proven bone bonding, osteoconductive, and osteostimulative properties [65]. After implantation of BAG, a thick silica-rich (Si-rich) layer forms rapidly, onto which calcium phosphate (CaP) nucleates and crystallizes to form hydroxyapatite (HA) [66]. Bone formation occurs gradually on top of the HA-layer, which in time results in bone ingrowth, finally replacing the bone substitute with new bone.

X-rays or computed tomography (CT) are commonly used to evaluate bone healing, but during the bone ingrowth around BAG, the formed HA-layer resembles bone mineral, thus providing poor X-ray contrast. Furthermore, as new bone forms and the bone substitute disappears, the treated region appears ever denser on X-rays, complicating the evaluation of the extent of bone remodelling. To further obfuscate matters, elastic properties of bone do not correlate significantly with bone mass density, determined from degree of mineralized bone measured by µCT [67, 68]. Fortunately, acoustic impedance, measured by scanning acoustic microscopy (SAM), is a more reliable measure [67, 68].

In SAM, a short, highly focused, low-power high-frequency (typically 10 MHz – 2 GHz [67, 69-71]) acoustic wave is transmitted towards a sample. The wave is reflected and the reflected echo recorded. This is done at each measurement point across the sample. The Time-of-Flight (ToF), i.e., the time between transmission and reception of the echo, determines the distance between the transducer and the sample. This information can be used to construct a topography map of the sample surface. Simultaneously, the change in amplitude of the reflected wave provides information about the elastic properties of the sample, or more specifically, the mismatch in acoustic impedance, $Z$, between the imaging medium (usually water, $Z_{water}$ = 1.5 MRayl) and the sample, $Z_{sample}$. At normal incidence of the wave in water immersion (and without scattering from the sample surface), the reflection coefficient of pressure amplitude, $R_P$, i.e., the ratio of the reflected pressure amplitude to transmitted pressure amplitude, is:

$$R_P = \frac{P_{reflected}}{P_{transmitted}} = \frac{Z_{sample} - Z_{water}}{Z_{sample} + Z_{water}} \tag{5}$$

where $P$ denotes the pressure amplitude and $Z$ the acoustic impedance of the indicated subscripts. The acoustic impedance of a material is the product of its density, $\rho$, and speed of sound, $c$, ($Z = \rho c$) and its unit is Rayl = kg/(m$^2$·s). Acoustic impedance is also related to a material's stiffness, $C$, as $C = Zc$. Hence, in SAM, the amplitudes of the reflected echoes produce an acoustic impedance map, while the ToFs simultaneously provide a topography map. Related to bone, SAM has been used to spatially characterize bone [67, 68, 72-75] and cartilage [76-78].

In SAM, the lateral resolution is diffraction limited, typically enabling resolutions of 2–20 µm [67, 73, 74, 79]. The axial resolution in surface imaging (as opposed to subsurface imaging), on the other hand, is determined by the accuracy in determining ToF. To obtain accurate ToFs, short pulses are used. Unfortunately, short pulses contain little energy, and therefore the amplitudes of the reflected echoes are low, resulting in a low signal-to-noise ratio (SNR), especially in soft samples with low reflection coefficients. One way to mitigate the low SNR is to use averaging, but imaging the same spot many times causes long imaging times. This is the problem coded-excitation SAM, i.e. CESAM, solves. In CESAM, the transmitted signals are long (to increase deposited energy and thus improve SNR) and frequency modulated (to allow accurate ToF determination) [61]. With our CESAM, features as small as ~150 nm in height can be discerned [61]. The improved

SNR also reduces and even eliminates the need for averaging, decreasing imaging time.

Due to the high SNR and axial resolution in CESAM, as well as its ability to create acoustic impedance and topography maps simultaneously, the hypothesis in paper III was that CESAM could be an excellent tool to study BAG remodelling *ex vivo*. While an *in vivo* measurement modality would be preferable, studying the remodelling stages and accompanying changes in mechanical properties of the bone tissue can still provide valuable insight into the remodelling process. To validate CESAM, it was compared to other standardized methods: The acoustic impedance was compared to scanning electron microscopy with elemental analysis (energy dispersive X-ray spectroscopy) (SEM-EDX) and the topography map was compared to scanning white light interferometry (SWLI) [80]. Not only did CESAM measurements agree with SEM-EDX and SWLI, but as CESAM provides maps of both the mechanical properties and the topography simultaneously, it allowed determining regions-of-interest related to bone formation with greater ease and confidence than with either SEM-EDX or SWLI alone.

With the work in Meriläinen *et al.* validating our CESAM's imaging capability on hard samples (USAF resolution sample) [61], paper III demonstrated its applicability for a complex sample (the bone sample containing both soft and hard substances) that also featured height variations. Having thus validated CESAM on different kinds of samples, quantification of gold removal from PCBs with CESAM was deemed reliable. Furthermore, as CESAM can image complex and soft samples, it might enable future quantification of gold removal from not only PCBs, but flexible electronics as well.

# 2 Aims

The claim of this dissertation is that gold can be removed from e-waste – solely from predetermined areas – using only HIFU-induced cavitation in water, i.e., without added chemicals. This claim was investigated through the following aims:

**Aim 1:** Show that gold can be removed from the gold connectors of PCBs with HIFU-induced cavitation. The first results were demonstrated in paper A. In paper I, the results were extended to investigate controlling the amount of removed material by selecting a suitable number of sonicated bursts.

**Aim 2:** Improve gold removal efficiency by using a lower frequency while still restricting the removal area to the gold pad, not the surrounding PCB substrate. This was achieved in paper II.

**Aim 3:** Explore the method's applicability to machining of other metals. Aluminium erosion and engraving were demonstrated in papers B and C.

**Aim 4:** Demonstrate that the CESAM, used to quantify gold removal and machining of aluminium, is also capable of imaging more complex and soft samples, thus cementing our confidence in its imaging capability. This was achieved in paper III.

# 3 Methods

The Methods are divided into two parts: 3.1 Metal erosion and 3.2 CESAM evaluation. The parameters for CESAM quantification of the metal erosion are provided in their appropriate sections while the technical details about the CESAM device are given in 3.2. All data analyses were performed using Matlab.

## 3.1 Metal erosion

### 3.1.1 Setup and samples

A schematic of the HIFU setup used for metal erosion in papers I, II, A, B, and C is shown in Figure 4. Minor changes were made to the setup for the different papers.

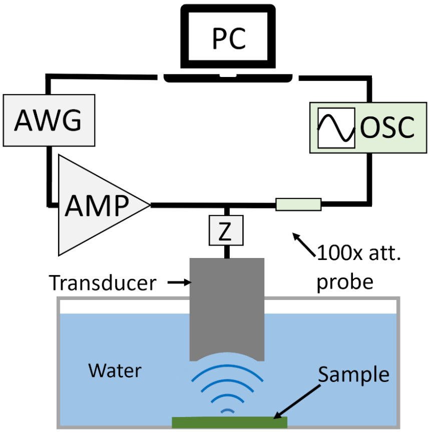

Figure 4 HIFU material removal setup. The sample was placed in water immersion and sonicated with a custom-built transducer mounted to a PC-controlled three-axis translation stage. Excitation signals were created with the arbitrary waveform generator (AWG), amplified with a power amplifier (AMP), and transmitted to the transducer. Impedance matching (Z) was used in papers I and II to ensure maximum power transfer. For imaging and initial positioning of the transducer, echoes from the sample were recorded with an oscilloscope (OSC) and processed on the PC. A 100x attenuating probe was used to protect the oscilloscope from the high-amplitude excitations in erosion experiments ($U_{PP} \approx 400$ V, small variations between papers). Only small changes to the hardware were made between papers I, II, A, B, and C (outlined in the text).

The transducers were custom-built from commercial curved piezo bowls with epoxy backing in a 3D printed housing. In papers I, II, A, B, and C, 11.8 MHz transducers (bandwidth 1.2 MHz, element diameter 19 mm, focal distance 15 mm) were used (one transducer for I and II (Type Pz26, CTS Ferroperm, Denmark), another for A, B, and C (F5265018, Meggitt A/S, Denmark)). In paper II, two additional transducers with the same element diameter and focal distance were used with centre frequencies 4.2 MHz and 7.3 MHz. The transducer was used to image the sample and position the transducer prior to all erosion experiments, which was done with a PC-controlled motorized three-axis translation stage (NLS4 NEMA 17 MDrive, Newmark Systems Inc., USA). Transmission, signal acquisition, and the translation stage were all controlled by a custom-written Python script (Python 3). The transmitted pulsed signals were created with an arbitrary waveform generator (AFG31052 series, Tektronix, USA) and in erosion experiments they were amplified with a power amplifier (500A100A, Amplifier Research, USA) at maximum amplification (100 % RF gain). During positioning and imaging, the echoes were recorded with an oscilloscope (Picoscope 5442D, Pico Technology, UK). A 100x attenuating probe (TT-HV250, TESTEC Elektronik GmbH, Germany) was used to protect the oscilloscope from the high excitation voltages during erosion experiments.

The measured excitation voltages for erosion experiments were $U_{PP} \approx 400$ V, with small variations between the different papers. In papers A, B, and C, impedance matching was not used and the obtained pressure levels only roughly estimated. In papers I and II, an LC impedance matching circuit was used to ensure maximum power transfer from the 50 Ω output of the amplifier to the transducers. The pressure amplitude at the focus was estimated in paper I from measurements with an optical hydrophone (ONDA HFO-690, Ø = 100 µm, Onda Corporation, USA) placed directly at the focus: $P_{PPP} = (46 \pm 1)$ MPa and $P_{PNP} = (-35 \pm 5)$ MPa (mean ± 1 SD from 15 signals). In paper II, the pressures at the foci were estimated using transient nonlinear acoustic holography from pressure measurements in the nearfield using the same hydrophone: $f = 11.8$ MHz, $P_{PPP} = 187$ MPa, $P_{PNP} = -35$ MPa; $f = 7.3$ MHz, $P_{PPP} = 107$ MPa, $P_{PNP} = -25$ MPa; $f = 4.2$ MHz, $P_{PPP} = 152$ MPa, $P_{PNP} = -40$ MPa. The discrepancy between measurements for 11.8 MHz in papers I and II can be explained by cavitation onset after just three cycles, which in the direct measurements of paper I led to loss of the signal (shielding bubbles). It was therefore a minimum estimate.

All sonications were performed in purified water (RiOs Essential Water Purification Systems, Merck KGaA, Germany) that had been degassed (Laboport UN 810.3 FTP vacuum pump, KNF Neuberger GmbH, Germany) for 30 min (paper I) to 1 h (paper II) prior to experiments.

One PCB sample, cut from a discarded circuit board, is shown in Figure 5a. The gold layer thicknesses of the samples were measured with Rutherford backscattering spectrometry using a 3 MeV proton beam from the 5 MeV tandem accelerator at the University of Helsinki. The obtained thicknesses were (1.73 ± 0.04) µm (paper I) and (1.64 ± 0.04) µm (paper II). A $^{7}$Li-beam was used for paper A, the gold layer was (870 ± 20) nm.

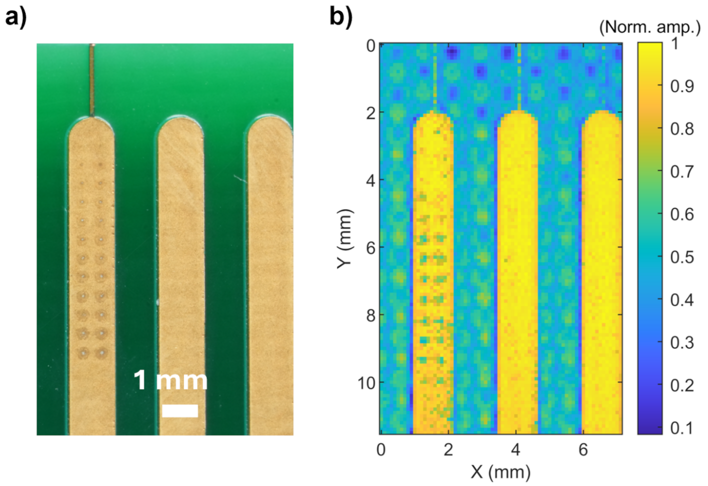

Figure 5 a) Photograph of one PCB sample and b) an acoustic image taken with the 11.8 MHz transducer (paper I). Pristine pads and erosion holes from prior experiments are visible in both. The internal structure of the fibreglass-epoxy substrate is visible in the acoustic image.

The gold pads were located by imaging with the transducer at low power. An example amplitude map obtained as a pulse-echo measurement with the 11.8 MHz transducer is shown in Figure 5b (10 cycles per burst, step size 100 µm) (paper I). The gold pads are easily distinguishable from the PCB substrate and even erosion holes from prior experiments are visible.

### 3.1.2 Gold removal

The first proof-of-concept gold removal test (paper A) was conducted without impedance matching between the power amplifier and the transducer, and thus the results are not directly comparable to papers I and II.

In paper A, gold removal was performed in three extraction areas (forming three large erosion holes), each consisting of a 5 x 5 grid of sonication spots with 20 µm spacing (area 80 µm x 80 µm). Sonications were performed at the focus (transducer-sample distance chosen to maximize reflected echo amplitude) and the sonication parameters for each spot were $f$ = 11.8 MHz, 30 cycles per burst, 250 000 bursts, maximum amplitude (~40 MPa), and pulse repetition frequency (PRF) 1 kHz.

In paper I, gold removal was studied more closely using the 11.8 MHz transducer. First, an optimal defocus distance (transducer-sample distance, +/-

from the focus) was sought. Constant sonication parameters were: maximum amplitude ($U_{PP}$ = 398 V, $P_{PPP}$ = 46 MPa, $P_{PNP}$ = −35 MPa), 50 cycles per burst, 500 000 bursts per sonication spot, PRF = 500 Hz. Three repetitions with 13 defocus distances were performed from defocus −500 µm (focus inside the sample) to +700 µm (focus above the sample) in 100 µm steps. The optimal defocus was found to be between 0 µm and +300 µm, thus +150 µm was selected and used in subsequent experiments. Second, a burst sweep was done to evaluate gold removal as a function of input energy. Constant sonication parameters were: defocus distance +150 µm, 50 cycles per burst, PRF = 500 Hz, maximum amplitude ($U_{PP}$ = 398 V, $P_{PPP}$ = 46 MPa, $P_{PNP}$ = −35 MPa). Bursts were varied between spots ([50, 100, 150, 200, 250, 300, 350, 400, 450, 500, 600, 700] × 1000 bursts per spot) and three repetitions were performed.

The erosion holes in papers A and I were measured with CESAM using a 375 MHz transducer (bandwidth 140 MHz, focal width 2.5 µm, depth-of-focus 29 µm, scan step size 2 µm in I, 1 µm in A) and a 300–500 MHz linear frequency modulated chirp of 1 µs length with a Gaussian envelope. Comparing the CESAM amplitude and topography maps to optical microscope images (Figure 6), two erosion effects are visible. Deep centre pits were formed, from which gold had been removed. They are readily visible in the CESAM topography map and seen as a colour change in the optical image (unearthing the nickel underneath). Surface roughening caused by stochastic cavitation events around the deep pit had also occurred. This is seen as a darker ring in the optical images and CESAM amplitude map. Erosion volumes of the deep pits were calculated from topography maps. Knowing the gold layer thickness and pit volume, the mass of removed gold (using density of gold $\rho_{Au}$ = 19.32 g/cm$^3$ [81]) was calculated as well.

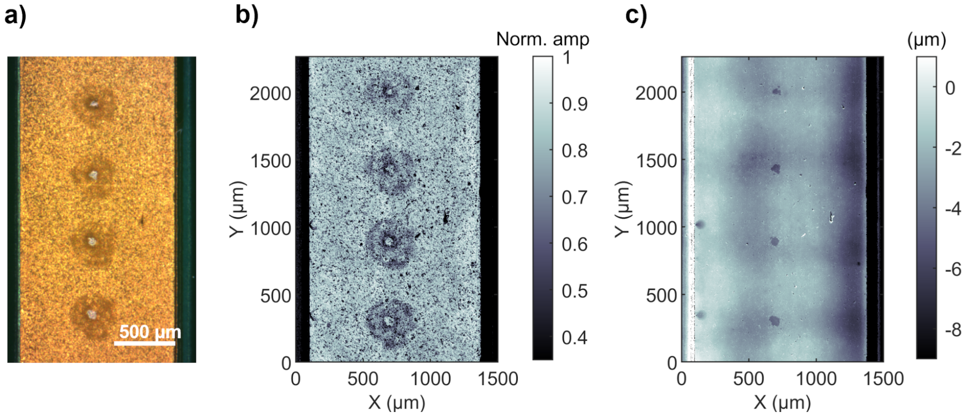

Figure 6 a) Optical microscope image, b) CESAM amplitude map, and c) CESAM topography map shown as examples of four corresponding erosion holes from one burst sweep. Surface roughening is seen in the optical image and amplitude map (a,b) and deep erosion holes, where the underlying nickel has been unearthed, are readily visible in the optical image and topography map (a,c). Erosion volumes of the deep pits were calculated from the topography maps.

In paper II, three different transducers were used for gold removal with centre frequencies of 4.2 MHz, 7.3 MHz, and 11.8 MHz (same transducer as in paper I). The purpose was to determine whether lowering the frequency could increase gold removal efficiency. This hypothesis was based mainly on two aspects: lower frequencies have lower cavitation thresholds (shown in Figure 2), and bubbles achieve larger size and more violent collapse with lower frequencies (due to the longer growth phase). In paper II, gold removal was quantified from optical microscope images.

Again, the optimal defocus distances were determined for the three transducers by performing defocus sweeps: ±1400 µm (200 µm steps) for 4.2 MHz; −600 µm to +2200 µm (200 µm steps) for 7.3 MHz; −500 µm to +900 µm (100 µm steps) for 11.8 MHz. Sonication parameters (except frequency) were constant for all three transducers: 50 cycles per burst, 500 000 bursts per spot, PRF = 500 Hz, and maximum excitation voltage (measured to be $U_{PP}$ = 430 V). The optimal defocus distances were selected as +200 µm for the 4.2 MHz and 11.8 MHz transducers, and +500 µm for the 7.3 MHz transducer.

To study gold removal efficiency, sonications were performed with the three transducers (4.2 MHz, 7.3 MHz, and 11.8 MHz) and varying the number of bursts from 100 000 to 1.9 million. Other sonication parameters were kept constant: maximum excitation voltage ($U_{PP}$ = 430 V), 50 cycles per burst, PRF = 500 Hz.

### 3.1.3 Aluminium erosion

Aluminium erosion was performed in papers B and C using the same 11.8 MHz transducer as for gold removal in paper A (without impedance matching). The samples were aluminium plates (AW-5754-H22), polished to a mirror finish using a grinder-polisher (TegraPol-25, Stuers, Denmark) with polishing paste (Akamono+, monocrystalline diamond suspensions, 15 µm & 6 µm particles).

All erosion marks on aluminium (in both papers B and C) were imaged with the same CESAM and CESAM settings as in the gold removal studies (papers I, A). The topography maps were used to visualize the marks and analyse erosion volumes.

In paper B, individual erosion holes were studied as a function of number of sonicated bursts. Five repeats were made, in which 15 different spots were sonicated with increasing burst count, from 1 000 to 15 000 in steps of 1 000 bursts. Other sonication parameters were kept constant: 80 cycles per burst, estimated pressure amplitude 24 MPa, PRF = 500 Hz, sonications performed at the focus.

In paper C, the possibility to machine aluminium with our setup was explored. First, the total input energy was kept constant (with amplitude 33 MPa) while the effects of transducer velocity, PRF, cycles per burst, and number of passes over the same line were investigated. Three different combinations of cycles per burst and PRF (25 cycles and 1 kHz PRF; 50 cycles and 500 Hz PRF; 100 cycles and

250 Hz PRF) were used to engrave 1 mm long lines in two different ways: with 20 passes over the same line at 50 µm/s or with 200 passes at 500 µm/s. Next, based on the results, constant velocity and PRF values (50 µm/s and 250 Hz) were selected to investigate the impact of input energy on engraving. Three amplitudes were chosen, 26 MPa, 33 MPa, and 38 MPa. For each amplitude, nine engravings of 1 mm lines were performed: using 10, 20, and 30 passes with 50, 100, and 200 cycles per burst. Finally, the word “ETLA” (the Finnish abbreviation of our laboratory) was engraved in 500 µm tall letters with 125 µm spacing using the sonication parameters: 33 MPa amplitude, 200 cycles per burst, PRF 250 Hz, 30 passes.

## 3.2 CESAM evaluation

To evaluate the performance of our CESAM on a complex sample – partially ossified BAG implant in rabbit bone – three separate imaging modalities were used to image the same area of the bone sample: CESAM, SWLI, and SEM-EDX. All images were manually co-registered. The EDX was used along one scan line containing both a BAG granule and surrounding tissue.

To evaluate CESAM, its topography map was compared to the SWLI, and its acoustic impedance map was compared to the SEM-EDX elemental analysis along the scan line. Details about the imaging methods and samples are given below.

### 3.2.1 BAG and bone samples

The BAG implants’ manufacturing process is described in detail in [82, 83]. The BAG used was BAG-S53P4 consisting of (in weight-percentage) 53 % $SiO_2$, 23 % NaO, 20 % CaO, and 4 % $P_2O_5$. It was melted twice and annealed to achieve sufficient homogeneity. The BAG block was crushed and sieved into 300–500 µm granules. To obtain cylindrical porous scaffolds of 5 mm x 15 mm size (diameter x height), the granules were sintered in nitrogen atmosphere at 720 °C for 90 min.

A BAG scaffold was implanted in a skeletally mature rabbit (NZW, Harlan laboratories) under general anaesthesia under aseptic conditions. A direct lateral approach to the knee and exposure of the femoral lateral epicondyle was performed, followed by drilling a horizontal bone defect of 6 mm without penetrating the medial cortex. The defect was filled with the 5 mm x 15 mm BAG-S53P4 scaffold. Cefuroxime, buprenorphine, and carprofen were given postoperatively for infection prophylaxis and pain relief for three days. The animal was euthanized at 8 weeks post treatment with an overdose of pentobarbital. The distal part of the femur was cut and stripped from soft tissue and stored in formalin at +4 °C. The study was approved by the Animal Experimental Board of Finland (ESAVI/440/04.10.07/2014) and the laboratory care guidelines of the University of Helsinki, the ARRIVE guidelines, and the Directive 2010/63/EU of the European Parliament and the Council of the European Union were strictly followed.

The bone sample was prepared for imaging by first moulding it in epoxy and then grinding it in ethanol in the axial plane with increasingly fine sandpaper, lastly with P4000 sandpaper. The process is described in more detail in [83]. The sample was dried in a vacuum oven at 40 °C for four weeks.

## 3.2.2 Imaging modalities

### 3.2.2.1 CESAM

Our custom-built CESAM [61] was used to image the sample and obtain simultaneous amplitude and topography maps. A schematic of the device is shown in Figure 7.

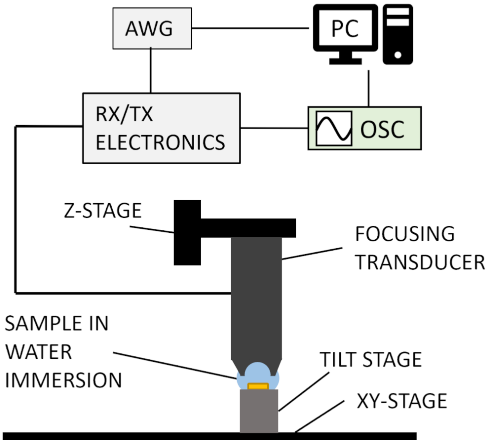

Figure 7 Schematic of CESAM. The 256 MHz focused transducer transmits a coded signal (a linear frequency-modulated chirp, 130–370 MHz), created by the arbitrary waveform generator (AWG). The signal is reflected from the sample surface to the same transducer, recorded with the oscilloscope, and postprocessed on the PC. The TX/RX electronics control when the electronic signal is transmitted to (TX) or received from (RX) the transducer. The sample is scanned in the xy-plane in water immersion (a droplet placed on the sample). The transducer is exchangeable (e.g., a 375 MHz transducer was used for gold removal quantification).

The transducer is scanned horizontally (in the xy-plane) using two orthogonally aligned translation stages (MLS203-1, controller BBD202, Thorlabs, USA) with 50 nm encoder resolution. The vertical movement (z-direction) is controlled by another translation stage (MTS 25/M-Z8 and KDC101, Thorlabs, USA). The received echoes are amplified with a low-noise pre-amplifier (ZFL-1000LN+, Mini Circuits, USA) and recorded with a PCIe digital oscilloscope (M4i.2233-x8, 2.5 GS/s, Spectrum Instrumentation GmbH, Germany).

The transducer can be exchanged depending on the sample. For the leporine bone sample, a 256 MHz centre frequency transducer was used (lateral width of focus 5.9 µm, depth of focus 49 µm, working distance 577 µm, −6 dB bandwidth: 144–368 MHz). The coded excitation was a 1 µs long linear frequency-modulated chirp (130–370 MHz) with a Gaussian envelope. The imaging scan was made in water immersion over an 880 µm x 1260 µm area with 1 µm stepping.

The topography was calculated directly from the measured ToFs using the longitudinal sound velocity in water ($c$ = 1483 m/s [84]). To obtain the acoustic impedance according to Equation 5, an amplitude calibration was performed using a method described in [73], as the transmitted acoustic pressure amplitude is not measured by the CESAM. Three flat calibration samples were used with the same transmission settings as for the bone sample: acrylic (PMMA), silicon, and sapphire, with acoustic impedances, $Z = 3.3$ MRayl, $Z = 22.0$ MRayl, and $Z = 41.7$ MRayl, respectively. All samples were carefully aligned to allow assuming normal incidence at each scanned point. As the focal width was only 5.9 µm, this is a fair assumption also for the bone sample, except in the vicinity of narrow and steep notches. The amplitudes from the bone sample were compared to the obtained calibration curve, producing the acoustic impedance map.

#### 3.2.2.2 Scanning white light interferometry (SWLI)

A custom-built SWLI, described in detail in [80], was used to obtain a topography map with higher resolution than with CESAM (wavelength of the SWLI is 400–800 nm, 5.6 µm of 256 MHz ultrasound; height resolution of SWLI is ±15 nm, ~150 nm of CESAM). The SWLI is built on a Nikon side-illuminated microscope frame and comprises a CMOS camera (Hamamatsu Orca-Flash 2.8, Japan) with a 10x objective (10x Nikon CF IC Epi Plan DI, Japan) and a 1x tube lens (Nikon 200 mm, Japan). Vertical scanning of the sample is performed by moving the objective within a 100 µm range using a piezo actuator (PI Pifoc P-721-CDQ, Physik Instrumente (PI) SE & Co. KG, Germany). For lateral scanning, xy-stages (8MTF-102LS05, Standa Ltd, Lithuania) with 0.31 µm resolution are used.

The sample was imaged with 17 sub-aperture scans, with 30 % spatial overlapping, that were stitched together. Custom-made software was used for data acquisition and surface detection, while surface stitching and 3D analyses were done with commercial software (MountainsMap, Digital Surf, France).

#### 3.2.2.3 Scanning electron microscopy with elemental analysis (SEM-EDX)

The sample was coated with a 5 nm Pt/Pd layer prior to imaging. The SEM image was obtained with a scanning electron microscope (Coxem SEM EM-30 AX Plus) using an in-lens upper secondary electron detector with 150x magnification. The acceleration voltage was 15.0 kV with a take-off angle of 25.8° and resolution of

133 eV (at 5.89 keV Mn). Elemental analysis was obtained along one 450 µm long scan line using Energy Dispersive X-ray Spectroscopy (EDX) with an Edax EDX detector of SDD type.

# 4 Results

The results are grouped into three sections: 4.1 Gold removal, 4.2 Aluminium erosion, and 4.3 CESAM capability. In 4.1, results from papers A, I, and II are shown, which correspond to Aims 1 (demonstrating gold removal) and 2 (improving removal efficiency) of this dissertation. 4.2 shows the results from papers B and C, relating to Aim 3 (removal of other metals). In 4.3, the results with the soft and complex sample (partially ossified BAG in leporine bone) from paper III are presented, corresponding to Aim 4 (exploring CESAM's capability).

## 4.1 Gold removal

### 4.1.1 Demonstrating gold removal

In paper A, gold removal was performed in three extraction areas, each consisting of a 5 x 5 grid of sonication spots with 20 µm spacing (an 80 µm x 80 µm grid). As the focal width of the transducer was 140 µm, the extracted areas were larger than the grid, approx. 200 µm x 200 µm. The topography of one extraction area and its 3D depth profile is shown in Figure 8. The measured gold-layer thickness was used to calculate the volume and mass of the removed gold.

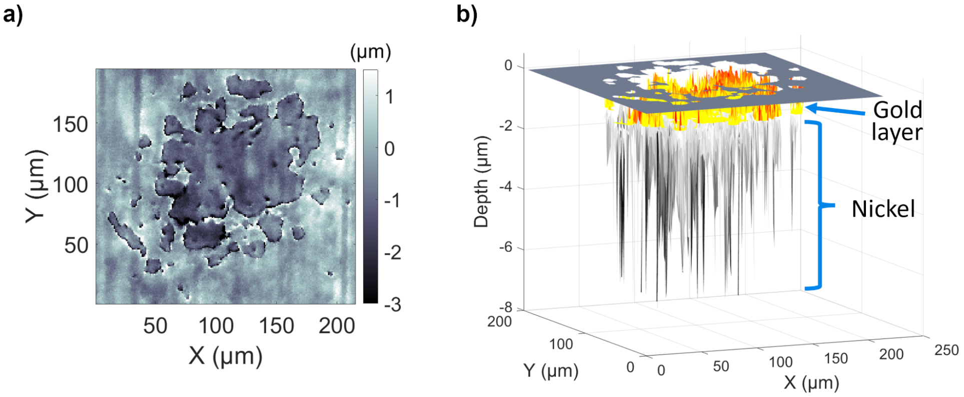

Figure 8 CESAM topography map of one extraction area. a) Top view. All extraction areas, including the sporadic spots along the edges, were calculated from this view. b) 3D depth profile of a). The measured gold-layer thickness was used to calculate removed gold volume and mass. © 2022 IEEE.

The average gold removal areas, volumes, and masses were calculated for the three extraction areas (average ± 1 SD): $A = (12.2 \pm 0.5)\cdot 10^3$ µm$^2$, $V = (18 \pm 2)\cdot 10^3$ µm$^3$, and $m_{Au} = (190 \pm 20)$ ng. For the gold masses, the greatest source of uncertainty came from the ±20 nm uncertainty in gold-layer thickness, which was hence used to estimate the uncertainty in mass instead of the standard deviation.

As Figure 8b shows, much nickel was also removed. As removing only gold would be desirable for e-waste recycling purposes, these results led to the more rigorous investigation in paper I: determine sonication parameters with which only gold would be removed.

In paper I, the first task was to determine optimal defocus distance (transducer-sample distance, ± from the focus) for gold removal. The results from the three defocus sweeps are shown in Figure 9a. Largest erosion areas were achieved in a range between 0 µm and +300 µm defocus (positive defocus implies focusing above the sample). In this region, the widths of the deep centre pits approached the width of the main lobe of the focus (140 µm). One example hole at +100 µm defocus is shown in Figure 9b. Apart from the main erosion pit, only a few minor stochastically generated pits appeared in the optimal defocus range. A defocus of +150 µm was selected for subsequent erosion experiments.

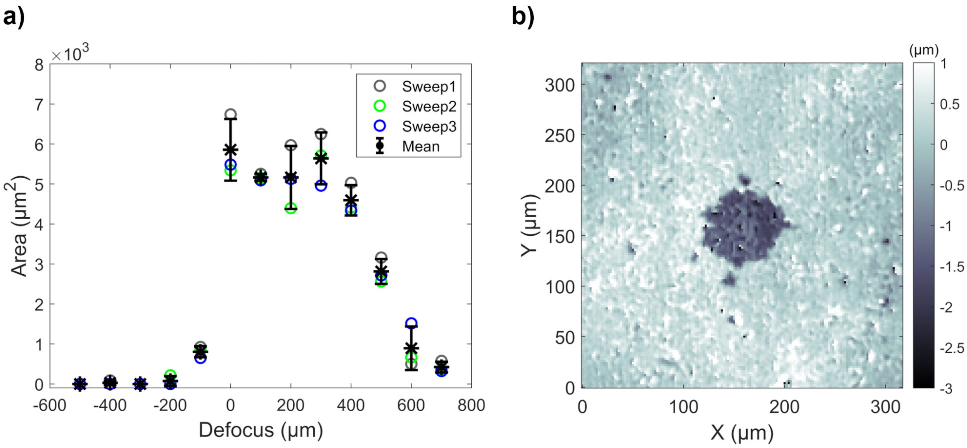

Figure 9 Determining optimal defocus distance. a) Erosion areas from three defocus sweeps shown separately and their mean ± 1 SD. Defocus 0 µm signifies focusing at the surface, positive (negative) values above (beneath). Largest erosion areas were achieved between 0 µm and +300 µm defocus. b) Topography map of one example hole at +100 µm defocus. The width of the centre pit is slightly less than the 140 µm focal width. Only a few stochastic cavitation pits (small pits) are visible outside the main lobe.

After determining an optimal defocus distance (+150 µm), the main investigation of paper I was performed: determine the number of bursts (input energy) to control gold removal and restrict the erosion to only the gold. As expected, the erosion areas and volumes increased with burst count. More bursts enabled more cavitation events to take place, thus increasing the amount of removed material. The total eroded areas and volumes are presented in Figure 10.

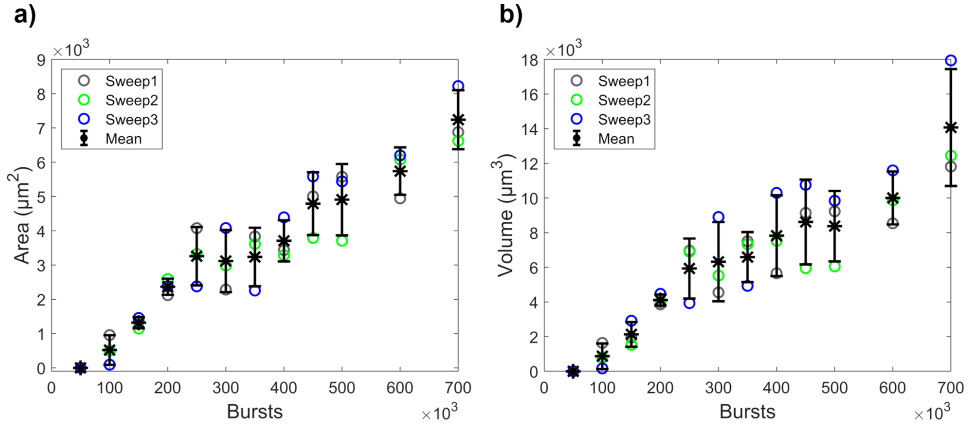

Figure 10 Material removal as a function of sonicated bursts. a) Area and b) volume of the deep erosion pits (excluding surface roughening). The three repeats are shown separately (sweeps) and their mean ± 1 SD.

Using the measured gold-layer thickness, (1.73 ± 0.04) µm, the volume of removed gold and nickel was calculated, Figure 11. Nickel started to be removed after approx. 250 000 bursts. When nickel removal begins, a slight plateauing effect in the gold removal volume is seen. The gold removal does not halt entirely, as erosion continues in the outer regions of the focus with lower pressure, and thus cavitation activity. As removing only gold, without nickel, would be desirable in a gold recycling application, it seems preferable to restrict the number of bursts and then move the transducer, instead of sonicating a long time in one spot. Despite cavitation being a phenomenon of deterministic chaos, the gold removal appears reasonably repeatable at these high burst counts.

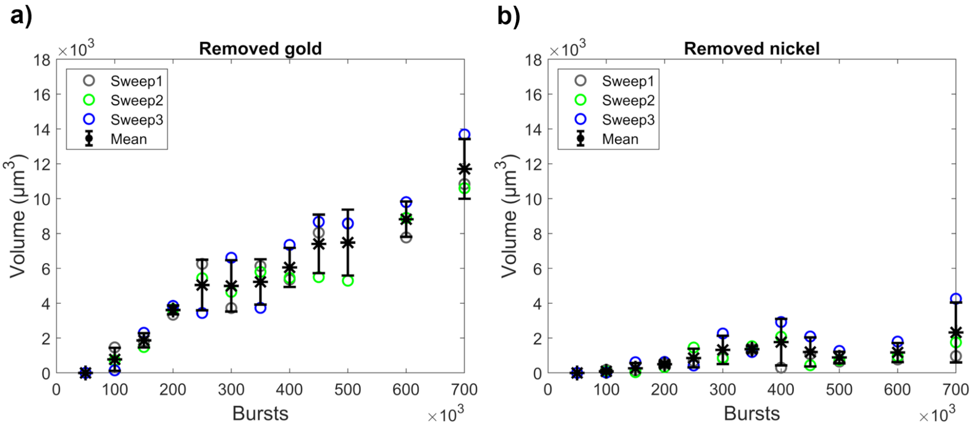

Figure 11 Volumes of removed a) gold and b) nickel. The repeats are shown separately, and their mean ± 1 SD. Gold removal is reasonably repeatable at these burst counts.

The mass of removed gold was calculated from the gold removal volumes (Figure 12a). To obtain another indication of the most efficient burst count, the mass of removed gold was compared to the input electrical energy (Figure 12b). This gold removal efficiency, calculated as ratio of removed gold mass to input electrical energy (and normalized for readability), increased until 250 000 bursts, i.e., until nickel removal was initiated. Therefore, even though gold removal continues with higher burst counts, it becomes less efficient as electrical energy is wasted on removing nickel.

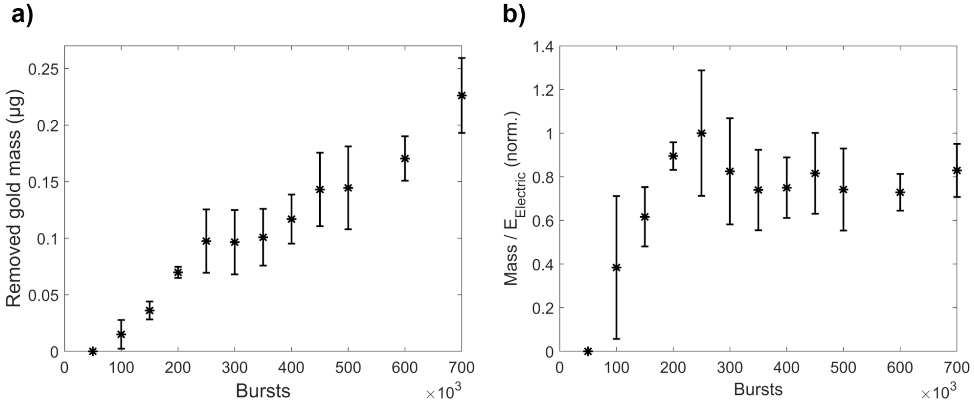

Figure 12 a) Mass of removed gold and b) removal efficiency as a function of bursts (mean ± 1 SD). Removal efficiency is the ratio of removed gold mass to input electrical energy. The efficiency values are normalized to the maximum mean value (at 250 000 bursts) for readability. The efficiency decreases when nickel is removed.

### 4.1.2 Improving gold removal efficiency

As the cavitation threshold decreases with decreasing frequency, paper II focused on improving gold removal efficiency by using lower frequencies, while still retaining a small enough spot size to erode only the gold pads. Thus, three transducers with the same element diameter and focal distance, but with different centre frequencies, were used: 4.2 MHz, 7.3 MHz, and 11.8 MHz (the same transducer as in paper I).

As in paper I, the optimal defocus distances were first sought. The 4.2 MHz and 7.3 MHz transducers removed gold over a wider range of defocus values, but both displayed marked peaks which were used in subsequent erosion experiments: +200 µm for 4.2 MHz and +500 µm for 7.3 MHz. A defocus of +200 µm was used for the 11.8 MHz transducer.

Next, burst sweeps were performed with all three transducers, with three repeats for each. Examples of optical microscope images of the erosion marks with the different transducers are shown in Figure 13. Key geometric measures of the acoustic fields at the foci, obtained by transient nonlinear acoustic holography, are overlayed: the positive-pressure-amplitude full-width half-maximum (FWHM+), negative-pressure-amplitude full-width half-maximum (FWHM−), and side-lobe ring (SLR).

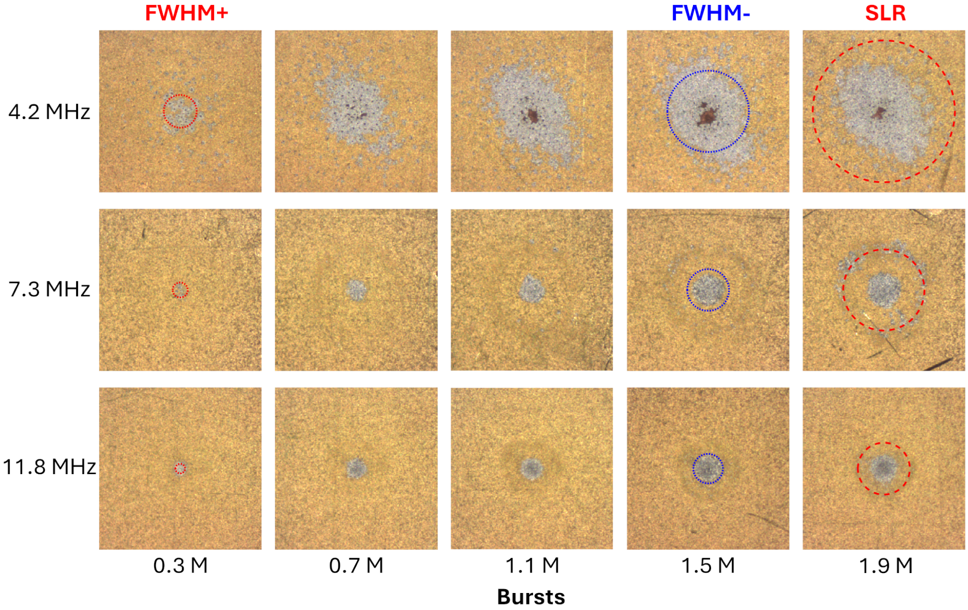

Figure 13 Optical microscope images of gold removal with the different transducers and increasing burst count ("M" denotes million). Key geometric features of the foci are overlayed: positive and negative pressure-amplitude full-width half-maxima (FWHM+, FWHM−) and side-lobe ring (SLR). At low burst counts (0.3 M), removal was confined to the FWHM+, increasing towards the FWHM−. At even higher burst counts, erosion was observed in the side lobe (SLR) with the 7.3 MHz and 11.8 MHz transducers. Erosion with 4.2 MHz was more violent; single deep pits were observed already at low burst counts and erosion progressed through the nickel layer into the copper (brown areas at the centre of the erosion mark). Each image is 1 mm wide.

The removal patterns were similar for the 7.3 MHz and 11.8 MHz transducers. Removal was confined to a small focal area, which grew with burst count. Erosion in the side lobe was particularly prominent for the 7.3 MHz transducer. The erosion area of the 4.2 MHz transducer was larger and the erosion more violent. For example, with 0.7 million bursts, single deep pits are seen, some deep enough to penetrate to the copper beneath the nickel layer. These single deep pits occurred around the edge of the main erosion area for all burst values.

As the erosion marks of the 4.2 MHz transducer contained many scattered single pits, two erosion areas (and subsequently volumes) were calculated for all transducers: largest, constituting the largest contiguous erosion area, and total, including the scattered areas. The erosion areas were determined from optical microscope images revealing the nickel (or copper) underneath. The areas were multiplied with the measured gold-layer thickness, (1.64 ± 0.04) µm, to obtain gold erosion volumes. The volumes of removed gold are presented in Figure 14, showing that the 4.2 MHz transducer removed much larger volumes than the other transducers. The pronounced side-lobe cavitation of the 7.3 MHz transducer causes the greater increase in total volume compared to largest volume for high burst counts.

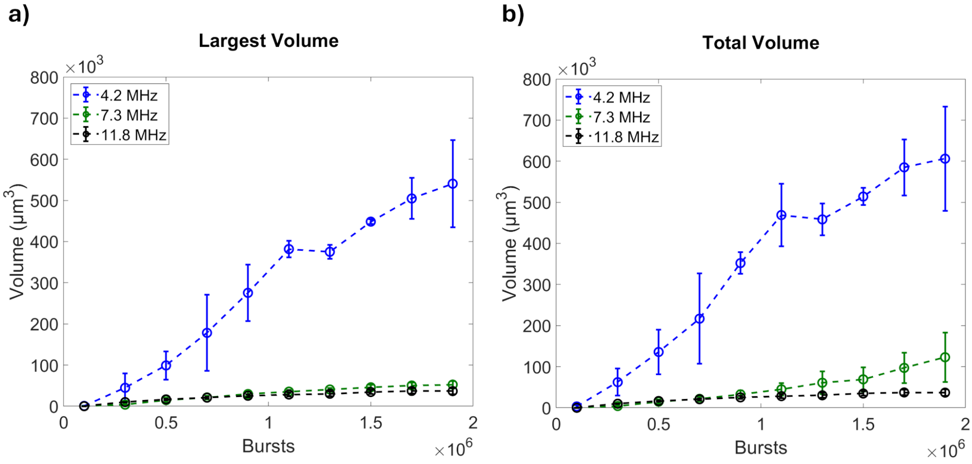

Figure 14 Removed gold volume increasing as a function of burst count (mean ± 1 SD of three measurements). a) Largest contiguous gold removal volume and b) total volume (including scattered removal areas). Cavitation in the side lobe was particularly pronounced with 7.3 MHz, causing the greater increase in total volume than largest volume. Lines are shown to guide the eye.

To compare frequency-related effects of the bubble dynamics on the subsequent gold removal, the electrical excitation amplitude and number of cycles per burst were kept constant for all three transducers. Due to the longer period of lower frequencies, this led to a higher electrical input energy for lower frequencies. This choice was made because higher amplitudes or numbers of cycles affect the dynamics of even single bubbles, thus confounding the frequency-related effects more than the overall input energy. To compare gold removal efficiency, the gold removal volumes were divided by the total input electrical energy. Gold removal efficiency is shown in Figure 15. All transducers displayed a maximum in gold removal efficiency of the largest contiguous volumes. Especially for 7.3 MHz and 11.8 MHz, this indicates that the focal region has become void of gold. The more sporadic erosion pattern of the 4.2 MHz transducer led to a more gradual increase in efficiency until reaching the maximum, and as seen in Figure 14, gold removal still continued. Again, the side lobe cavitation of the 7.3 MHz transducer causes a continuous increase in total volume removal efficiency.

Comparing the efficiency maxima of largest removal volume, the benefit of using a lower frequency becomes clear – the gold removal is 3.8 times more efficient using 7.3 MHz, and 4.6 times using 4.2 MHz, than with the 11.8 MHz transducer.

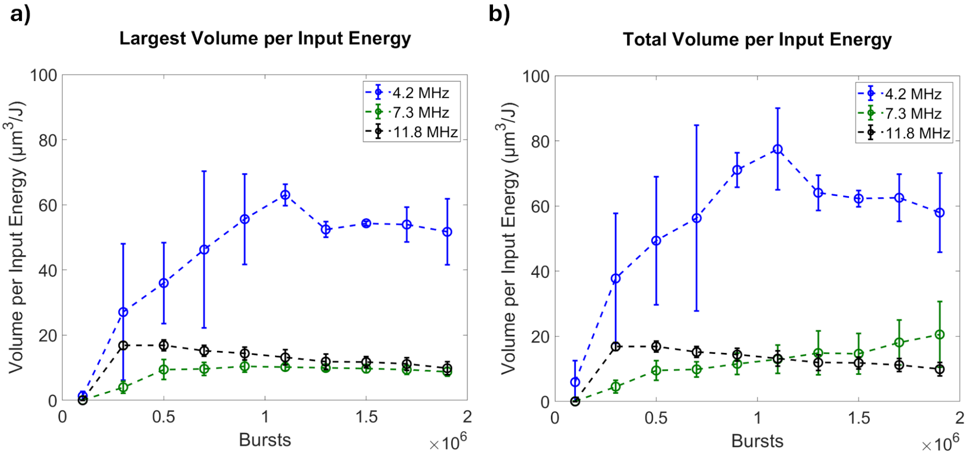

Figure 15 Gold removal efficiency: Volume of removed gold divided by input electrical energy (mean ± 1 SD of three measurements) for largest (a) and total (b) removed volumes. There is a maximum in gold removal efficiency of the largest contiguous volumes for all transducers. The 7.3 MHz transducer's removal efficiency of the total volume continues to increase due to pronounced cavitation erosion in the side lobe. Comparing the maxima, the removal efficiencies of 7.3 MHz and 4.2 MHz are 3.8 and 4.6 times that of the 11.8 MHz, respectively. Lines are shown to guide the eye.

## 4.2 Aluminium erosion

Aluminium erosion of individual sonication spots was explored in paper B using the same 11.8 MHz transducer as in paper A. The volumes of the erosion holes were measured with CESAM and the results are shown in Figure 16. Eroding aluminium required only a fraction of the bursts required for gold. For example, exceeding 5 000 µm³ erosion volumes required 8 000 bursts on aluminium, but 250 000 on gold (Figure 10b).

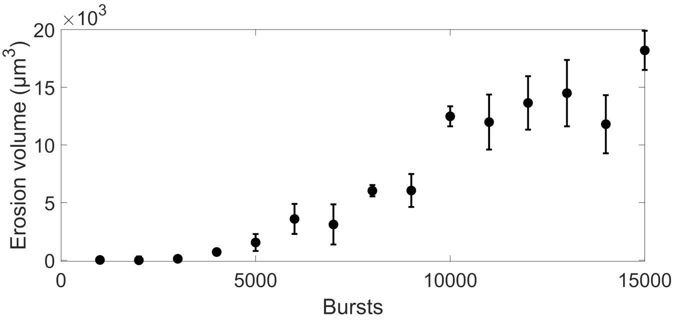

Figure 16 Erosion hole volumes on aluminium. Error bars are standard errors of the mean of five repeats. Note that reaching volumes exceeding 5 000 µm³ requires only 8 000 bursts on aluminium compared to 250 000 bursts on gold. © 2022 IEEE.

Progressing to machining in paper C, the first experiments were made with constant input energy to determine the effect of other sonication parameters on the thickness and evenness of 1 mm long engraved lines: transducer velocity, PRF, cycles per burst, and number of passes along the same line. Cycles and PRF were varied in pairs, with either 20 passes at 50 µm/s or 200 passes at 500 µm/s. The CESAM image is shown in Figure 17.

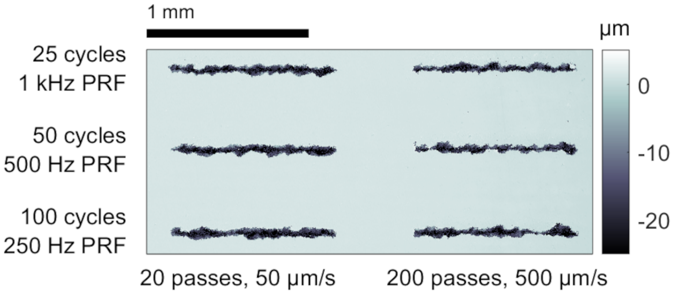

Figure 17 Aluminium engraving with constant input energy (CESAM topography map). All lines sonicated at lower speed (50 µm/s) are slightly thicker and more even. © 2022 IEEE.

All lines produced at the lower speed (50 µm/s) were slightly thicker than their counterparts (3–6 µm thicker) and more even (SD of linewidth was greater with 500 µm/s speed and 200 passes). A possible explanation could be the difference in spatial separation between consecutive pulses for the two speeds. With PRF = 250 Hz, the distance between pulses is only 0.2 µm at 50 µm/s speed, while it is 20 µm at 500 µm/s. Compared to the 140 µm focal width of the transducer, moving 0.2 µm is virtually sonicating in the same spot, while the 20 µm step seems large enough to alter the symmetry of the cavitation in the bubble cloud. Based on these results, a speed of 50 µm/s and 250 Hz PRF were selected for studying the effect of input energy on engraving.

The effect of input energy was studied in variations of three parameters: amplitude, cycles per burst, and number of passes along the engraved line. For three pressure amplitudes (26 MPa, 33 MPa, and 38 MPa), nine engravings of 1 mm lines were performed: using 10, 20, and 30 passes with 50, 100, and 200 cycles per burst. The results are presented in Figure 18. Increasing any parameter, i.e. increasing acoustic energy, resulted in widening of the lines.

All lines displayed some roughness of the edges, which is to be expected with the stochastic cavitation behaviour especially in the outer regions of the focal zone. In lower-energy lines, this stochasticity even resulted in segmentation of the line. Thus, for engraving, sufficient input energy is required to onset cavitation with sufficient reliability.

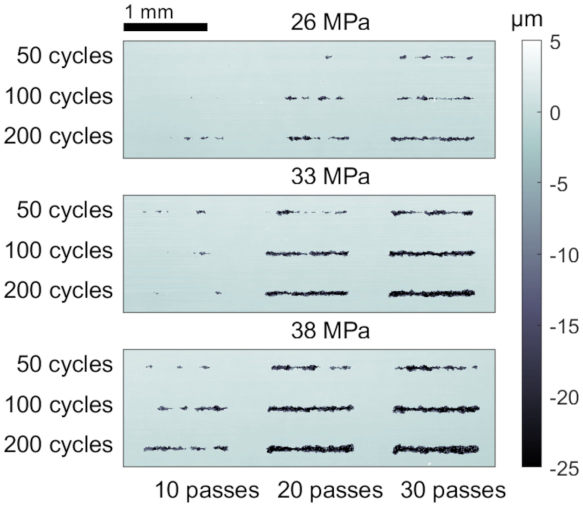

Figure 18 Effect of input energy on aluminium engraving with constant PRF (250 Hz) and speed (50 µm/s) (CESAM topography map). Increasing any parameter, i.e. increasing energy, results in widening of the lines. © 2022 IEEE.

While higher amplitudes produced more consistent erosion, higher amplitudes also caused a larger region of the focus to exceed the cavitation threshold, thus widening the lines. In many engraving applications, narrow lines are desirable. Hence, to engrave "ETLA" (the acronym of the Finnish name of our laboratory) in 500 µm tall letters, the selected engraving parameters were: 33 MPa pressure amplitude, 200 cycles, 20 passes, 50 µm/s speed, and 250 Hz PRF. The average line width and depth in Figure 18 with these parameters were (43 ± 13) µm and (20 ± 8) µm (mean ± 1 SD), respectively. The engraved "ETLA" is shown in Figure 19.

Figure 19 Letter engraving of "ETLA" (CESAM topography map). © 2022 IEEE.

The increased linewidth at the intersections was caused by the engraving procedure – the vertical and horizontal lines overlapped at the intersections, leading to double sonication. The line widths and depths were (53 ± 22) µm and (23 ± 10) µm, respectively. The line width of 53 µm corresponds to $0.42\lambda$ (wavelengths).

## 4.3 CESAM capability

To evaluate the CESAM's imaging capability, images of the BAG-S53P4-implanted leporine femoral epicondyle taken with CESAM, SWLI, and SEM were compared. A line intersecting both a glass granule and surrounding forming tissue was selected for closer inspection, including elemental analysis (SEM-EDX). The comparison of the different imaging modalities is presented in 4.3.1 Comparing imaging modalities.

As CESAM provides simultaneous topography and amplitude maps (the latter convertible to acoustic impedance), the added information facilitates easier and more reliable determination of regions-of-interest (ROIs) than from SWLI or other topography techniques alone. This is shown in 4.3.2 ROI determination using both acoustic impedance and topography information.

### 4.3.1 Comparing imaging modalities

Images of the bone sample with the different imaging modalities are presented in Figure 20. There are seven ROIs (i–vii) along the scan line, featuring different materials and stages of bone ingrowth. The results and comparisons of the imaging modalities are given below for each region.

**Region (i):** The region (0 µm to 140 µm) has an elemental composition (Figure 20a) corresponding to BAG-S53P4 (53 % $SiO_2$, 23 % NaO, 20 % CaO, and 4 % $P_2O_5$). Both SWLI (Figure 20b) and CESAM topography (Figure 20c, black) show a flat, slightly sloping region, which is also consistent with a large glass granule. Furthermore, the acoustic impedance (Figure 20c, red) in this region is high, $Z$ = (7.7 ± 1.2) MRayl (mean ± 1 SD) (*cf.* $Z_{acrylic}$ = 3.3 MRayl), confirming the presence of a hard material, i.e., a glass granule.

**Region (ii–iii):** After BAG implantation, a thick Si-rich layer is formed rapidly at the granule surface. CaP then nucleates and crystallizes to HA on top of the Si-layer. This process is seen here. An Si-spike is seen in Region (ii) (140–160 µm), followed by gradual increase in Ca and P, which continues into Region (iii). The HA-layer thus begins at the border between (ii) and (iii). Bone formation occurs gradually in (iii) (160–205 µm), which is seen from the constant Ca and P (in HA), accompanied by a slow increase in C (biological tissue) and rapid decrease in Si (bone ingrowth). The acoustic impedance of the flat section is moderate, reaching $Z$ = (5.4 ± 1.2) MRayl, with a curve shape following the Si-, Ca-, and P-content. Narrow notches as in (ii), seen in both SWLI and CESAM topographies, are present around all glass granules. This notch contains a tiny particulate (seen in the topography maps). The apparent low acoustic impedance in (ii) is probably caused by significant scattering from the edges of the narrow notch.

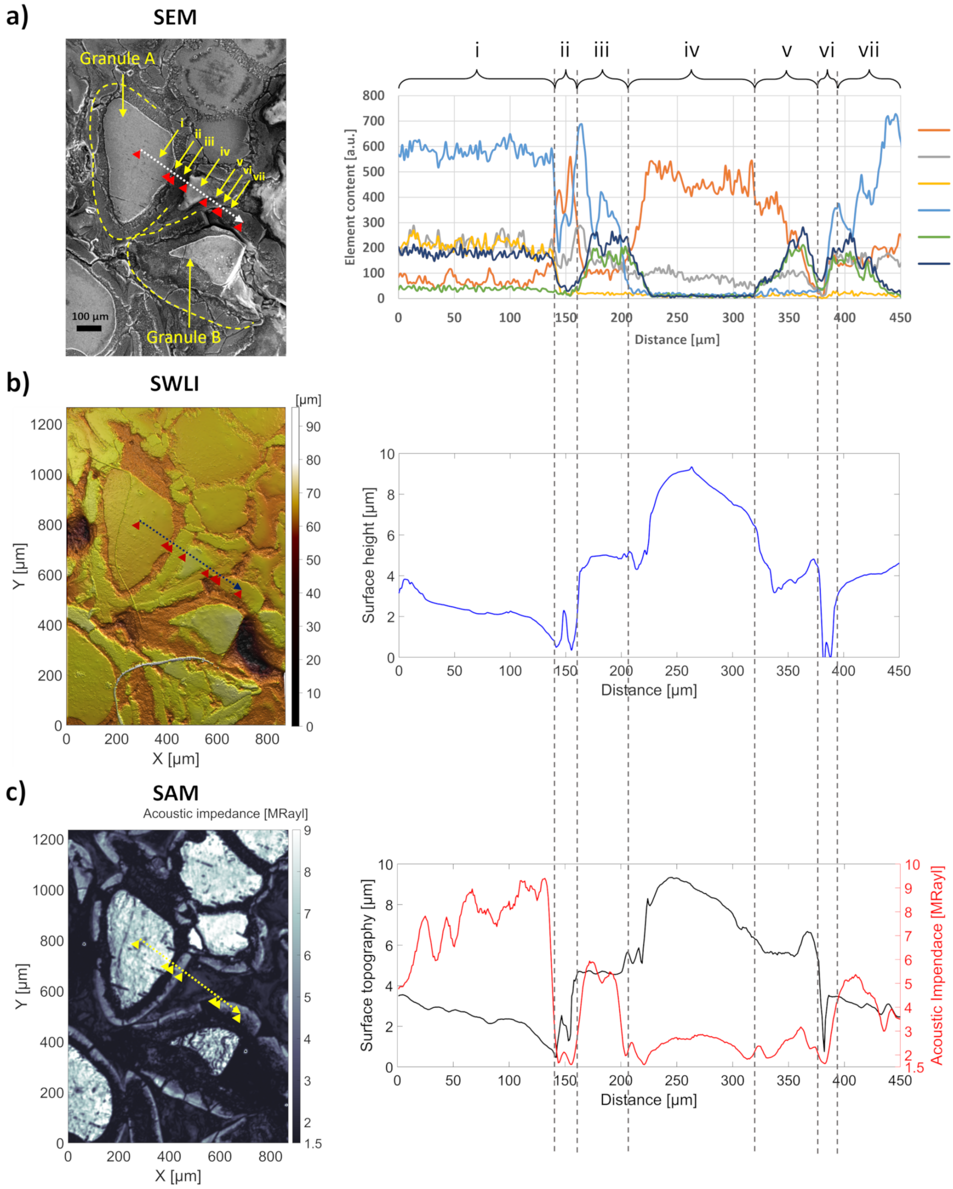

Figure 20 Bone ingrowth around BAG glass granules measured with a) SEM-EDX, b) SWLI, and c) CESAM. Data from the scan line, indicated in each image, are presented to the right. a) SEM image (left) with two marked glass granules (granules A and B). Elemental composition along the scan line, measured with EDX, is on the right. b) SWLI image (left) and topography along the scan line (right). c) CESAM acoustic impedance map (left), and acoustic impedance (red) and topography (black) along the scan line (right). ROIs (i–vii) (glass granule, Si-layer, HA-layer, epoxy, non-mineralized bone tissue, HA-layer, Si-layer) are indicated and discussed in detail in the text. CESAM's acoustic impedance (c, red) corresponds well to the elemental composition (a) and its topography (c, black) to the SWLI (b). Thus, CESAM encapsulates sufficient information for evaluating bone ingrowth.

**Region (iv):** Region (iv) (205–320 μm) is a representative example of how only one imaging modality might give misleading results. The SEM-EDX shows high C-content, but no Si, Ca, P, or Na. The acoustic impedance is also low, $Z = (2.5 \pm 0.3)$ MRayl (compared to 1.5 MRayl of water). These properties could be indicative of biological tissue. However, the homogeneity of the acoustic impedance and the tall smooth ridge in both SWLI and CESAM topography maps indicate that it cannot be tissue, but rather the fixing agent epoxy. Similar homogeneous patches are seen elsewhere in the acoustic impedance map, supporting this hypothesis.

**Region (v–vi):** The increase in Ca and P indicates the presence of bone tissue in (v) (320–375 μm). The acoustic impedance curve follows the same shape as these elements. Compared to (iii), the acoustic impedance remains lower, peaking at $Z = 3.2$ MRayl. This suggests that the bone tissue has not mineralized yet. The topography maps differ somewhat in (v) (CESAM estimates the flat region to be almost 1 μm higher than the SWLI), but both show a narrow notch in (vi) (375–395 μm). At the right edge of (vi), the Si-, Ca-, and P-levels increase, as the scan line encounters the bone formation layer around granule B.

**Region (vii):** The left part of (vii), from 395 μm to 435 μm, shows similar chemical composition and acoustic impedance (reaching $Z = 5.4$ MRayl) as in (iii), suggesting bone formation on top of the HA-layer around granule B. At 450 μm, CaP is no longer present and Si has increased further, suggesting that the line intersects the thick Si-layer around granule B in the tangential direction. Due to the notch in (ii), the acoustic impedance is underestimated due to scattering. In (vii), the sample is almost flat (in the SWLI and CESAM topographies), therefore the acoustic impedance in this Si-layer, from 435 μm to 450 μm, is more reliable: $Z = (3.1 \pm 0.4)$ MRayl.

To sum up, the acoustic impedances of the different materials/tissues were: glass granules (i), $Z \approx 8$ MRayl; Si-layer surrounding the glass granule (vii), $Z = (3.1 \pm 0.4)$ MRayl; bone formation on top of the HA-layer (iii), $Z = (5.4 \pm 0.3)$ MRayl; non-mineralized bone tissue (v), $Z = (2.4 \pm 0.4)$ MRayl; and epoxy (iv), $Z = (2.5 \pm 0.3)$ MRayl.

Based on the comparison, CESAM is able to measure and distinguish different materials related to bone formation and corresponds to both SEM-EDX and SWLI measurements. As seen in Region (iv), having access to both a mechanical and a topography map helps in determining substances of interest.

### 4.3.2 ROI determination using both acoustic impedance and topography information

To expand on the benefits of obtaining both the acoustic impedance map and the topography map simultaneously, three areas containing ambiguous features in

SWLI and CESAM topography maps were selected for comparison with the acoustic impedance map. These areas (Area 1–3) are shown in Figure 21.

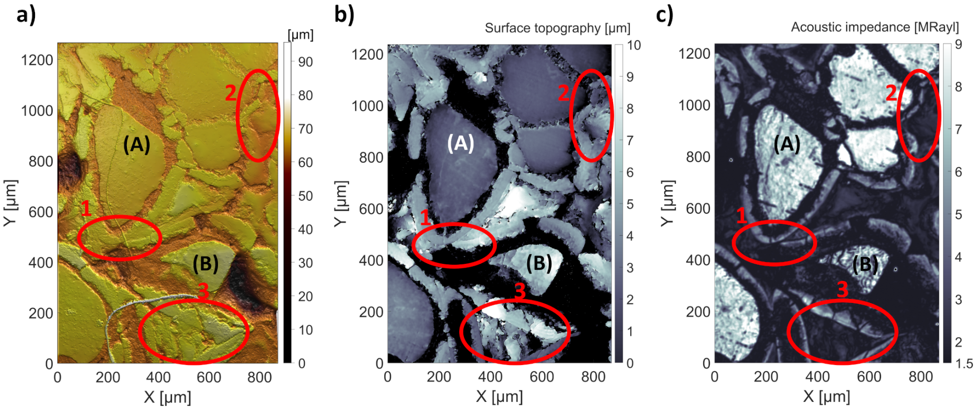

Figure 21 Comparing a) SWLI, b) CESAM topography map, and c) acoustic impedance map. Three areas (Area 1–3) with ambiguous features in both topography maps are highlighted. Obtaining simultaneous topography and acoustic impedance maps with CESAM assists in determining ROIs (described in detail in the text). Glass granules (A) and (B) are indicated.

**Area 1:** Area 1 illustrates the difficulty in distinguishing the exact border between the bone formation layers surrounding glass granules A and B. As this region is flat, the border is almost imperceptible in either topography map (Figure 21, a and b), despite the much higher lateral resolution of the SWLI compared to CESAM. However, the bone formation layers are readily seen in the acoustic impedance map (Figure 21c) (hard boundaries surrounding glass granules, *cf.* Region (iii), Figure 20) and the border between the two layers is evident.

**Area 2:** Both topography maps show a flat feature in Area 2, similar to adjacent glass granules. The acoustic impedance in Area 2 differentiates between the hard adjacent glass granules (*cf.* Region (i), Figure 20) and the flat feature: The low and homogeneous acoustic impedance leads to the conclusion that it is epoxy (*cf.* Region (iv), Figure 20).

**Area 3:** The interpretation of the uneven Area 3 from topography maps is elusive. One can only exclude a flat glass granule. Again, the acoustic impedance map provides insight: Area 3 contains a triangle of three bone formation layers with a soft material in the middle. The inhomogeneity suggests that the soft material is not epoxy (*cf.* Area 2), whereby it could be connective tissue or non-mineralized bone.

The results show that the imaging capability of CESAM was sufficient to evaluate the complex partially ossified bone sample. In addition, no averaging was used, which is a benefit compared to most SAMs. While a BAG-implanted rabbit bone might seem to have little connection to gold removal, or even gold removal quantification, it serves as a challenging validation sample: It contains both hard and soft materials – and includes height differences. As CESAM performed well on this sample, our confidence in its output was increased. Furthermore, with a growing supply of soft, flexible electronics, CESAM should be a useful tool for gold removal quantification even if the substrates in e-waste shift from hard PCBs towards soft polymers.

# 5 Discussion

The versatility of ultrasound and its adaptability to complex problems is astonishing. As is shown in this dissertation, with focused ultrasound – but used in different ways – one can achieve, for example, imaging of complex samples (BAG-implanted rabbit bone), machining of aluminium, or gold removal for recycling purposes. However, as the sample or the use of ultrasound becomes more intricate (e.g. utilizing cavitation), the number of physical phenomena affecting the result also rises. To discuss these phenomena and their impact on the three applications in this study (gold removal, aluminium engraving, and CESAM imaging), the Discussion is divided into three sections.

In 5.1 Gold removal for e-waste recycling, the discussion is focused on HIFU, cavitation, and cavitation erosion, including the frequency-dependence of removal efficiency. In 5.2 Differences between gold and aluminium erosion, possible explanations for why aluminium is much easier to erode than gold are presented. In 5.3 CESAM, the factors affecting its output (e.g. tilt, scattering, frequency) and the reliability of the acoustic impedance values from the leporine bone sample are discussed, as well as CESAM's benefits compared to traditional SAMs.

## 5.1 Gold removal for e-waste recycling

The main focus of this dissertation was on removing gold from e-waste using HIFU (papers, A, I, and II). As the results show, gold was successfully removed (A, I, II), and the removal efficiency was increased 4.6 times by lowering the frequency from 11.8 MHz to 4.2 MHz (II). Furthermore, the material removal was restricted to only the gold pads by using a focused transducer, and the erosion depth could also be restricted to mainly the gold layer by controlling the number of sonicated bursts (I). Achieving the latter two aspects without added chemicals are an improvement from current hazardous e-waste recycling processes, i.e., pyro- and hydrometallurgy.

To discuss the gold removal method in detail, this section is divided into four subsections for readability. In 5.1.1, the benefits of HIFU and our method are presented. In 5.1.2 Cavitation for metal erosion, sonication parameters affecting the cavitation erosion and bubble (and bubble cloud) dynamics are discussed. The impact of frequency, based on the results from paper II, is discussed in 5.1.3

Frequency dependence, and finally future work and means of improvement are discussed in 5.1.4 Outlook.

### 5.1.1 Benefits of HIFU

HIFU-induced cavitation erosion has already found common use in biomedical research (e.g. [21, 51-55]). Cavitation erosion of metals has also been studied extensively, but mainly for the purpose of minimizing damage in hydrodynamically cavitating flows. While there are acoustic cavitation erosion studies on metals (e.g. [48, 57-59]), and even a measurement standard for acoustic cavitation erosion – the ASTM G-32 [85] (particularly Note 1, "stationary specimen tests") originally approved in 1972 (latest ed. 2021) – practical applications have yet to become widely available.

This dissertation presents a novel, practical HIFU-based cavitation erosion application: gold removal from e-waste for recycling purposes. In papers A, I, and II, we demonstrated that HIFU-induced cavitation erosion not only is able to remove gold from e-waste, but that the gold erosion can be controlled by easily tuneable sonication parameters: defocus distance and number of sonicated bursts (I and II). We also showed that a lower centre frequency can improve removal efficiency (II).

The applications most resembling ours found in the literature are the recent works by Jacobson *et al.* [13] (improved RPM recycling from e-waste with DES) and Watt *et al.* [60] (gold nanoparticles from a discarded SIM card). However, the 20 kHz sonotrodes with 6.4 mm tips used in those studies cannot provide the localization of HIFU (e.g., 140 µm lateral focal width of our 11.8 MHz transducer). On a PCB, a sonotrode would remove also the fibreglass-epoxy substrate surrounding the gold pads, as the pads are approx. 1 mm wide. In addition, as in Jacobson *et al.* [13], the high-power continuous-wave sonications of a sonotrode easily erodes through not only the gold, but the nickel and copper layers beneath as well. The need for pyro- and hydrometallurgic recycling processes stems from the presence of other metals and undesired materials (e.g. the substrate) in e-waste. As sonotrodes superfluously remove both the surrounding substrate, nickel and copper, the removed material still requires postprocessing. Hence, highly localized HIFU-induced cavitation erosion removing mainly gold (and possibly minute amounts of nickel) from an intact PCB is a significant improvement – especially as it can be done in water, without added chemicals. Furthermore, the HIFU-transducer also enables localizing (imaging) the gold pads prior to erosion and accurately determining transducer-sample distance. That cannot be done with a sonotrode.

### 5.1.2 Cavitation for metal erosion

Due to the many parameters and phenomena affecting the bubble cloud dynamics near a solid sample – for example, frequency, pressure amplitude, number of bursts, number of cycles per burst, defocus distance, PRF, gas content in the liquid, size and spatial distribution of bubble nuclei, shock waves, microjets, and the material – it is no wonder that acoustic cavitation has been labelled “deterministic chaos” [22, 23]. Fortunately, as the sound field is deterministic, producing cavitation erosion is not a totally random process.

In this dissertation, we confirmed three hypotheses relating to cavitation erosion of gold (and aluminium): 1) More gold was removed with more bursts (and engraving marks on aluminium widened and deepened with increased input energy), 2) the defocus distance plays a role, because it affects both the sound field, the bubble cloud dynamics, and their interactions, and 3) erosion was improved with a lower frequency. The effect of frequency and material is discussed further in sections 5.1.3 Frequency dependence and 5.2 Differences between gold and aluminium erosion. In this section, the impact of the other parameters is discussed.

Assuming that all parameters are constant, the number of cavitation events during one burst will vary due to the stochasticity of single-bubble collapse. But even so, the more bursts, the more cavitation erosion, because increasing the burst count is analogous with increasing deposited energy. Burst count is also a simple parameter to control, which is why it was chosen as a variable in our studies. While gold removal increased almost linearly with burst count, the removal efficiency (removed gold volume or mass divided by input electrical energy) displayed a peak (Figures 12 and 15). The peak occurs because when the nickel layer is reached, electricity is wasted on eroding nickel (and even copper with the 4.2 MHz transducer) instead of gold. Nonetheless, gold removal still continued in the outer area of the focal spots at higher burst counts (Figures 11, 13, and 14), even in the sidelobes, which was prominent with the 7.3 MHz transducer (Figure 13). This progression was also seen in the more sporadic and deep pitting of the 4.2 MHz transducer (Figure 13). Based on the results and as removing only gold (without nickel) would be desirable in a gold recycling application, it seems preferable to restrict the number of bursts to the efficiency peak and then move the transducer. This is in contrast to sonicating a long time in one spot to maximize the gold removal in that spot.

For single bubbles, the effects of standoff distance, $\gamma$, ($\gamma = d/R_{max}$) on bubble collapse and erosion marks have been studied extensively (e.g. [44-47, 56]). However, in the bubble cloud created in HIFU, the situation is much more complex. Here, the defocus distance directly affects the superposition of the incoming and reflected sound fields, which in turn affects where the bubble cloud forms and the dynamics of the bubbles within. In addition, the shock waves and microjets caused by imploding bubbles affect the cloud and the sound field [21, 49, 50, 86], influencing the optimal defocus distance. Determining the optimal defocus distance is thus best done experimentally for the sample type in question. In gold removal, we found that a slight positive defocus was optimal (+200 µm for 4.2 MHz and 11.8 MHz, +500 µm for 7.3 MHz). A previous study on erosion of a model kidney stone reached a similar result [87].

Surprisingly, a positive defocus distance is not always optimal. While aluminium erosion in papers B and C was performed at focus, our later (unpublished) experiments have shown that a negative defocus is optimal on samples of the same aluminium. This has proven to be the case with several different transducers, with optimal defocus for gold erosion always being positive. To determine the reason why, the cavitation cloud dynamics would need to be studied, e.g. with a high-resolution high-speed camera.

In the gold removal experiments, other sonication parameters whose effects were not investigated were pressure amplitude, number of cycles per burst, and PRF. They are, however, not insignificant and merit discussion.

In general, higher pressure amplitudes should produce more and increasingly powerful bubble collapses, aiding erosion. However, our pressure amplitudes were limited by the highest achievable output by the commercial amplifier. As the gold erosion experiments required millions of bursts even at the maximum amplitude, we excluded investigating lower amplitudes. On the other hand, as the 4.2 MHz transducer produced single deep pits reaching even the copper (Figure 13), using lower amplitudes might limit the deep pitting and produce more even erosion marks. In aluminium engraving, the amplitude was varied (Figure 18). Higher amplitudes produced more even, but thicker engraving lines, as a wider area of the focus exceeded the cavitation threshold. Thus, there was a trade-off between evenness and achievable detail.

At sufficiently high pressures, bubble collapse should occur after 1–2 cycles [35, 36, 88, 89]. Hence, longer bursts (i.e., more cycles within a burst) should induce more cavitation events and more erosion. However, in a bubble cloud, the situation is not straightforward, because bubbles also reflect sound. Hence, the outer bubbles of the cloud can cause bubble shielding [90], scattering part of the sound and decreasing pressure amplitudes at the sample surface. Shock waves from bubble collapse and reflections also generate new bubbles, which causes the cloud to grow towards the transducer [21, 86]. Thus, with long bursts, the cloud grows towards the transducer, causing increasing shielding and decreased erosion efficiency. To further complicate matters, this behaviour and/or its impact on erosion can also depend on defocus distance. As we had no means to monitor the cloud dynamics during sonication, we based our choice of burst length on other indicators. Our transducers settled into stable oscillation after approx. 20 cycles, whereby we selected 50 cycles per burst, which proved sufficient in preliminary tests. In aluminium engraving (paper C), the effect of number of cycles in a burst was explored (Figure 18). Increasing the number of cycles from 50 to 200 had an effect, but the impact of the number of passes (analogous to burst count in stationary sonication) was greater. Considering further that the burst count used for aluminium engraving corresponded to 10 000 bursts of stationary sonication, which is only 10 % of the lowest burst count producing any gold erosion, we concluded that a closer investigation into the effect of burst length on gold removal was not warranted.

In aluminium engraving (paper C), the PRF and engraving speed affected the evenness of the engraved line, which relates to spatial separation between pulses. However, when comparing the lines in Figure 17 made with the same speed, the PRF did not affect the erosion mark. Preliminary tests on gold revealed the same result. To increase gold removal speed, we did attempt to increase PRF, but this caused overheating and breaking of the thin curved piezo bowls. Hence, 500 Hz was used.

Apart from the sound parameters, the gas content of the water and size and spatial distribution of initial bubble nuclei affect cavitation. These were not monitored, though degassing of the purified water was done (30 min (paper I) to 1 h (paper II)) to obtain comparable gas contents between experiments. However, the gold erosion experiments took several hours to perform and thus the gas content did not remain constant throughout. Still, we observed no systematic differences between sonications performed in the beginning or end of experiments.

Attempts to navigate the myriad of parameters, interactions, and phenomena affecting cavitation erosion have given rise to a vast literature on cavitation and cavitation erosion. As no single equation or model yet exists to incorporate all effects, we elected for an empirical approach to determine the sonication parameters for our experimental work.

### 5.1.3 Frequency dependence

In paper II, we confirmed the hypothesis that gold removal efficiency could be improved by lowering the ultrasound frequency; by 4.6 and 3.8 times with the 4.2 MHz and 7.3 MHz transducers, respectively, compared to 11.8 MHz. The reasoning behind the hypothesis was that lower frequencies have lower cavitation thresholds, and that bubbles reach larger size and more violent collapse due to the longer growth phase. The discussion in the next paragraphs covers the fairness of comparison, the choice of frequencies, and details about the differences in erosion marks and their causes.

To compare the frequencies (4.2 MHz, 7.3 MHz, and 11.8 MHz), care was taken to build transducers that were as similar as possible, except in centre frequency. The curved piezo bowls were made from the same material (type Pz26), had the same geometry (19 mm element diameter, 15 mm focal distance), and were ordered from the same manufacturer (CTS Ferroperm, Denmark). They were electrically matched to 50 Ω to ensure maximum power transfer from the amplifier. Sonication parameters (amplitude, PRF, number of cycles, and burst count) were equal, except for frequency. Due to the longer period of the lower frequencies, this meant that the electrical input energy differed between transducers. To maintain constant input energy, either the number of cycles, amplitude, or a combination of both should have been altered. But as discussed in the previous section, changing the pressure amplitude alters the collapse of the bubbles and the number of cycles affects the cloud behaviour. Hence, the choice was made to keep these parameters constant and instead calculate removal efficiency (removed volume divided by the input electrical energy) to allow comparison.

The three frequencies were chosen as follows. The 11.8 MHz transducer was used in paper I and its high frequency and focusing allows high energy density at the focus and a small spot size (enabling removal from only the gold pads). When choosing the lowest frequency, the spot size had to be small enough to only affect the desired gold pad while having the same focusing geometry as the 11.8 MHz transducer. The ~500 µm spot size of the 4.2 MHz transducer is thus almost at the limit of the gold pads. Having selected the upper and lower frequencies, 7.3 MHz was chosen to be approximately in the middle of the range.

The erosion marks of the 7.3 MHz and 11.8 MHz transducers corresponded well to their focal zones (Figure 13), matching the FWHM+ at low burst counts and increasing towards FWHM−. Sidelobe cavitation was prominent with the 7.3 MHz transducer. As it is the rarefaction phase, i.e. the negative pressure, that drives bubble growth and collapse, one might wonder why the erosion marks at low burst counts matched the positive pressure profile (FWHM+). This can be explained by shock scattering [21, 86]. Due to nonlinear distortion, the compressive (positive) pressure in HIFU waves is higher than the rarefactive (negative), resulting in waveform distortion. As the first bubbles are generated, sound is reflected off them. This soft-boundary reflection causes the positive pressure to invert, resulting in a much larger negative pressure than the negative amplitude of the initial wave. This amplifies both the bubble expansion and collapse, and could explain why the initial erosion marks conform to the FWHM+. As the bubble cloud grows over successive acoustic cycles, the impact of shock scattering from the outermost bubbles decreases, causing the erosion mark to grow towards the FWHM−.

The erosion marks of the 4.2 MHz transducer differed markedly from those of the other transducers; they contained deep pitting reaching the copper layer and displayed a more erratic outline. The erosion began inside the FWHM+, as with the other transducers, which can thus also be attributed to shock scattering. At lower frequencies, the bubbles can grow larger, but the bubble density of the cloud decreases [91]. The reduced bubble density may allow the incident wave to penetrate deeper into the bubble cloud without being affected by bubble shielding.

The sporadic pits along the edge could be explained by the same factors, but in a somewhat more complicated sequence of events. When a bubble collapses, a toroidal ring of small rebound bubbles is usually formed. The size of the formed torus increases with the maximum radius of the imploded bubble [45], and thus decreases with frequency. Hence, the small rebound bubbles will be more dispersed for lower frequencies. These bubbles can then collapse and produce erosion during the subsequent cycles. Similar sporadic outer erosion marks have been observed in agarose tissue phantoms [91]. Secondary Bjerknes forces [92, 93] might also cause bubbles to accumulate more easily at larger bubble sizes, thus further explaining the occurrence of the larger sporadic marks in the outer regions seen mainly with the 4.2 MHz transducer.

As the erosion marks show, the improved gold removal efficiency is not only caused by a reduction in cavitation threshold or collapse of larger bubbles, but more intricate bubble dynamics also play a role.

### 5.1.4 Outlook

The presented gold removal technology has many advantages, mainly that it is environmentally friendly and uses only ultrasound and water, no harmful substances. Its main disadvantage is the long processing times. Lowering the frequency further from 4.2 MHz could reduce the cavitation threshold, but also increase the spot size too much to maintain removal selectivity. An alternative could be to use several transducers in an array, which could increase intensities further and ease the strain on the individual transducers.

Collecting the gold is the natural next step in developing this technology, but collecting gold particles from water is not novel in itself and was hence left out of the scope of this work. There exist many traditional gold separation methods, e.g., filtering, sedimentation, evaporation, and centrifugation. More novel methods also exist, e.g. nylon-based 3D-printed scavengers [94], amyloid nanofibril aerogels [95], and metal-organic frameworks (e.g. [96]). A localized sampling method described in [97], a sister project of our gold removal work, could also be used in conjunction with any aforementioned method to reduce the sampling water volume and ease post processing. Fortunately, nickel is magnetic, and thus minute amounts of unintentionally eroded nickel could be separated magnetically.

As demonstrated, our HIFU technology not only works on gold, but also on e.g. aluminium. It might therefore be useful for recycling other RPMs. The main restriction is that the removable material needs to be on the surface of the e-waste.

For paper I, a rough estimate of the profitability of the method was made. It was a simple calculation of dividing the monetary worth of the removed gold mass by the cost of the used electricity. This ratio was always >1 when any gold was removed, even considering a 40–60 % efficiency of the power amplifier. As this calculation was made for the 11.8 MHz transducer, with the lowest efficiency, this technology might become commercially viable in the future.

## 5.2 Differences between gold and aluminium erosion

Eroding aluminium required only a fraction, 2–3 %, of the burst count required for gold removal (frequency 11.8 MHz), even without impedance matching. For example, reaching erosion volumes exceeding 5 000 µm$^3$ required 8 000 bursts on aluminium compared to 250 000 bursts on gold (Figure 10b (Au), Figure 16 (Al)). While it is well known that materials have different cavitation erosion resistances, a conclusive description of which material properties that affect it the most remains elusive. In this section, select material parameters claimed to determine erosion resistance are presented and estimates for our gold and aluminium samples are given for two. In addition, detailed CESAM images of aluminium erosion from our other studies are shown, which provide some insight.

As stated by Sreedhar *et al.* in their comprehensive review article from 2017 [98], while cavitation erosion has been studied for almost a century, no single material parameter has yet been found to explain cavitation damage. Even curve fitting models with multiple parameters are limited in their predictions. A similar statement was also made by Karimi & Martin 30 years earlier [43]. Reviews on the quest for most predictive material properties can be found in e.g. [43, 98-100] (a convenient summary is given in Table 1 of [98]). Part of the problem is that different erosion tests can produce different results [43]. Another difficulty is to properly account for the high strain rates of cavitation erosion [98].

While there is no conclusive model, a few parameters have shown promise throughout the years: Vickers hardness (and other hardness measures), strain energy, ultimate resilience, fatigue strength coefficient, and a combination of Vickers hardness and fatigue-crack growth rate [43, 57, 98, 99, 101]. Even so, hardness continues to show most promise [99]. This is understandable, as hardness is a measure of the material's ability to withstand localized damage, usually measured by surface indentation – not a far cry from impacts from imploding bubbles.

To compare the erosion of our samples, their material properties must first be known. The aluminium used in this dissertation was AW-5754-H22. It is an aluminium-magnesium wrought alloy, that is tempered by strain hardening and partial annealing. Its material properties were chiefly retrieved from the open material database MatWeb [102]. The gold's properties, however, are not precisely known, as the sample was a piece from a discarded PCB of unknown origin. However, electroplated hard gold (EHG) is the most commonly used material in edge connectors [103], and thus assumed to be used on our sample. EHG contains less than 0.4 % (by weight) cobalt or nickel, has a polycrystalline structure with

20–30 nm grain size and Knoop hardness 170–200HK (kg/mm$^2$) (50–80HK for pure, soft gold) [103, 104].

AW-5754-H22 aluminium has a Vickers hardness (HV) of 75HV [102], which is higher than that of pure gold, 25HV [102], and thus should be more difficult to erode. However, pure gold is much softer than EHG. As EHG is a thin sample, reported hardnesses are in Knoop hardness, HK. Knoop hardness is similar to Vickers hardness in that both tests use a pyramidal indenter, but Knoop hardness is a microhardness test used on very thin or brittle samples. Reported Knoop hardness values for EHG are e.g. 160HK or 181HK, when containing nickel or cobalt, respectively [103]. While conversions between Knoop and Vickers hardness are only fully valid when using a test load of minimum 500 g, these values can be roughly converted to 147HV and 168HV, respectively. Comparing these values to aluminium (75HV), Vickers hardness could be a factor explaining why the aluminium was easier to erode.

Hattori & Nakao proposed that cavitation erosion should not be described by quasi-static material parameters, but should rather consider the fracture mechanism [101]. They investigated removed erosion particles from cavitation tests of steels to determine their fracture characteristics, with smaller particles signifying impact fracture and larger particles fatigue fracture. They thus proposed that both fracture types should be taken into account. With the removed particle volume decreasing as $\mathrm{HV}^{-3/2}$ and the fatigue-crack growth rate being proportional to $E^{-2}$ ($E$ is Young's modulus), they proposed that the volume loss rate by fatigue fracture, $V_{fa}$, is proportional to both terms, $V_{fa} \propto \mathrm{HV}^{-3/2}E^{-2}$. As erosion resistance is inversely proportional to volume loss, normalized values of $\mathrm{HV}^{3/2}E^2$ were calculated for our aluminium and gold samples (normalized by the value for aluminium): 1 for aluminium and 4.04 for EHG ($E$ for EHG was taken as the bulk value for gold from [102]). Based on these numbers, aluminium should be easier to erode. Pure gold again had a lower value than aluminium, 0.23.

Despite the multitude of material properties that have been investigated, and periodically claimed to most accurately predict cavitation erosion of some material (when measured with some cavitation test), the conclusion of the review by Krella from 2023 [99] was that hardness still remains one of the most successful parameters for predicting resistance to cavitation erosion. Furthermore, while the approach of Hattori & Nakao [101] directly considered fatigue, the fatigue limits of materials have also been separately described as a function of Vickers hardness (e.g. [105]). As discussed, these values could explain why EHG was more difficult to remove than aluminium in our studies.

It should also be noted that gold connectors are layered structures, where the underlying layers can affect both effective material properties and the reflected acoustic field, and subsequently bubble cloud dynamics (the pressure reflection coefficient at normal incidence is given in Equation 5). A study by Dular & Ohl found that cavitation damage from single laser-generated bubbles on a 9 µm thin aluminium foil depended on the substrate beneath [48]. Regardless of standoff distance of the bubble, the foil attached to PMMA suffered approx. 70 % less damage than that attached to $SiO_2$. They found that the softer PMMA substrate absorbed more sound from produced shock waves at bubble collapse, caused by PMMA having a lower acoustic impedance than $SiO_2$, i.e., a smaller impedance mismatch to water (1.5 MRayl). They concluded that cavitation damage is more violent when the reflection amplitude from the sample is larger (Equation 5). Unfortunately, acoustic impedance values ($Z$) for EHG (or speed of sound, $c$, as $Z = \rho c$) were not available. Pure gold has a higher acoustic impedance than aluminium, $Z_{Au,pure}$ = 62.5 MRayl, $Z_{Al}$ = 17.3 MRayl (densities and speeds of sound from [81]), which would suggest that removing gold should be easier than removing aluminium. However, the gold pads are layered structures (Figure 1), with gold, nickel, and copper layers on top of a fibreglass-epoxy substrate. While both nickel and copper have higher acoustic impedances than aluminium ($Z_{Ni}$ = 53.6 MRayl and $Z_{Cu}$ = 40.7 MRayl; densities from [102], speeds of sound from [81]), the fibreglass-epoxy substrate should have a lower acoustic impedance. A lower acoustic impedance of the PCB substrate compared to aluminium could explain why gold was more difficult to remove than aluminium.

A further possible explanation to why aluminium is easier to erode was discovered from CESAM images of aluminium erosion holes. An example is shown in Figure 22 (sonication parameters $f$ = 11.8 MHz, 10 000 bursts, defocus −800 µm, 80 cycles per burst, PRF = 250 Hz, maximum amplitude; imaging parameters as for all metal samples). In several instances, partially dislodged grains were visible at the edges of the erosion holes. These grains had risen slightly (a few µm) but not been completely removed. Such cracks forming perpendicular to the surface during cavitation erosion of aluminium agrees with the observations on cavitation erosion of aluminium alloys in [58].

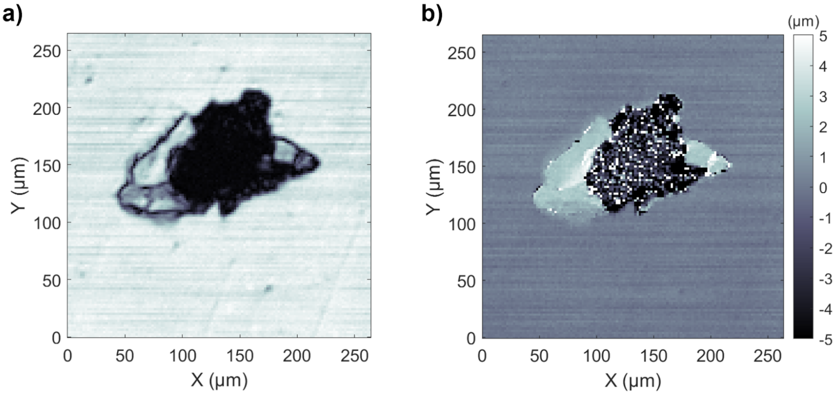

Figure 22 Partially dislodged grains from aluminium. a) CESAM amplitude map and b) CESAM topography map. The topography map reveals that the grains have risen from the sample by a few micrometers.

No such effect, i.e. seeing distinct grains partially dislodging, was observed in gold erosion holes. While both aluminium and gold are considered malleable, these images suggest that aluminium is more brittle than EHG, as it can break off in distinct grains. This could explain why aluminium is easier to erode than EHG.

## 5.3 CESAM

The imaging capability of our CESAM was previously quantified using USAF resolution samples and compared to standard SAM in [61]. However, hard samples are simple to image and hence the more extensive imaging capability of CESAM was explored in paper III on a complex sample containing both soft and hard materials: partially ossified BAG-implants in rabbit bone. CESAM's impedance and topography maps were validated against SEM-EDX and SWLI, respectively. CESAM can thus be used reliably on diverse samples and might enable future quantification of gold removal from soft substrates, e.g. from flexible electronics.

The benefits of CESAM in general are discussed in 5.3.1 Benefits of CESAM, while the factors affecting its output (e.g. tilt, scattering, frequency) and the reliability of the acoustic impedance values from the leporine bone sample are discussed in 5.3.2 Reliability of CESAM.

### 5.3.1 Benefits of CESAM

The benefit of all acoustic imaging compared to other imaging methods is that it truly probes mechanical properties. Despite its wide use in orthopaedics, X-rays probe density, which only partly affects mechanical properties. Furthermore, acoustic microscopy produces a topography map simultaneously with the amplitude map – basically two imaging modalities in one. As the amplitude map is more sensitive to surface changes, its contrast is usually better than the topography map's (for example, *cf.* Figure 6b and c or Figure 22a and b). On the other hand, the topography map was an excellent tool for measuring erosion volumes in paper I, A, B, and C. The greatest benefit is obtained by using both maps side by side, as the information contained in one can support drawing conclusions from the other. This was shown in Figure 21 (identifying ROIs related to bone formation) and Figure 22, where the topography map revealed that aluminium grains had partially dislodged.

The benefits of CESAM compared to traditional SAM is that the coded-excitation allows transmitting long signals without losing ToF resolution (even improving it, as shown in [61]). In traditional SAM, there is always a trade-off between SNR and ToF: shorter signals allow more accurate determination of ToF (high topography resolution), but shorter signals contain less energy resulting in poorer SNR (low amplitude resolution). The coded-excitation in CESAM circumvents this problem. The improved SNR brings another added benefit: reduced need for averaging. In traditional SAM, especially with soft samples, signal averaging is used in each scan point, which slows down imaging considerably. Paper III demonstrated that even as complex a sample as bone formation around BAG could be imaged using a single C-scan, without averaging.

### 5.3.2 Reliability of CESAM

The accuracy in determining ToF is not very sensitive to sample properties, as long as an echo is received – the amplitude (and calculated acoustic impedance), however, is. The reflected amplitude at each scan point contains the necessary information to calculate acoustic impedance (Equation 5). However, the amplitude can also be reduced by e.g. sample tilt, scattering due to surface roughness, or even an unsuitable wavelength (frequency) and/or focusing for the sample in question. The impact of these and their mitigation are discussed in the next paragraphs.

To ensure proper alignment and minimal tilt, B-scans (scan along one line) were performed over two orthogonal lines and the sample angle was adjusted with a goniometer until both lines were flat. Furthermore, any tilt would have been visible in the topography map (Figure 21b) as a colour gradient across the entire image. As no such gradient is present, the sample was properly aligned.

The frequency and focusing of the transducer determine the size of the focus. The lateral width affects the lateral resolution. The focal depth determines how large the height differences of the sample can be, before they cause scan points to be out of focus and thus have a lower amplitude. Hence, a longer focus allows larger height variations of the sample surface while still remaining in focus. However, a longer focus is also wider, decreasing the lateral resolution. The depth of focus of the 256 MHz transducer used in paper III was 49 µm. Thus, the observed height differences of approx. 10 µm were well within the focus. Steep notches, as seen in Regions (ii) and (vi) of Figure 20, still scatter sound due to the steep gradient.

Surface roughness is another source of scattering. Higher frequencies thus require more diligent polishing of the sample. Unfortunately, polishing biological samples is problematic, as softer matter is removed with greater ease than hard matter. Thus, some surface roughness always remains [73]. To properly account for surface roughness, a multilayer technique could be used, where the sample is imaged in many planes for each point. This can be beneficial in two ways: to ensure that each selected pixel is in focus [106] or to estimate the local inclinations in the vicinity of the pixel and accounting for it, as was done in [73]. As this was not done in paper III, acoustic impedance values might be underestimated in scattering areas.

The impact of frequency and focusing on the amplitude map is sample-dependent. For example, using a low frequency can cause averaging effects within the pixel, as was the case in [74]. Comparing images of human femoral cortical bone obtained with 25 MHz, 50 MHz, and 100 MHz SAM revealed that the wider focus of 25 MHz caused lateral averaging of the Haversian canals, thus decreasing the impedance estimate of the bone by 11 %. Then again, high frequencies are more sensitive to surface roughness. In [73], Raum *et al.* studied the effect of surface roughness on acoustic impedance estimates of proximal femoral cortical bone using a 900 MHz SAM. A 24 % reduction of impedance estimates was seen when not accounting for surface roughness. The 256 MHz centre frequency used in paper III was deemed a suitable compromise between sufficient lateral resolution (5.9 µm) and depth of focus (49 µm), i.e., not excessively sensitive to surface roughness.

To evaluate the reliability of CESAM's acoustic impedance values, they were compared to the literature. The relevant values from paper III were: $Z = (5.4 \pm 0.3)$ MRayl and $Z = (4.9 \pm 0.3)$ MRayl for bone mineral forming around the BAG granules (Regions (iii) and (vi) in Figure 20), and $Z = (2.4 \pm 0.4)$ MRayl for the probable non-mineralized bone tissue (Region (v) in Figure 20). These values matched acoustic impedances of newly formed bone tissue in leporine condyles, with impedances in the range of 4.2 MRayl to 6.9 MRayl [107]. As acoustic impedance values of leporine bone are scarce, comparisons were also made to acoustic impedance values of human bone. However, human bone differs from rabbit bone, and appears to be somewhat stiffer. Acoustic impedances of human femoral cortical bone is in the range of 5.1 MRayl to 9.3 MRayl, depending on age, sex, and SAM frequency [67, 73]. As our leporine bone sample was from the lateral femoral epicondyle, it should comprise trabecular bone, which is softer than cortical bone. Human trabecular bone samples embedded in PMMA have acoustic impedances of approx. 6 MRayl (6.2 MRayl in calcanei [108], 6.1 MHz in the femoral neck [75]), while fresh samples polished with P4000 sandpaper have acoustic impedances as low as $Z = (3.7 \pm 0.5)$ MRayl [75]. The probable non-mineralized bone tissue ($Z = (2.4 \pm 0.4)$ MRayl) resembled that of cartilage in human tibia, $Z = (2.12 \pm 0.02)$ MRayl [76].

Thus, the results from CESAM in paper III agree with literature values, despite consisting of a single C-scan without averaging. The acoustic impedance map was sufficient to differentiate between different tissues and materials, which was aided by the simultaneously produced topography map. The acoustic measures correlated with the other measurement modalities: acoustic impedance with SEM-EDX and topography with SWLI. Hence, CESAM can quantitatively image not only metal samples (USAF resolution sample in [61], cavitation erosion marks in papers I, A, B, and C), but also more complex soft samples (paper III).

# 6 Conclusion

The claim of this dissertation is that gold can be removed from e-waste, from solely predetermined areas, using only HIFU-induced cavitation erosion in water (i.e. without added chemicals). This was demonstrated in papers A, I, and II.

The drawbacks of current e-waste recycling methods stem from the need to separate RPMs from other materials. Thus, to truly add value, our HIFU-method should remove other materials in minimal quantities. The tight focus of the HIFU transducer (140 µm to 500 µm, for 11.8 MHz and 4.2 MHz, respectively) ensures that the cavitation erosion occurs only on the gold pads. In paper I, controlling the erosion depth by controlling the number of sonicated bursts was explored, which showed that nickel removal was minimal (or non-existent) with a suitable burst count.

In paper II, gold removal efficiency was increased by lowering the frequency: efficiency increased by a factor of 3.8 and 4.6 compared to 11.8 MHz when using 7.3 MHz or 4.2 MHz, respectively. The 4.2 MHz transducer produced small deep pits, some penetrating to the copper, and thus, while being the most effective, still requires optimization to reduce the amount of removed nickel and copper.

The HIFU metal removal method was also tested for aluminium machining (papers B, C). This confirmed our hypothesis that the method can be extended to other metals as well. Thus, it could be suitable for removing other RPMs from surfaces.

As quantification of the cavitation erosion was done with CESAM, its imaging capability was evaluated on a more complex sample (the partially ossified BAG bone implant) and evaluated against two other imaging modalities (SWLI and SEM-EDX) in paper III. The results served to cement our confidence in its quantitative imaging capability.

With massive amounts of e-waste being generated each year, current e-waste recycling methods having significant disadvantages, natural gold reserves diminishing, and less than 2 % of annual gold production coming from e-waste, new and improved gold recycling methods for e-waste are needed. Thus, the results from this dissertation are both timely and have the potential to make a real impact.

# References

[1] Cornelis P. Baldé, Ruediger Kuehr, Tales Yamamoto, Rosie McDonald, Elena D'Angelo, Shahana Althaf, Garam Bel, Otmar Deubzer, Elena Fernandez-Cubillo, Vanessa Forti, Vanessa Gray, Sunil Herat, Shunichi Honda, Giulia Iattoni, Deepali S. Khetriwal, Vittoria Luda di Cortemiglia, Yuliya and I. N. Lobuntsova, Noémie Pralat, Michelle Wagner, "Global E-waste Monitor 2024," International Telecommunication Union (ITU) and United Nations Institute for Training and Research (UNITAR), 2024.

[2] M. Wang, Q. Tan, J. F. Chiang, and J. Li, "Recovery of rare and precious metals from urban mines—A review," *Frontiers of Environmental Science & Engineering,* vol. 11, no. 5, pp. 1-17, 2017, doi: https://doi.org/10.1007/s11783-017-0963-1.

[3] X. Zeng, J. A. Mathews, and J. Li, "Urban mining of e-waste is becoming more cost-effective than virgin mining," *Environmental science & technology,* vol. 52, no. 8, pp. 4835-4841, 2018, doi: https://doi.org/10.1021/acs.est.7b04909.

[4] A. Mairizal, A. Sembada, K. Tse, N. Haque, and M. Rhamdhani, "Techno-economic analysis of waste PCB recycling in Australia," *Resources, Conservation and Recycling,* vol. 190, 2023, Art no. 106784, doi: https://doi.org/10.1016/j.resconrec.2022.106784.

[5] U.S. Geological Survey *Mineral commodity summaries 2025 (ver. 1.2, March 2025).* U.S. Geological Survey, U.S. Department of the Interior, Reston, Virginia, 2025, pp. 82-83.

[6] "Gold Focus 2020," Metals Focus, 2020. Accessed: 16.4.2025. [Online]. Available: https://www.metalsfocus.com/wp-content/uploads/2020/11/GOLD-FOCUS-2020.pdf

[7] *Precious Metals E-Waste Recovery Market: Global Forecast to 2025.* Markets and Markets, 2020.

[8] J. Cui and L. Zhang, "Metallurgical recovery of metals from electronic waste: A review," *Journal of hazardous materials,* vol. 158, no. 2-3, pp. 228-256, 2008, doi: https://doi.org/10.1016/j.jhazmat.2008.02.001.

[9] L. H. Xavier, M. Ottoni, and L. P. P. Abreu, "A comprehensive review of urban mining and the value recovery from e-waste materials," *Resources, Conservation and Recycling,* vol. 190, 2023, Art no. 106840, doi: https://doi.org/10.1016/j.resconrec.2022.106840.

[10] A. Zupanc *et al.*, "Sequential Selective Dissolution of Coinage Metals in Recyclable Ionic Media," *Angewandte Chemie,* 2024, Art no. e202407147, doi: https://doi.org/10.1002/ange.202407147.

[11] M. Baniasadi, F. Vakilchap, N. Bahaloo-Horeh, S. M. Mousavi, and S. Farnaud, "Advances in bioleaching as a sustainable method for metal recovery from e-waste: a review," *Journal of Industrial and Engineering*

*Chemistry,* vol. 76, pp. 75-90, 2019, doi: https://doi.org/10.1016/j.jiec.2019.03.047.

[12] M. Guo, R. Deng, M. Gao, C. Xu, and Q. Zhang, "Sustainable Recovery of Metals from E-Waste Using Deep Eutectic Solvents: Advances, Challenges, and Perspectives," *Current Opinion in Green and Sustainable Chemistry,* 2024, Art no. 100913, doi: https://doi.org/10.1016/j.cogsc.2024.100913.

[13] B. Jacobson *et al.*, "A mechanistic study identifying improved technology critical metal delamination from printed circuit boards at lower power sonications in a deep eutectic solvent," *Ultrasonics Sonochemistry,* vol. 101, 2023, Art no. 106701, doi: https://doi.org/10.1016/j.ultsonch.2023.106701.

[14] D. Ensminger and L. J. Bond, "Ultrasonics: Fundamentals, Technologies, and Applications," 3rd ed. Boca Raton: CRC Press, 2011, ch. 2.12.1 Cavitation, pp. 95-97.

[15] D. Ensminger and L. J. Bond, "Ultrasonics: Fundamentals, Technologies, and Applications," 3rd ed. Boca Raton: CRC Press, 2011, ch. 11 Applications of High-Intensity Ultrasonics - Basic Mechanisms and Effects, pp. 459-460.

[16] K. Yasui, "Dynamics of Acoustic Bubbles," in *Sonochemistry and the Acoustic Bubble*, F. Grieser, P.-K. Choi, N. Enomoto, H. Harada, K. Okitsu, and K. Yasui Eds.: Elsevier, 2015, ch. 3: Dynamics of Acoustic Bubbles, pp. 41-83.

[17] J. I. Thornycroft and S. W. Barnaby, "Torpedo-Boat Destroyers," in *Minutes of the Proceedings of the Institution of Civil Engineers*, 1895, vol. 122, no. 1895: Thomas Telford-ICE Virtual Library, pp. 51-69.

[18] O. Silberrad, "Propeller erosion," *Engineering,* vol. 93, pp. 33-35, 1912. [Online]. Available: https://archive.org/details/sim_engineering_january-june-1912_93/page/n41/mode/2up.

[19] A. Bouakaz, A. Zeghimi, and A. A. Doinikov, "Sonoporation: Concept and mechanisms," in *Therapeutic Ultrasound*, vol. 880, J.-M. Escoffre and A. Bouakaz Eds., (Advances in Experimental Medicine and Biology: Springer, 2016, ch. 10, pp. 175-189.

[20] R. Suzuki and A. L. Klibanov, "Co-administration of Microbubbles and Drugs in Ultrasound-Assisted Drug Delivery: Comparison with Drug- Carrying Particles," in *Therapeutic Ultrasound*, vol. 880, J.-M. Escoffre and A. Bouakaz Eds., (Therapeutic Ultrasound: Springer, 2016, ch. 12, pp. 205-220.

[21] K. B. Bader, E. Vlaisavljevich, and A. D. Maxwell, "For whom the bubble grows: physical principles of bubble nucleation and dynamics in histotripsy ultrasound therapy," *Ultrasound in medicine & biology,* vol. 45, no. 5, pp. 1056-1080, 2019, doi: https://doi.org/10.1016/j.ultrasmedbio.2018.10.035.

[22] W. Lauterborn and R. Mettin, "Acoustic cavitation: Bubble dynamics in high-power ultrasonic fields: Single-bubble dynamics," in *Power Ultrasonics - Applications of High-Intensity Ultrasound*, J. A. Gallego-Juárez, K. F. Graff, and M. Lucas Eds., 2nd ed. (Woodhead Publishing Series in Electronic and Optical Materials: Woodhead Publishing, Elsevier, 2023, ch. 3.3, p. 30.

[23] W. Lauterborn and R. Mettin, "Acoustic cavitation: Bubble dynamics in high-power ultrasonic fields: Acoustic cavitation noise," in *Power Ultrasonics - Applications of High-Intensity Ultrasound*, J. A. Gallego-Juárez, K. F. Graff, and M. Lucas Eds., 2nd ed. (Woodhead Publishing Series in Electronic and Optical Materials: Woodhead Publishing, Elsevier, 2023, ch. 3.5, p. 43.

[24] R. E. Apfel, "Acoustic cavitation inception," *Ultrasonics,* vol. 22, no. 4, pp. 167-173, 1984, doi: https://doi.org/10.1016/0041-624X(84)90032-5.

[25] Lord Rayleigh, "VIII. On the pressure developed in a liquid during the collapse of a spherical cavity," *The London, Edinburgh, and Dublin Philosophical Magazine and Journal of Science,* vol. 34, no. 200, pp. 94-98, 1917.

[26] M. S. Plesset, "The dynamics of cavitation bubbles," *Journal of Applied Mechanics,* vol. 6, pp. 277-282, 1949, doi: https://doi.org/10.1115/1.4009975.

[27] B. E. Noltingk and E. A. Neppiras, "Cavitation produced by ultrasonics," *Proceedings of the Physical Society. Section B,* vol. 63, no. 9, pp. 674-685, 1950, doi: https://doi.org/10.1088/0370-1301/63/9/305.

[28] H. Poritsky, "The collapse or growth of a spherical bubble or cavity in a viscous fluid," in *Proceedings of the First US National Congress on Applied Mechanics*, E. Sternberg, Ed., 1952: New York, pp. 813-821.

[29] A. J. Walton and G. T. Reynolds, "Sonoluminescence," *Advances in physics,* vol. 33, no. 6, pp. 595-660, 1984, doi: https://doi.org/10.1080/00018738400101711.

[30] A. Prosperetti and A. Lezzi, "Bubble dynamics in a compressible liquid. Part 1. First-order theory," *Journal of Fluid Mechanics,* vol. 168, pp. 457-478, 1986, doi: https://doi.org/10.1017/S0022112086000460.

[31] A. Zhang, S.-M. Li, P. Cui, S. Li, and Y.-L. Liu, "A unified theory for bubble dynamics," *Physics of Fluids,* vol. 35, no. 3, 2023, Art no. 033323, doi: https://doi.org/10.1063/5.0145415.

[32] F. G. Blake, "The onset of cavitation in liquids," in *Technical Memo 12*. Acoustics Research Laboratory, Harvard University, Cambridge, MA, 1949.

[33] M. Minnaert, "XVI. On musical air-bubbles and the sounds of running water," *The London, Edinburgh, and Dublin Philosophical Magazine and Journal of Science,* vol. 16, no. 104, pp. 235-248, 1933, doi: https://doi.org/10.1080/14786443309462277.

[34] R. E. Apfel, "Acoustic cavitation prediction," *The Journal of the Acoustical Society of America,* vol. 69, no. 6, pp. 1624-1633, 1981, doi: https://doi.org/10.1121/1.385939.

[35] R. E. Apfel, "Possibility of microcavitation from diagnostic ultrasound," *IEEE Transactions on Ultrasonics, Ferroelectrics, and Frequency Control,* vol. 33, no. 2, pp. 139-142, 1986, doi: https://doi.org/10.1109/T-UFFC.1986.26805.

[36] C. K. Holland and R. E. Apfel, "An improved theory for the prediction of microcavitation thresholds," *IEEE transactions on ultrasonics, ferroelectrics, and frequency control,* vol. 36, no. 2, pp. 204-208, 1989, doi: https://doi.org/10.1109/58.19152.

[37] K. Yasui, "Dynamics of Acoustic Bubbles," in *Sonochemistry and the Acoustic Bubble*, F. Grieser, P.-K. Choi, N. Enomoto, H. Harada, K. Okitsu, and K. Yasui Eds.: Elsevier, 2015, ch. 3: Dynamics of Acoustic Bubbles, eq. (3.40), p. 58.

[38] J. Ma, C.-T. Hsiao, and G. L. Chahine, "Euler–Lagrange simulations of bubble cloud dynamics near a wall," *Journal of Fluids Engineering,* vol. 137, no. 4, 2015, Art no. 041301, doi: https://doi.org/10.1115/1.4028853.

[39] J. Ma, C.-T. Hsiao, and G. L. Chahine, "Numerical study of acoustically driven bubble cloud dynamics near a rigid wall," *Ultrasonics sonochemistry,*

vol. 40, pp. 944-954, 2018, doi: https://doi.org/10.1016/j.ultsonch.2017.08.033.

[40] K. Maeda and T. Colonius, "Eulerian–Lagrangian method for simulation of cloud cavitation," *Journal of computational physics,* vol. 371, pp. 994-1017, 2018, doi: https://doi.org/10.1016/j.jcp.2018.05.029.

[41] A. Vogel and W. Lauterborn, "Acoustic transient generation by laser-produced cavitation bubbles near solid boundaries," *The Journal of the Acoustical Society of America,* vol. 84, no. 2, pp. 719-731, 1988, doi: https://doi.org/10.1121/1.396852.

[42] M. Kornfeld and L. Suvorov, "On the destructive action of cavitation," *Journal of Applied Physics,* vol. 15, no. 6, pp. 495-506, 1944, doi: https://doi.org/10.1063/1.1707461.

[43] A. Karimi and J. Martin, "Cavitation erosion of materials," *International Metals Reviews,* vol. 31, no. 1, pp. 1-26, 1986, doi: https://doi.org/10.1179/imtr.1986.31.1.1.

[44] Y. Tomita and A. Shima, "Mechanisms of impulsive pressure generation and damage pit formation by bubble collapse," *Journal of Fluid Mechanics,* vol. 169, pp. 535-564, 1986, doi: https://doi.org/10.1017/S0022112086000745.

[45] A. Philipp and W. Lauterborn, "Cavitation erosion by single laser-produced bubbles," *Journal of fluid mechanics,* vol. 361, pp. 75-116, 1998, doi: https://doi.org/10.1017/S0022112098008738.

[46] M. Dular, T. Požar, J. Zevnik, and R. Petkovšek, "High speed observation of damage created by a collapse of a single cavitation bubble," *Wear,* vol. 418, pp. 13-23, 2019, doi: https://doi.org/10.1016/j.wear.2018.11.004.

[47] F. Reuter, C. Deiter, and C.-D. Ohl, "Cavitation erosion by shockwave self-focusing of a single bubble," *Ultrasonics sonochemistry,* vol. 90, 2022, Art no. 106131, doi: https://doi.org/10.1016/j.ultsonch.2022.106131.

[48] M. Dular and C. D. Ohl, "Bulk material influence on the aggressiveness of cavitation–Questioning the microjet impact influence and suggesting a possible way to erosion mitigation," *Wear,* vol. 530, 2023, Art no. 205061, doi: https://doi.org/10.1016/j.wear.2023.205061.

[49] L. van Wijngaarden, "Mechanics of collapsing cavitation bubbles," *Ultrasonics sonochemistry,* vol. 29, pp. 524-527, 2016, doi: https://doi.org/10.1016/j.ultsonch.2015.04.006.

[50] E. Brujan, T. Ikeda, K. Yoshinaka, and Y. Matsumoto, "The final stage of the collapse of a cloud of bubbles close to a rigid boundary," *Ultrasonics sonochemistry,* vol. 18, no. 1, pp. 59-64, 2011, doi: https://doi.org/10.1016/j.ultsonch.2010.07.004.

[51] V. A. Khokhlova *et al.*, "Histotripsy methods in mechanical disintegration of tissue: Towards clinical applications," *International journal of hyperthermia,* vol. 31, no. 2, pp. 145-162, 2015, doi: https://doi.org/10.3109/02656736.2015.1007538.

[52] Z. Xu, T. L. Hall, E. Vlaisavljevich, and F. T. Lee Jr, "Histotripsy: the first noninvasive, non-ionizing, non-thermal ablation technique based on ultrasound," *International journal of hyperthermia,* vol. 38, no. 1, pp. 561-575, 2021, doi: https://doi.org/10.1080/02656736.2021.1905189.

[53] A. S. Sehmbi *et al.*, "Systematic review of the role of high intensity focused ultrasound (HIFU) in treating malignant lesions of the hepatobiliary system," *HPB,* vol. 23, no. 2, pp. 187-196, 2021, doi: https://doi.org/10.1016/j.hpb.2020.06.013.

[54] S. Yoshizawa, T. Ikeda, A. Ito, R. Ota, S. Takagi, and Y. Matsumoto, "High intensity focused ultrasound lithotripsy with cavitating microbubbles," *Medical & biological engineering & computing,* vol. 47, no. 8, pp. 851-860, 2009, doi: https://doi.org/10.1007/s11517-009-0471-y.

[55] T. Ikeda, S. Yoshizawa, N. Koizumi, M. Mitsuishi, and Y. Matsumoto, "Focused ultrasound and lithotripsy," in *Therapeutic Ultrasound*, vol. 880, J.-M. Escoffre and A. Bouakaz Eds., (Advances in Experimental Medicine and Biology: Springer, 2016, ch. 7, pp. 113-129.

[56] H. J. Sagar and O. el Moctar, "Dynamics of a cavitation bubble near a solid surface and the induced damage," *Journal of Fluids and Structures,* vol. 92, 2020, Art no. 102799, doi: https://doi.org/10.1016/j.jfluidstructs.2019.102799.

[57] R. Richman and W. McNaughton, "Correlation of cavitation erosion behavior with mechanical properties of metals," *Wear,* vol. 140, no. 1, pp. 63-82, 1990, doi: https://doi.org/10.1016/0043-1648(90)90122-Q.

[58] W. Tomlinson and S. Matthews, "Cavitation erosion of aluminium alloys," *Journal of materials science,* vol. 29, no. 4, pp. 1101-1108, 1994, doi: https://doi.org/10.1007/BF00351438.

[59] M. Dular, O. C. Delgosha, and M. Petkovšek, "Observations of cavitation erosion pit formation," *Ultrasonics sonochemistry,* vol. 20, no. 4, pp. 1113-1120, 2013, doi: https://doi.org/10.1016/j.ultsonch.2013.01.011.

[60] J. Watt *et al.*, "Formation of Metal Nanoparticles Directly from Bulk Sources Using Ultrasound and Application to E-Waste Upcycling," *Small,* vol. 14, no. 17, 2018, Art no. 1703615, doi: https://doi.org/10.1002/smll.201703615.

[61] A. Meriläinen, J. Hyvönen, A. Salmi, and E. Hæggström, "CESAM—Coded excitation scanning acoustic microscope," *Review of Scientific Instruments,* vol. 92, no. 7, 2021, Art no. 074901, doi: https://doi.org/10.1063/5.0047351.

[62] R. K. Baruah, H. Yoo, and E. K. Lee, "Interconnection technologies for flexible electronics: Materials, fabrications, and applications," *Micromachines,* vol. 14, no. 6, 2023, Art no. 1131, doi: https://doi.org/10.3390/mi14061131.

[63] Fortune Business Insights, "Flexible Electronics Market Size, Share & Industry Analysis, By Type (Flexible Printed Circuits and Rigid-Flexible), By Application (Monitoring, Sensing, Lighting, Display, Storage, and Others (Sensors)), By End-user (Consumer Goods, Healthcare, Automotive, Robotics, Agriculture, Aerospace and Defense, and Others (Energy and Power), and Regional Forecast, 2025 – 2032," in "Semiconductor & Electronics Market Research Report," 2025. Accessed: 25.5.2025. [Online]. Available: https://www.fortunebusinessinsights.com/flexible-electronics-market-109105

[64] Fortune Business Insights, "Consumer Electronics Market Size, Share & Industry Analysis, By Product Type (Electronic Devices (Television, Computer, Digital Camera & Camcorder, and Others) and Home Appliances (Refrigerator, Washing Machine, Air Conditioner, and Others)), Distribution Channel (Offline and Online), and Regional Forecast, 2025-2032," in "Appliances Market Research Report," 2025. Accessed: 25.5.2025. [Online]. Available: https://www.fortunebusinessinsights.com/consumer-electronics-market-104693

[65] L. L. Hench and H. Paschall, "Direct chemical bond of bioactive glass-ceramic materials to bone and muscle," *Journal of biomedical materials*

*research,* vol. 7, no. 3, pp. 25-42, 1973, doi: https://doi.org/10.1002/jbm.820070304.

[66] L. L. Hench, "The story of Bioglass®," *Journal of Materials Science: Materials in Medicine,* vol. 17, no. 11, pp. 967-978, 2006, doi: https://doi.org/10.1007/s10856-006-0432-z.

[67] K. Raum, R. O. Cleveland, F. Peyrin, and P. Laugier, "Derivation of elastic stiffness from site-matched mineral density and acoustic impedance maps," *Physics in Medicine & Biology,* vol. 51, no. 3, pp. 747-758, 2006, doi: https://doi.org/10.1088/0031-9155/51/3/018.

[68] K. Raum *et al.*, "Site-matched assessment of structural and tissue properties of cortical bone using scanning acoustic microscopy and synchrotron radiation μCT," *Physics in Medicine & Biology,* vol. 51, no. 3, pp. 733-746, 2006, doi: https://doi.org/10.1088/0031-9155/51/3/017.

[69] R. Lemons and C. F. Quate, "Acoustic microscope—scanning version," *Applied Physics Letters,* vol. 24, no. 4, pp. 163-165, 1974, doi: https://doi.org/10.1063/1.1655136.

[70] J. D. N. Cheeke, "Fundamentals and applications of ultrasonic waves." Boca Raton: CRC Press, 2002, ch. 14.1 Acoustic microscopy: Introduction, pp. 297-303.

[71] G. A. D. Briggs and O. V. Kolosov, "Acoustic Microscopy," 2nd ed. New York: Oxford University Press, 2010, ch. 4.2 Surface imaging, pp. 52-57.

[72] L. Smitmans, K. Raum, J. Brandt, and A. Klemenz, "Variations in the microstructural acousto-mechanical properties of cortical bone revealed by a quantitative acoustic microscopy study," in *2000 IEEE Ultrasonics Symposium. Proceedings. An International Symposium (Cat. No. 00CH37121),* 2000, vol. 2: IEEE, pp. 1379-1382, doi: https://doi.org/10.1109/ULTSYM.2000.921579.

[73] K. Raum, K. V. Jenderka, A. Klemenz, and J. Brandt, "Multilayer analysis: Quantitative scanning acoustic microscopy for tissue characterization at a microscopic scale," *IEEE transactions on ultrasonics, ferroelectrics, and frequency control,* vol. 50, no. 5, pp. 507-516, 2003, doi: https://doi.org/10.1109/TUFFC.2003.1201463.

[74] K. Raum, J. Reißhauer, and J. Brandt, "Frequency and resolution dependence of the anisotropic impedance estimation in cortical bone using time-resolved scanning acoustic microscopy," *Journal of Biomedical Materials Research Part A,* vol. 71, no. 3, pp. 430-438, 2004, doi: https://doi.org/10.1002/jbm.a.30156.

[75] X. Ojanen, J. Töyräs, S. I. Inkinen, M. K. Malo, H. Isaksson, and J. S. Jurvelin, "Differences in acoustic impedance of fresh and embedded human trabecular bone samples—Scanning acoustic microscopy and numerical evaluation," *The Journal of the Acoustical Society of America,* vol. 140, no. 3, pp. 1931-1936, 2016, doi: https://doi.org/10.1121/1.4962347.

[76] S. Leicht and K. Raum, "Acoustic impedance changes in cartilage and subchondral bone due to primary arthrosis," *Ultrasonics,* vol. 48, no. 6-7, pp. 613-620, 2008, doi: https://doi.org/10.1016/j.ultras.2008.04.012.

[77] Y. Hagiwara, A. Ando, E. Chimoto, Y. Saijo, K. Ohmori-Matsuda, and E. Itoi, "Changes of articular cartilage after immobilization in a rat knee contracture model," *Journal of Orthopaedic Research,* vol. 27, no. 2, pp. 236-242, 2009, doi: https://doi.org/10.1002/jor.20724.

[78] Y. Hagiwara *et al.*, "Comparison of articular cartilage images assessed by high-frequency ultrasound microscope and scanning acoustic microscope," *International orthopaedics,* vol. 36, no. 1, pp. 185-190, 2012, doi: https://doi.org/10.1007/s00264-011-1263-1.

[79] G. A. D. Briggs and O. V. Kolosov, "Acoustic Microscopy," 2nd ed. New York: Oxford University Press, 2010, ch. 2.3 Reflection acoustic microscopy, pp. 22-25.

[80] N. Sandler, I. Kassamakov, H. Ehlers, N. Genina, T. Ylitalo, and E. Haeggstrom, "Rapid interferometric imaging of printed drug laden multilayer structures," *Scientific reports,* vol. 4, 2014, Art no. 4020, doi: https://doi.org/10.1038/srep04020.

[81] D. R. Lide, Ed. *CRC Handbook of Chemistry and Physics*, 84 ed. Boca Raton: CRC Press, 2003.

[82] R. Björkenheim *et al.*, "Polymer-coated bioactive glass S53P4 increases VEGF and TNF expression in an induced membrane model in vivo," *Journal of Materials Science,* vol. 52, no. 15, pp. 9055-9065, 2017, doi: https://doi.org/10.1007/s10853-017-0839-6.

[83] R. Björkenheim *et al.*, "Bone morphogenic protein expression and bone formation are induced by bioactive glass S53P4 scaffolds in vivo," *Journal of Biomedical Materials Research Part B: Applied Biomaterials,* vol. 107, no. 3, pp. 847-857, 2019, doi: https://doi.org/10.1002/jbm.b.34181.

[84] *Water Speed of Sound: Datasheet from "Dortmund Data Bank (DDB) – Thermophysical Properties Edition 2014" in SpringerMaterials (https://materials.springer.com/thermophysical/docs/sos_c174).* Springer-Verlag Berlin Heidelberg & DDBST GmbH, Oldenburg, Germany. [Online]. Available: https://materials.springer.com/thermophysical/docs/sos_c174

[85] *ASTM G-32 Standard: Standard Test Method for Cavitation Erosion Using Vibratory Apparatus*, ASTM International, 100 Barr Harbor Drive, PO Box C700, West Conshohocken, PA 19428-2959. United States.

[86] A. D. Maxwell *et al.*, "Cavitation clouds created by shock scattering from bubbles during histotripsy," *The Journal of the Acoustical Society of America,* vol. 130, no. 4, pp. 1888-1898, 2011, doi: https://doi.org/10.1121/1.3625239.

[87] L. Biasiori-Poulanges, B. Lukić, and O. Supponen, "Cavitation cloud formation and surface damage of a model stone in a high-intensity focused ultrasound field," *Ultrasonics Sonochemistry,* vol. 102, 2024, Art no. 106738, doi: https://doi.org/10.1016/j.ultsonch.2023.106738.

[88] O. V. Abramov, "Figure 2.16," in *High-Intensity Ultrasonics: Theory and application*. Amsterdam: Gordon and Breach Science Publishers, 1998, ch. 2.2 Acoustic cavitation, p. 94.

[89] R. E. Apfel and C. K. Holland, "Gauging the likelihood of cavitation from short-pulse, low-duty cycle diagnostic ultrasound," *Ultrasound in medicine & biology,* vol. 17, no. 2, pp. 179-185, 1991, doi: https://doi.org/10.1016/0301-5629(91)90125-G.

[90] K. Maeda, A. D. Maxwell, T. Colonius, W. Kreider, and M. R. Bailey, "Energy shielding by cavitation bubble clouds in burst wave lithotripsy," *The Journal of the Acoustical Society of America,* vol. 144, no. 5, pp. 2952-2961, 2018, doi: https://doi.org/10.1121/1.5079641.

[91] C. Edsall, E. Ham, H. Holmes, T. L. Hall, and E. Vlaisavljevich, "Effects of frequency on bubble-cloud behavior and ablation efficiency in intrinsic threshold histotripsy," *Physics in Medicine & Biology,* vol. 66, no. 22, 2021, Art no. 225009, doi: https://doi.org/10.1088/1361-6560/ac33ed.

[92] L. A. Crum, "Bjerknes forces on bubbles in a stationary sound field," *The Journal of the Acoustical Society of America,* vol. 57, no. 6, pp. 1363-1370, 1975, doi: https://doi.org/10.1121/1.380614.

[93] M. Lanoy, C. Derec, A. Tourin, and V. Leroy, "Manipulating bubbles with secondary Bjerknes forces," *Applied Physics Letters,* vol. 107, no. 21, 2015, Art no. 214101, doi: https://doi.org/10.1063/1.4936259.

[94] E. Lahtinen, L. Kivijärvi, R. Tatikonda, A. Väisänen, K. Rissanen, and M. Haukka, "Selective recovery of gold from electronic waste using 3D-printed scavenger," *ACS omega,* vol. 2, no. 10, pp. 7299-7304, 2017, doi: https://doi.org/10.1021/acsomega.7b01215.

[95] M. Peydayesh, E. Boschi, F. Donat, and R. Mezzenga, "Gold Recovery from E-Waste by Food-waste Amyloid Aerogels," *Advanced Materials,* 2024, Art no. 2310642, doi: https://doi.org/10.1002/adma.202310642.

[96] T. Xue *et al.*, "A customized MOF-polymer composite for rapid gold extraction from water matrices," *Science Advances,* vol. 9, no. 13, 2023, Art no. eadg4923, doi: https://doi.org/10.1126/sciadv.adg4923.

[97] T. Sillanpää *et al.*, "Ultrasound-based surface sampling in immersion for mass spectrometry," *Journal of Applied Physics,* vol. 134, no. 10, 2023, Art no. 104901, doi: https://doi.org/10.1063/5.0157705.

[98] B. Sreedhar, S. a. Albert, and A. Pandit, "Cavitation damage: Theory and measurements–A review," *Wear,* vol. 372, pp. 177-196, 2017, doi: https://doi.org/10.1016/j.wear.2016.12.009.

[99] A. K. Krella, "Degradation and protection of materials from cavitation erosion: a review," *Materials,* vol. 16, no. 5, 2023, Art no. 2058, doi: https://doi.org/10.3390/ma16052058.

[100] K.-H. Kim, G. Chahine, J.-P. Franc, and A. Karimi, Eds. *Advanced Experimental and Numerical Techniques for Cavitation Erosion Prediction* (Fluid Mechanics and Its Applications, no. 106). Dordrecht: Springer, 2014.

[101] S. Hattori and E. Nakao, "Cavitation erosion mechanisms and quantitative evaluation based on erosion particles," *Wear,* vol. 249, no. 10-11, pp. 839-845, 2001, doi: https://doi.org/10.1016/S0043-1648(00)00308-2.

[102] MatWeb. "Matweb Material property data." http://www.matweb.com/ (accessed 25 April, 2025).

[103] N. Togasaki, Y. Okinaka, T. Homma, and T. Osaka, "Preparation and characterization of electroplated amorphous gold–nickel alloy film for electrical contact applications," *Electrochimica acta,* vol. 51, no. 5, pp. 882-887, 2005, doi: https://doi.org/10.1016/j.electacta.2005.04.057.

[104] Y. Okinaka and M. Hoshino, "Some recent topics in gold plating for electronics applications," *Gold Bulletin,* vol. 31, no. 1, pp. 3-13, 1998, doi: https://doi.org/10.1007/BF03215469.

[105] A. Casagrande, G. Cammarota, and L. Micele, "Relationship between fatigue limit and Vickers hardness in steels," *Materials Science and Engineering: A,* vol. 528, no. 9, pp. 3468-3473, 2011, doi: https://doi.org/10.1016/j.msea.2011.01.040.

[106] J. Hyvönen, A. Meriläinen, A. Salmi, L. Hupa, N. Lindfors, and E. Hæggström, "Three Megapixel Ultrasonic Microscope Imaging," in *2019*

*IEEE International Ultrasonics Symposium (IUS)*, 2019: IEEE, pp. 1886-1889, doi: https://doi.org/10.1109/ULTSYM.2019.8925785.

[107] M. Schulz, J. Brandt, K. Raum, and K. Brehme, "Quantitative Assessment of Bone Properties during Defect Healing in an Animal Defect Model by Scanning Acoustic Microscopy," in *World Congress on Medical Physics and Biomedical Engineering, September 7-12, 2009, Munich, Germany*, 2009: Springer, pp. 289-292, doi: https://doi.org/10.1007/978-3-642-03900-3_84.

[108] I. Leguerney *et al.*, "Trabecular bone properties evaluated by scanning acoustic microscopy," *Proceedings WCU,* pp. 295-298, 2003.

# Appendix 1. Cavitation threshold calculation

To calculate cavitation thresholds for five select frequencies, a modified version of the equation found in [36] was used. The original equation in [36] takes into account surface tension, viscosity, and inertia and its derivation is not repeated here. A modification was made by calculating the maximum temperature reached inside the bubble, instead of using an assumption, as in the original article.

The equation in [36]describing the acoustic cavitation threshold is:

$$f = \frac{\left(\frac{1}{3\pi R_0}\sqrt{\frac{P_0\xi}{\rho}}\left(\sqrt{\frac{p^*-1}{p^*}}+\sqrt{\frac{p^*-p_b^*}{p^*}}\right)\right)}{\left(\frac{T_{max}}{T_0(\gamma-1)\left(\frac{\xi}{3}+1\right)}\right)^{1/3}-0.46+\frac{4\mu}{R_0}\sqrt{\frac{2}{\rho P_0\xi}}+\frac{2\sigma}{P_0R_0}\sqrt{\frac{\xi}{3}}\left(\frac{1}{p^*-p_b^*}\right)^{3/2}} \tag{A1}$$

where $p^*$ is the normalized acoustic amplitude $p^* = P_A/P_0$, and $p_b^*$ is the normalized Blake threshold:

$$p_b^* = \frac{P_{Blake}}{P_0} = 1 + \frac{4}{9}X_B\sqrt{\frac{3X_B}{4(1+X_B)}} \tag{A2}$$

with $X_B = 2\sigma/(R_0P_0)$.

The parameter $\xi$ is:

$$\xi = p^* + p_b^* - 2 + \sqrt{(p^*-1)(p^*-p_b^*)} \tag{A3}$$

The maximum collapse temperature inside the bubble was assumed to be 5000 K in [36]. Assuming that the collapse is adiabatic, it can be calculated as [37]:

$$T_{max} \sim \left(\frac{(P_0+P_A)(\gamma-1)}{P_0}\right)T_0 \tag{A4}$$

Equation A1 can be solved numerically using Newton’s method, which was implemented in Matlab.

Newton’s method is a root-finding method for a real-valued differentiable function, $g(x)$. An improved estimate of the root, $x_{n+1}$, is calculated from the x-intercept of the tangent to the function at a guessed root, $x_n$. The new root is thus calculated as:

$$x_{n+1} = x_n - \frac{g(x_n)}{g'(x_n)} \tag{A5}$$

The function $g(x)$ in this case was:

$$g(p^*) = \frac{\left(\frac{1}{3\pi R_0}\sqrt{\frac{P_0\xi}{\rho}}\left(\sqrt{\frac{p^*-1}{p^*}}+\sqrt{\frac{p^*-p_b^*}{p^*}}\right)\right)}{\left(\frac{T_{max}}{T_0(\gamma-1)\left(\frac{\xi}{3}+1\right)}\right)^{1/3} - 0.46 + \frac{4\mu}{R_0}\sqrt{\frac{2}{\rho P_0\xi}} + \frac{2\sigma}{P_0R_0}\sqrt{\frac{\xi}{3}}\left(\frac{1}{p^*-p_b^*}\right)^{3/2}} - f \tag{A6}$$

The process is repeated until a selected tolerance is reached. The selected tolerance was $|x_{n+1} - 0| < 10^{-9}$.

The parameters used for the calculations were: $P_0$ = 101.325 kPa, $\rho$ = 1000 kg/m3, $\sigma$ = 0.072 N/m, $\mu$ = 0.001 Pa·s, $\gamma$ = 1.4, and $T_0$ = 300 K.

Equation A1 was solved for frequencies $f$ = [11.8 MHz, 7.3 MHz, 4.2 MHz, 1 MHz, 20 kHz] and initial bubble radii $R_0$ from 0.01 µm to 2 µm in steps of 0.02 µm.

The same parameters were used to calculate resonance frequencies according to Minnaert’s equation (Equation 4). The resonance sizes for 1 MHz and 20 kHz were outside the selected of range of $R_0$, at 3.3 µm and 164.2 µm, respectively.

Ultrasonics Sonochemistry 111 (2024) 107109

Contents lists available at ScienceDirect

Ultrasonics Sonochemistry

journal homepage: www.elsevier.com/locate/ultson

# Gold removal from e-waste using high-intensity focused ultrasound

Axi Holmström [a,*], Topi Pudas [a], Jere Hyvönen [a], Martin Weber [a], Kenichiro Mizohata [b], Tom Sillanpää [a,c], Joni Mäkinen [a], Antti Kuronen [b], Tapio Kotiaho [c,d], Edward Hæggström [a], Ari Salmi [a]

[a] Electronics Research Laboratory, Faculty of Science, University of Helsinki, P.O.B. 64, FIN-00014 University of Helsinki, Finland
[b] Accelerator Laboratory, Faculty of Science, University of Helsinki, P.O.B. 43, FIN-00014 University of Helsinki, Finland
[c] Drug Research Program and Division of Pharmaceutical Chemistry and Technology, Faculty of Pharmacy, University of Helsinki, P.O.B. 56, FIN-00014 University of Helsinki, Finland
[d] Department of Chemistry, Faculty of Science, University of Helsinki, P.O.B 55, FIN-00014 University of Helsinki, Finland

ARTICLE INFO

*Keywords:*
E-waste recycling
Urban mining
High-intensity focused ultrasound
Cavitation
Cavitation erosion
UN SDG 12

ABSTRACT

The demand for rare and precious metals (RPMs), e.g. gold, is increasing, as these are used in the ever-increasing amount of electronics needed for technological development and digitalization. Due to their rarity, virgin mining of RPMs is becoming more difficult and expensive. At the same time, over 62 Mt of e-waste is created globally each year. The high concentration of gold and other RPMs in e-waste makes it an excellent source for recycling. Unfortunately, current recycling methods need to separate the different metals and the current pyrometallurgical and hydrometallurgical processes also create toxic pollutants, large amounts of wastewater and require highly corrosive substances. Here we present a new method for gold removal for the purpose of recycling, using only water and high-intensity focused ultrasound to induce material erosion through cavitation. An 11.8 MHz ultrasonic transducer is used to first image the sample to locate gold-coated pads on discarded printed circuit boards (PCBs) and subsequently to remove only the gold layer. We demonstrate that the gold removal can be controlled by the number of transmitted ultrasonic bursts and that the energy efficiency is optimal when only minute amounts of the nickel layer beneath are also removed. Removing solely the gold layer also decreases the need for further processing steps. This greener gold removal method for e-waste is therefore well aligned with, and contributing to, the United Nations Sustainable Development Goal 12: Ensure sustainable consumption and production patterns.

## 1. Introduction

Due to increasing technological development and digitalization, the demand for electronic devices is increasing. Electronics are built on printed circuit boards (PCBs), which contain rare and precious metals (RPMs), such as gold, silver, and platinum, as well as copper and nickel [1]. RPMs are not easily substituted for more available materials, as they have certain properties required for PCBs, such as high electrical conductivity and corrosion resistance. As the amount of electronics increases, so too does the amount of e-waste. Currently, over 62 Mt of e-waste is generated globally per year, of which only 14 Mt is recycled [2]. The amount of generated e-waste is expected to increase to 82 Mt per annum by 2030 [2]. E-waste recycling is already more profitable than virgin mining [3] and despite the low mass fraction of gold in e.g. PCBs (only 0.11 ‰), gold constitutes 66 % of the monetary worth [4].

In 2019, 4 831 t of gold was produced, with only 1 297 t coming from recycled sources [5]. With 55 000 t of unmined gold reserves and a current global annual mining rate of approx. 3 500 t, mineable gold reserves would run out in 15 years [5]. It is therefore necessary to increase gold recycling from e-waste. As gold (and other RPMs) is already concentrated in PCBs, they constitute an excellent source for recycling: There is approximately the same amount of gold in 1 t of e-waste as in 17 t of mineable ore [6]. Decreasing virgin mining and increasing recycling is therefore a key aspect of the United Nations Sustainable Development Goal (UN SDG) 12: Ensure sustainable consumption and production patterns, particularly Target 12.2: By 2030, achieve the sustainable management and efficient use of natural resources, and 12.5: By 2030, substantially reduce waste generation through prevention,

---

* Corresponding author.
*E-mail address:* axi.holmstrom@helsinki.fi (A. Holmström).

https://doi.org/10.1016/j.ultsonch.2024.107109
Received 22 August 2024; Received in revised form 10 October 2024; Accepted 14 October 2024

reduction, recycling and reuse [7,8].

Recycling e-waste is already being done, usually through pyrometallurgy and/or hydrometallurgy [1,4,9]. Such methods are needed, as waste PCBs contain several materials that need to be separated in different steps: plastic and other non-metallic substances are burnt off and all metals, e.g. copper, nickel, and gold, need to be separated. However, these methods have significant drawbacks: The burning of e-waste creates toxic and volatile air pollutants and large amounts of $CO_2$ [1,10], and hydrometallurgy usually employs toxic and/or highly corrosive substances for leaching (e.g. *aqua regia*, piranha solution ($H_2SO_4$/$H_2O_2$) and cyanide [10]), which are difficult to handle and create large amounts of wastewater [1,10]. There are developments being made using biological substances, e.g. bioleaching [1,11] and deep eutectic solvents [10,12], that could provide greener solutions. However, these are still in the early development phase and are slow [11,12]. The microorganisms are selective, i.e., one population only recovers one substance [11]. Furthermore, the microorganisms can perish due to the generated toxic substances, thus stopping the process [11]. Deep eutectic solvents again have high viscosity, which requires use at higher temperatures than inorganic acids and long leaching times [12], and some are not genuinely green, as their synthesis requires toxic components that are not easily biodegraded [12]. Thus, there is still a great need for improved and cleaner gold recycling methods.

In this paper, we present a novel high-intensity focused ultrasound (HIFU) technique to remove gold from PCBs, using only HIFU in water, requiring no additional chemicals. Breaking materials with HIFU-induced inertial cavitation has already been established in the medical fields of histo- and lithotripsy [13–16]. Cavitation erosion on metals has also been studied [17–26], but it has yet to become widely used for controlled material removal of metals. A recent study showed that cavitation activity could be utilized in a deep eutectic solvent to improve RPM recycling from e-waste [24]. However, the 20 kHz sonotrode in that study removed all metal layers of the PCB (containing gold, nickel, and copper) at once, requiring further separation steps. Watt *et al.* demonstrated removing gold nanoparticles and only minor amounts of nickel from a SIM card in a two-surfactant system, also by using a 20 kHz sonotrode [26]. While they managed to restrict the erosion depth to the layers of interest, the use of a sonotrode on a generic PCB sample is not sufficiently selective. While the surface of a SIM card consists almost exclusively of gold, generic gold pads on e.g. PCBs are much narrower than the tip of a sonotrode (tips in both [24,26] were 6.4 mm). Thus, the adjacent substrate would also be removed, again requiring additional separation steps. In our approach, we use a high-frequency (11.8 MHz) HIFU transducer, which is first used to image a PCB sample to localize gold pads. Then the same transducer is driven at high power to cause cavitation-induced metal erosion from only desired areas, thereby removing the top gold layer (and only minute amounts of nickel from the layer beneath). Here we show how the gold and nickel removal depends on the number of transmitted ultrasonic bursts. This method requires only water (no added chemicals) and decreases the need for further processing steps by predominantly removing only gold. It could therefore contribute to greener and improved e-waste recycling methods and to the UN SDG 12. Table 1 summarizes some examples of research advancing HIFU-induced gold removal for recycling purposes, which have contributed towards the SDGs.

## 2. Methods

### 2.1. Setup and samples

A schematic of the setup used in this work is shown in Fig. 1. The setup is an improved version of the ones described in [28–31] (gold removal proof-of-concept conference paper [28], aluminium erosion [30,31], soft material removal [29]). The same transducer was used for both imaging (locating gold pads) and material erosion. It was custom-built using a commercial curved piezo bowl (type Pz26, model F5260195, CTS Ferroperm, Denmark), with epoxy backing in a 3D printed housing. The transducer had a central frequency of 11.8 MHz, bandwidth of 1.2 MHz, element diameter 1.9 cm, focal distance 1.5 cm and focal width 140 µm. All sonications were performed in an open container with purified water (RiOs Essential Water Purification Systems, Merck KGaA, Germany) that had been vacuumed (Laboport UN 810.3 FTP, KNF Neuberger GmbH, Germany) for 30 min prior to the start of experiments. This was done to obtain similar conditions for

**Table 1**
Examples of some research that have advanced SDGs and HIFU-induced gold removal for recycling purposes.

| The focus of the study/ studies | Key points | SDGs and targets | Countries of affiliation (authors) | Reference |
|---|---|---|---|---|
| Histo- and lithotripsy using HIFU for biomedical applications | • Utilizing HIFU to non-invasively liquefy tissue or erode kidney stones | SDG-3: Ensure healthy lives and promote well-being for all at all ages. Target 3.8 | Numerous groups world-wide | Review of various preclinical applications in both thermal and non-thermal regime [15]. |
| Industry standard for conducting acoustic cavitation erosion tests | • Using 20 kHz sonotrode to induce cavitation erosion on e.g. metal (particularly Note 1 pertaining to “stationary specimen” tests)<br>• Repeatable method to evaluate cavitation resistance in e.g. pumps, hydraulic turbines, valves, propellers etc. | SDG-9: Build resilient infrastructure, promote inclusive and sustainable industrialization and foster innovation. Target 9.1, 9.4 | United States | [27], originally approved in 1972, latest ed. 2021. |
| Extracting gold nanoparticles from e-waste | • Reduce hazardous waste and energy requirements for gold nanoparticle synthesis by using a 20 kHz sonotrode<br>• Extract the nanoparticles from e-waste (SIM card) | SDG-12: Ensure sustainable consumption and production patterns. Targets 12.2, 12.5 | United States | [26] |
| Improved PCB recycling in deep eutectic solvent by low-power ultrasound | • Combining 20 kHz sonotrode with deep eutectic solvent for gold, nickel and copper recycling<br>• Processing time for gold, nickel and copper removal improved thirtyfold | SDG-12: Ensure sustainable consumption and production patterns. Targets 12.2, 12.5 | United Kingdom | [24] |
| Gold removal from e-waste using HIFU | • Proof-of-concept to demonstrate gold removal from PCBs using MHz HIFU<br>• Ability to image and locate gold pads on a PCB and produce three deep erosion holes<br>• Done in water immersion without added chemicals | SDG-12: Ensure sustainable consumption and production patterns. Targets 12.2, 12.5 | Finland | [28] (conference paper), precursor to the study presented in this paper. |

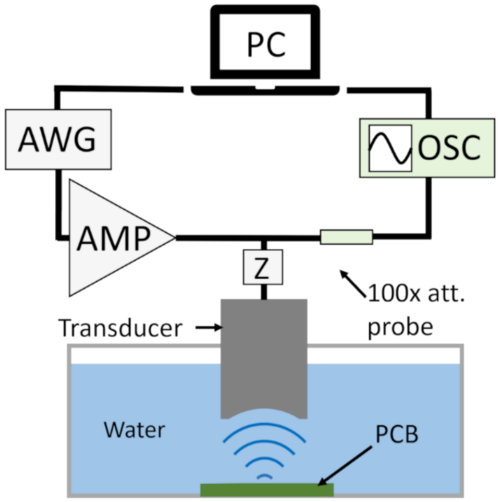

**Fig. 1.** Setup. A PC controlled a three-axis translation stage and the arbitrary waveform generator (AWG), which transmitted excitation signals to the 11.8 MHz custom-built focused transducer. A power amplifier (AMP) was used for erosion experiments and impedance matching (Z) ensured maximum power transfer. In imaging and when positioning the transducer, the echoes reflected from the printed circuit board (PCB) were received with an oscilloscope (OSC) and recorded on the PC. A 100x attenuating probe was used to protect the oscilloscope from the transmitted high-amplitude ($U_{PP}$ = 398 V) signals in the erosion experiments.

bubble nucleation in all cavitation experiments, as both particulates and dissolved gas content influence the cavitation probability.

A motorized three-axis translation stage (NLS4 NEMA 17 MDrive, Newmark Systems Inc., USA) was used to move the transducer. Transmission, signal acquisition, and the translation stage were all controlled by a custom-written Python script (Python 3). On the transmission side, an arbitrary waveform generator (AFG31052 SERIES, Tektronix, USA) was used to generate the desired signals, which were amplified with a Class A RF power amplifier (500A100A, Amplifier Research, USA). During imaging, minimum amplification was used (0 % RF gain), whereas during erosion experiments, maximum settings were used (100 % RF gain). At maximum amplification, the peak-to-peak voltage of the electric signal driving the transducer was $U_{PP}$ = 398 V (example signal shown in Supplementary material Fig. S1a). The transducer was matched to 50 Ω (at the driving frequency) with an LC impedance matching circuit to ensure maximum power transfer from the 50 Ω output of the amplifier to the transducer. During imaging, the echoes reflected from the sample were recorded with a digital oscilloscope (Picoscope 5442D, Pico Technology, UK) and saved on the PC. A 100x attenuating probe (TT-HV250, TESTEC Elektronik GmbH, Germany) was used to protect the oscilloscope from the transmitted high-amplitude signals in the erosion experiments. Echoes were also displayed in real time during erosion experiments for cavitation monitoring.

To determine the acoustic pressure at the focus, an optical hydrophone (ONDA HFO-690, Ø = 100 µm, Onda Corporation, USA) was used to measure the pressure directly at the focus of the transducer. Due to the high pressure amplitudes involved, cavitation started after only three rarefactive cycles (four compressive), which was repeatable over all 15 recorded signals (see Supplementary materials S1 and Fig. S1b for details). However, at the third peaks (both positive and negative), the electric signal was almost equal to the stable oscillation values and thus the peak-positive and peak-negative-pressures, $P_{PPP}$ and $P_{PNP}$, could be estimated. When the pressure values were calculated, the Small Signal Sensitivity $SSS$ = 5.57 mV/MPa provided by the device was used with a frequency-dependent tip scattering correction, $k = 0.459$, calculated for 11.8 MHz. The corrected pressure was calculated as $P_{\text{corrected}} = k \cdot P_{SSS}$, where $P_{SSS}$ was the pressure obtained using only the $SSS$ (for details, see Supplementary materials S1). Thus, the peak-positive and peak-negative pressures (marked with green asterisks in Fig. S1b) were obtained: $P_{PPP} = (46 \pm 1)$ MPa and $P_{PNP} = (-35 \pm 5)$ MPa (mean ± 1 SD), with standard deviations calculated from the 15 signals.

The PCB sample (Fig. 2a), containing several gold pads, was cut from a discarded motherboard. The gold layer thickness of the pads was measured with Rutherford backscattering spectrometry using a 3 MeV proton beam from 5 MeV tandem accelerator at the University of Helsinki (incident angle $\alpha = 30^\circ$). Scattered probing particles were detected using an Ortec Ultra ion-implanted silicon detector (scattering angle $\theta = 165^\circ$, detector-sample distance 80 mm, 50 mm$^2$ detector surface area, limiting detector solid angle to 8 msr). The gold layer thickness was measured to be (1.73 ± 0.04) µm.

### 2.2. Identifying regions-of-interest

The PCB was imaged prior to each erosion experiment to determine the locations of the gold pads. Imaging was performed with the same 11.8 MHz transducer that was used for erosion. Imaging parameters were $f$ = 11.8 MHz, 10 cycles per burst, step size 100 µm. An example photograph and an ultrasonic image of the sample are shown in Fig. 2a and b, respectively. The gold pads are clearly visible and distinguishable from the adjacent substrate. In addition, erosion holes from prior experiments can also be seen in both images. Even with the 11.8 MHz transducer, all but the smallest erosion holes are discernible and pristine pads thus easily identified.

### 2.3. Gold removal

#### 2.3.1. Sonication parameters

Two sets of experiments were performed relating to gold removal: 1) Defocus sweep to determine the optimal transducer-sample distance, and 2) a burst sweep to evaluate gold removal. Preliminary experiments revealed that material erosion was dependent on the transducer-sample distance, hence the defocus sweep was performed. In the defocus sweep, the constant sonication parameters, used at each sonication spot, were: $f$ = 11.8 MHz, maximum amplitude ($U_{PP}$ = 398 V, $P_{PPP}$ = 46 MPa, $P_{PNP}$ = − 35 MPa), 50 cycles per burst, 500 000 bursts per sonication spot, pulse

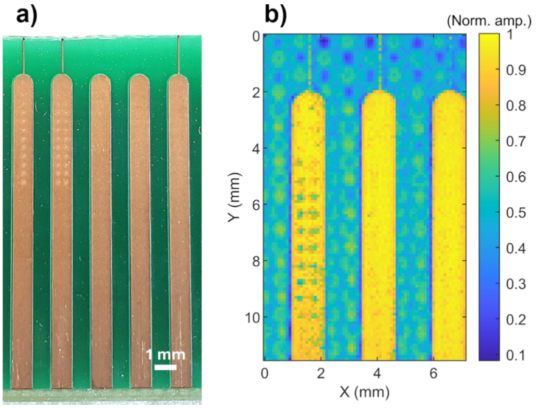

**Fig. 2.** Locating gold pads. a) Example photograph of the PCB and b) image taken with the 11.8 MHz transducer. Erosion holes from prior experiments can also be seen in both images.

repetition frequency (PRF) 500 Hz. Three repetitions were made with 13 defocus distances in 100 µm steps, from defocus − 500 µm (focus inside the sample) to +700 µm (focus on top of the sample), with defocus 0 µm signifying focusing on the sample surface.

Having determined the optimal defocus distance (+150 µm, see 3. Results), the burst sweep was performed. The purpose was to determine how gold removal depends on input energy. Only the number of bursts sonicated in one spot was varied, the other sonication parameters were constant: $f = 11.8$ MHz, maximum amplitude ($U_{PP} = 398$ V, $P_{PPP} = 46$ MPa, $P_{PNP} = -35$ MPa), 50 cycles per burst, PRF 500 Hz, defocus distance +150 µm. Three repetitions were performed with (50, 100, 150, 200, 250, 300, 350, 400, 450, 500, 600, 700) × 1000 bursts per spot. Cavitation activity, which was monitored from the echoes, did not cease during sonications.

### 2.3.2. *Quantifying erosion areas, volumes, and mass*

All erosion holes were measured with a coded-excitation scanning acoustic microscope (CESAM) [28,32,33]. Produced topography maps enabled calculating both the area of the erosion holes (which were also visible in optical images, Fig. 3a), and their depth, and hence volume, as well. The CESAM images were obtained with a 375 MHz transducer (bandwidth 140 MHz, beam width 2.5 µm, depth-of-focus 29 µm, scanning step size 2 µm) using a 300–500 MHz linear frequency modulated chirp of 1 µs length with a Gaussian envelope. Examples of an optical image and corresponding amplitude and topography maps taken with CESAM are shown in Fig. 3. The surface roughening is seen in both the optical and CESAM amplitude images, whereas the deep erosion holes, where the nickel beneath the gold pad is exposed in the optical image, are readily visible in the CESAM topography map. Thus, the CESAM topography maps were used to analyze eroded areas and volumes of the deep erosion holes.

All analyses were done with Matlab R2020b (The MathWorks, Inc., USA). As the gold pads are not entirely flat (up to 5 µm surface height variation within one pad, an example pad is shown in Supplementary material Fig. S2), each erosion hole was first processed manually to determine the correct zero level of the surface. Next, the areas of the deep erosion holes (visible in the topography map) were determined by manually creating a mask of the hole using Matlab's "drawassisted" function. The area was then calculated from the mask and the erosion hole volume was calculated from the topography inside the mask. The volume of removed gold was subsequently calculated from the erosion hole topography using the measured gold layer depth $d_{Au} = (1.73 \pm 0.04)$ µm to determine when gold had been removed and when the erosion had reached the nickel beneath. The mass of removed gold was then calculated from the eroded gold volume using the density of gold, $\rho_{Au} = 19.32$ g/cm$^3$ [34]. Gold removal efficiency was also calculated as the ratio of removed gold mass to used electrical energy (and normalized to the maximum mean value). The electrical energy delivered to the transducer was 1.7 mJ per burst, as determined from the measured voltage signals (for details, see Supplementary materials S3).

## 3. Results

### 3.1. *Transducer-sample distance*

First, the optimal transducer-sample distance for gold erosion was determined from the defocus sweep. The results from all three sweeps and their mean ± 1 SD are shown in Fig. 4a. The largest eroded areas were achieved with between 0 µm and +300 µm defocus (0 µm signifying focusing on the surface, positive moving the focus above the surface). In this region, the widths of the erosion holes approach the width of the focal main lobe (140 µm), and only few stochastically generated separate minor pits outside the large erosion areas are present. A CESAM image of one hole produced with +100 µm defocus is shown as an example in Fig. 4b. Based on these results, a defocus of +150 µm was used in subsequent erosion experiments.

### 3.2. *Gold removal*

Having determined the optimal defocus distance (selected as +150 µm), the main study, i.e. gold removal as a function of sonicated bursts, was performed. As expected, the erosion area increased with number of bursts, as more bursts enables more cavitation events and thus erosion (Fig. 5a). The total eroded volume (total volume of each erosion hole, including gold and nickel) was calculated using the depth information obtained with the CESAM (Fig. 5b).

The volume of removed gold was subsequently calculated (Fig. 6a). With an increasing number of bursts, more gold was removed, though a slight plateauing effect is seen. This effect occurs because the region of highest cavitation activity (highest pressures in the focus) erodes through the (1.73 ± 0.04) µm gold layer and starts eroding the nickel beneath. The gold erosion does not halt completely, as the weaker

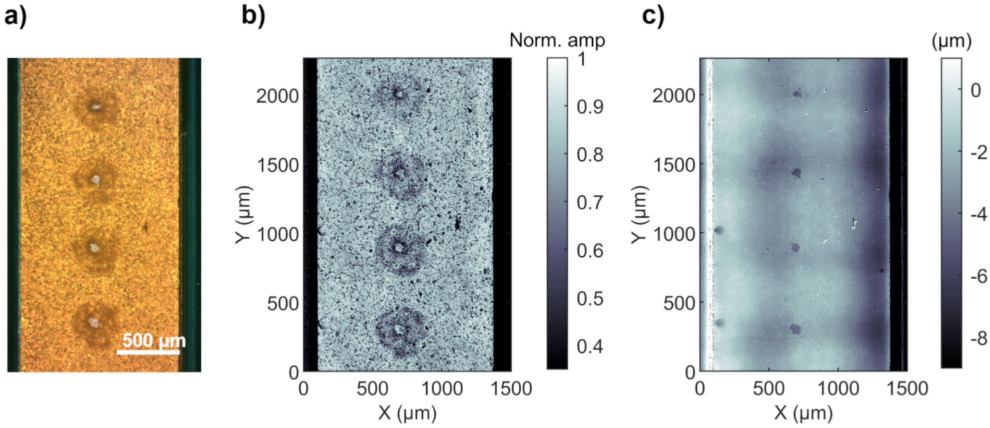

**Fig. 3.** Examples of a) optical microscope image, b) CESAM amplitude map, and c) CESAM topography map of four corresponding holes from one burst sweep. The surface roughening around the deep holes is visible in both the optical image and amplitude map (a, b). The small deep holes, where gold has been removed and the nickel beneath is exposed, are readily visible in the optical image (a) and the topography map (c). Erosion areas and volumes were subsequently determined from the topography maps.

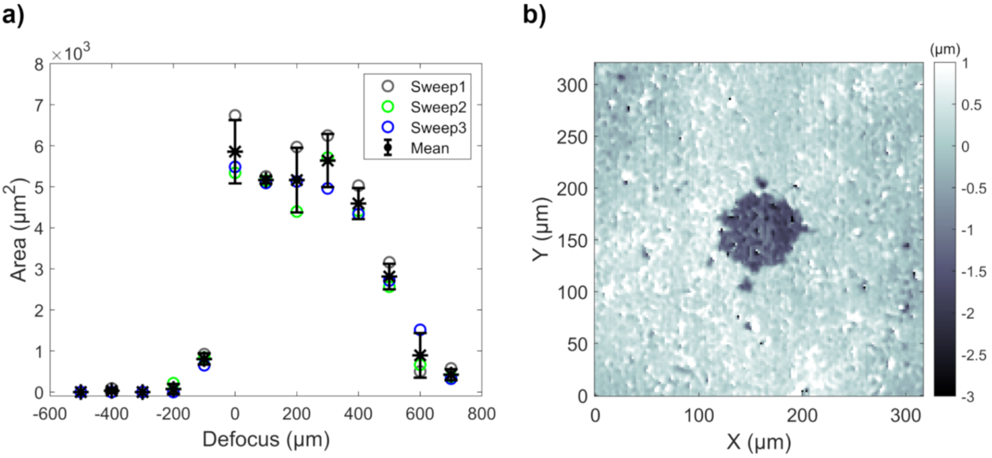

**Fig. 4.** Defocus sweep to determine optimal transducer-sample distance. a) Erosion area as a function of defocus distance. Sweep numbers signify measurement series and the mean ± 1 SD is shown. Defocus 0 μm is focused at the surface, negative defocus below and positive defocus above the surface. The largest eroded areas are achieved with defocus between 0 and +300 μm. b) Example of topography map of a hole at +100 μm defocus. The width of the hole is slightly less than the 140 μm focal beam width. Only a few stochastic cavitation events (smaller pits) are visible outside the main lobe.

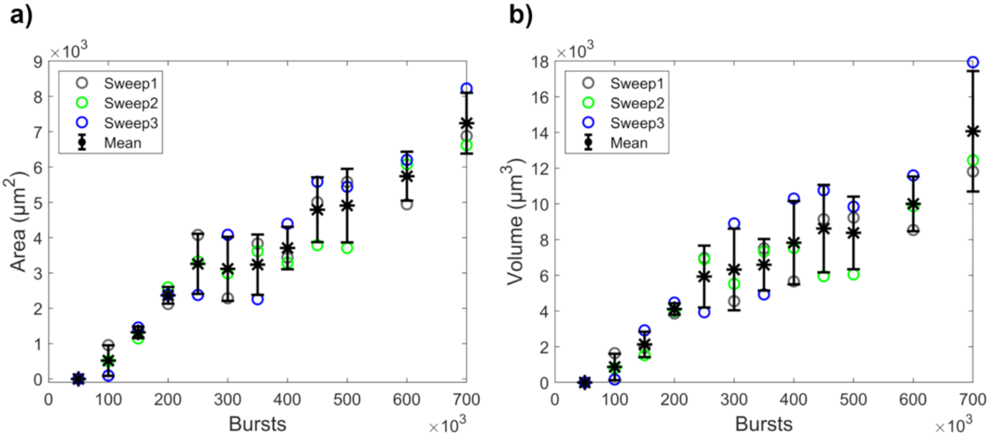

**Fig. 5.** Material removal as a function of number of sonicated bursts. a) Area and b) volume of deep erosion holes. Sweep numbers signify measurement series and the mean ± 1 SD is shown.

cavitation activity in the outer region of the focus continues to remove gold. For gold recycling purposes, it would be desirable to only remove the gold, without removing nickel. Nickel starts to be removed at approx. 250 000 bursts (Fig. 6b). Thus, sonicating fewer bursts in one spot and then moving the transducer could be preferable to sonicating many bursts in one spot. One can also conclude that while cavitation is a stochastic phenomenon, at these high burst counts, the gold removal is quite repeatable.

Finally, the mass of the removed gold was calculated (Fig. 7a). Despite the small masses removed from each hole, erosion was achieved through the depth of the gold layer. The removed gold mass was also compared to the electrical energy used (Fig. 7b), which showed that the removal efficiency starts to decrease after 250 000 bursts, when nickel is also removed. Therefore, even though gold continues to be removed with more bursts, but at a slower rate (outside the main focal volume), the removal efficiency decreases as more electric energy is wasted on removing nickel instead of gold inside the main focal volume.

## 4. Discussion

As technological development and digitalization continues on a global scale, the need for PCBs, and subsequently RPMs (e.g. gold), will continue to increase. As current e-waste recycling methods still have significant drawbacks (creation of toxins, wastewater, use of strong acids, etc. [1,10]), new, more environmentally and user-friendly recycling methods could greatly contribute to the UN SDG 12 (Ensure sustainable consumption and production patterns), particularly Targets 12.2 and 12.5 [7,8]. The HIFU method presented in this paper — using only ultrasound in water, with no added chemicals — could be a step towards such a solution.

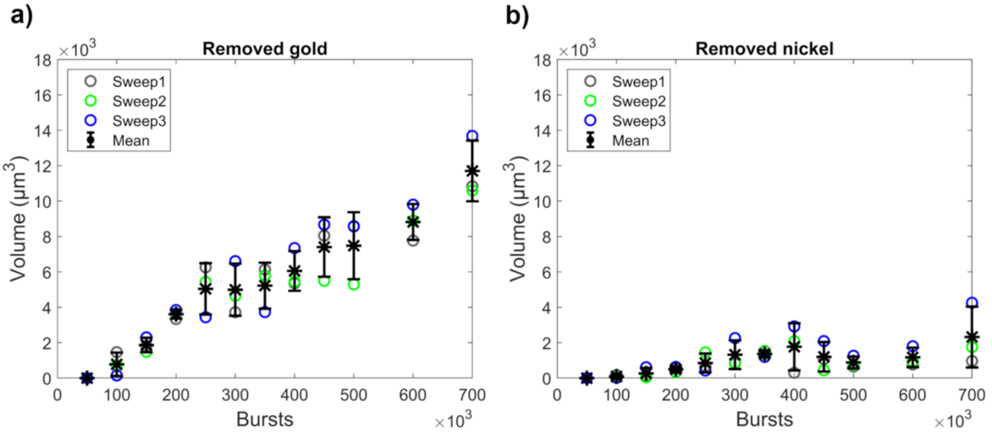

**Fig. 6.** Volumes of removed a) gold and b) nickel as a function of number of bursts. Sweep numbers signify measurement series and the mean ± 1 SD is shown. Gold removal plateaus slightly as the erosion continues into the nickel layer beneath. Gold removal still continues, as the weaker cavitation activity in the outer region of the focus continues to remove gold.

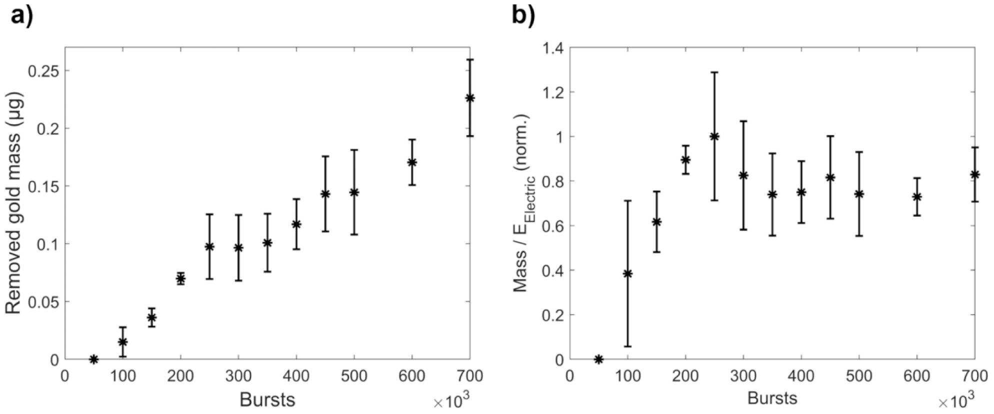

**Fig. 7.** Mass of removed gold and removal efficiency as a function of bursts. Mean ± 1 SD from the three sweeps in Figs. 5 & 6a are shown. **a)** Mass of removed gold. **b)** Removal efficiency: The ratio of removed gold mass to used electrical energy. For readability, the values have been normalized by the maximum mean value (at 250 000 bursts). Beyond 250 000 bursts, the efficiency decreases as nickel is also removed.

### *4.1. Benefits of HIFU*

Whereas HIFU-induced cavitation is common in medicine, applications for metal erosion are scarce. While cavitation damage to metals has been long known [35,36], previous work on controlled cavitation-induced metal erosion has mainly focused on studying laser-generated single-bubble erosion dynamics [18,20,22,25,37,38] or the effect of non-localized ultrasound [26] and adding it to existing methods [24]. Here we showed that high-frequency HIFU (11.8 MHz) can be used to locally erode gold and that the amount of removed material can be controlled by the number of sonicated bursts. Our previous proof-of-concept work on HIFU gold removal demonstrated three erosion holes created with identical acoustic parameters, without studying the controllability of the erosion [28]. Here we showed the gold erosion's dependence on easily controlled parameters, i.e., defocus and number of bursts. Our tightly focused transducer (focal width 140 µm) also enabled ultrasonic imaging to locate the gold pads prior to erosion, thus facilitating gold removal from only the desired area, i.e. the gold pads, and not the surrounding substrate. While sonotrodes have many advantages (e.g. that they are built for high amplitude and long sonication times), they lack the selectivity of HIFU. This selectivity is an important aspect, because the need for pyrometallurgical and hydrometallurgical techniques in current e-waste recycling processes stems from the presence of undesired materials (e.g. plastics) and other metals present in PCBs (e.g. copper and nickel). Removing only gold (and possibly minute amounts of nickel) therefore decreases the need for hazardous post processing.

### *4.2. Gold removal and cavitation*

The presented burst sweep results show that the amount of removed gold initially increases linearly, but shows a slight plateauing effect when nickel starts to be removed. This was expected, as more bursts translates to more cavitation events. Gold removal did not stop completely, even when nickel was also removed. The cavitation probability is not constant in the entire focus, but pressure dependent, and hence the number of cavitation events decreases towards the outer edges of the focus, even within the main lobe. This outer region continued to erode gold with the highest burst counts. Bubble cloud dynamics are the cause of the optimal defocus distance – when focusing some distance above the surface, the created bubble cloud with its subsequent internal dynamics caused by cavitation events (shock waves and microjets) create suitable conditions for gold erosion. While the effect of the stand-off distance of single bubbles on erosion has been studied [18,20,22,25,37], our case is not that of a single bubble, but a cloud, and hence such results are not directly transferrable. In this work, we empirically determined a repeatable optimal defocus region for use in our gold removal application. High-resolution high-speed camera footage and analyses similar to [39] could provide insight into the bubble cloud dynamics and why the optimal defocus is between 0 μm and +300 μm.

Only the effect of defocus and burst count was investigated in this study, even though other parameters affect cavitation erosion too: frequency, pressure amplitude, number of cycles, PRF, dissolved gas in the liquid, etc. We used a high-frequency (11.8 MHz) focused transducer to ensure small spot size (much smaller than the gold pad, to ensure selectivity) and high energy density at the focus, even though the cavitation threshold increases with frequency [40–42]. Higher amplitudes might decrease the number of required bursts, as each burst could generate more powerful microjets and inertial bubble collapses. An amplitude study was excluded since even using the highest driving voltages generated by our commercial amplifier, several hundred thousand bursts were still required. The number of cycles also affects the erosion, as long bursts might cause bubble shielding [43], which could reduce erosion. As we could not monitor the cavitation cloud dynamics during the bursts, the effect of the burst length in our case remains undetermined. The transducer took ~ 20 cycles to settle into stable oscillation, so 50 cycles/burst was selected, which also demonstrated effective gold removal in preliminary experiments. The water was always degassed for 30 min prior to sonications, but as the sonication experiments took 2–4 h to perform, the gas content did not remain constant during the experiments. This could explain some variability in the results. The main reason for the long sonication times was the low PRF (500 Hz), which was chosen to ensure sufficient heat dissipation from the transducer. Higher PRFs with these high amplitudes caused our thin curved piezos to overheat and break.

Inertial cavitation is affected by many parameters, which gives it a quasi-stochastic nature. Thus, the variability between repeated experiments introduces the greatest uncertainty in the results. By manually performing the erosion area selection, uncertainties in area were at the level of some *per mille*. Even the uncertainty in the gold-layer depth measurement only caused 1–2 % uncertainty in the volume estimates. Thus, these are minute compared to the variability shown between repeated measurements.

Compared to our previous studies on cavitation erosion on aluminium [30,31], gold is surprisingly difficult to erode. Aluminium can be eroded using only a few percent of the number of bursts required for gold (setup in [30,31] was comparable to [28]). One hypothesis is that since gold is more malleable (less brittle) than aluminium, the erosion therefore becomes a fatigue process [44]. The high number of required bursts could support this. It is also possible that the layered structure of the PCB pads plays a role in the fracture mechanics of the top layer (gold). As gold is a noble metal, it might also be resistant to any contributing effect from free radicals that form in the water during inertial cavitation [45]. Molecular dynamics simulations could provide valuable insight into the cavitation erosion dynamics of different solid materials. In the presented method, gold erosion could be accelerated by introducing abrasive particles to the water. Other methods for improving the erosion could be to decrease frequency while maintaining a sufficiently tight focus (to reduce the frequency-dependent cavitation threshold, but reaching high energy densities) and to use larger piezo disks to generate higher power.

### 4.3. *Outlook and scale-up*

In this study, we focused on the HIFU gold erosion and excluded the subsequent gold collection. While developing the gold collection is important for any future use of this technology, the novelty lies in using HIFU for selective gold removal. Collecting the removed gold was left for future work. There are several common methods for collecting small particulates from aqueous solutions, e.g. filtering, sedimentation, evaporation, and centrifugation. More complex methods for gold particle collection also exist, e.g. nylon-based 3D-printed scavengers [46], amyloid nanofibril aerogels [47], and metal–organic frameworks (e.g. [48]). Localized sampling during the sonication process [29] could also be combined with any of the aforementioned methods to reduce the volume from which to collect the gold. As gold was not collected, the purity and size of the removed gold particles is not known, which will also be studied in the future. If the gold would be removed as nanoparticles, as in [26], it would open up even more possible new end-uses for the removed gold.

This method's greatest advantage is the use of only ultrasound and water, with no added chemicals, and that it allows to remove gold from accurately predefined areas of e.g. a PCB. Despite the amounts of removed gold now being small, the technology could be optimized and scaled up by using several transducers in parallel. Optimization could be done by e.g. tuning the used frequency (lower frequencies have lower cavitation thresholds) and the focusing of the used transducer. A lower-frequency transducer with the same focusing (numerical aperture) has a larger focal width. Thus, it could plausibly remove gold from a larger area in the same amount of time. Considering the added beneficial effect of a lower cavitation threshold, gold removal might be increased further. When decreasing frequency, care must be taken to ensure both sufficient energy densities at the focus and a small enough spot size to maintain selectivity. This could be done with a more tightly focused transducer. After appropriate single-transducer optimization, many transducers could be used simultaneously to scale up the technology. These could be placed in parallel (in suitable places for sonicating different PCBs simultaneously) or combined into an array to achieve much higher acoustic intensities.

A rough estimate of the profitability, i.e., the monetary worth of the removed mass of gold divided by the cost of electricity used, was > 1 for all cases where any gold was removed, even when considering a 40–60 % efficiency of the power amplifier. With further optimization and scaling, the presented environmentally friendly gold removal method could therefore become economically viable and contribute to improving e-waste recycling. Furthermore, this technology could be used to remove other metals as well in a layer-by-layer sequence, e.g., first removing gold, then nickel, then copper and so forth. A sequential approach is already necessary for pyrometallurgy, bioleaching, and deep eutectic solvents to separate the different metals in e-waste. Hence, our method could also be added to other processes. It thus aligns well with UN SDG 12: Ensure sustainable consumption and production patterns.

## 5. Conclusion

A novel, green gold removal method for e-waste, based on HIFU-induced cavitation, was presented. Its benefits arise from using no chemicals (only water) and selectively removing only gold (and only minute amounts of nickel) from gold pads on discarded PCBs. The selectivity is achieved by first imaging the sample with the HIFU transducer to locate the gold pads and subsequently removing only the gold layer – only from the pads. The gold removal can be controlled by the number of sonicated bursts. With the increasing accumulation of e-waste and demand for PCBs, improved gold recycling methods are needed. Thus, this method could contribute to the United Nations Sustainable Development Goal 12: Ensure sustainable consumption and production patterns.

## CRediT authorship contribution statement

**Axi Holmström:** Writing – original draft, Visualization, Supervision, Methodology, Investigation, Funding acquisition, Formal analysis, Conceptualization. **Topi Pudas:** Writing – review & editing, Software, Methodology, Investigation. **Jere Hyvönen:** Writing – review & editing, Visualization, Software, Methodology, Investigation. **Martin Weber:** Writing – review & editing, Methodology, Investigation. **Kenichiro Mizohata:** Writing – review & editing, Methodology, Investigation. **Tom Sillanpää:** Writing – review & editing. **Joni Mäkinen:** Writing – review & editing, Formal analysis. **Antti Kuronen:** Writing – review & editing, Supervision, Conceptualization. **Tapio Kotiaho:** Writing – review & editing, Supervision, Conceptualization. **Edward Hæggström:** Writing – review & editing, Supervision. **Ari Salmi:** Writing – review & editing, Supervision, Funding acquisition, Conceptualization.

## Declaration of competing interest

The authors declare the following financial interests/personal relationships which may be considered as potential competing interests: Ari Salmi, Axi Holmström, Joni Mäkinen, Jere Hyvönen, Tom Sillanpää, Tapio Kotiaho, Antti Kuronen, Edward Hæggström has patent #WO2023281159A1 pending to University of Helsinki. Ari Salmi, Jere Hyvönen, Joni Mäkinen, Antti Kuronen, Axi Holmström, Topi Pudas, Tom Sillanpää, Tapio Kotiaho, Edward Hæggström has patent #WO2024062155A1 pending to University of Helsinki. If there are other authors, they declare that they have no known competing financial interests or personal relationships that could have appeared to influence the work reported in this paper.

## Acknowledgements

This work was supported by the Research Council of Finland (grant numbers 347459, 349200).

## Appendix A. Supplementary data

Supplementary data to this article can be found online at https://doi.org/10.1016/j.ultsonch.2024.107109.

## Data availability

Data will be made available on request.

## References

[1] M. Wang, Q. Tan, J.F. Chiang, J. Li, Recovery of rare and precious metals from urban mines—a review, Front. Env. Sci. Eng. 11 (5) (2017) 1–17, https://doi.org/10.1007/s11783-017-0963-1.

[2] C.P. Baldé, R. Kuehr, T. Yamamoto, R. McDonald, E. D'Angelo, S. Althaf, G. Bel, O. Deubzer, E. Fernandez-Cubillo, V. Forti, V. Gray, S. Herat, S. Honda, G. Iattoni, D.S. Khetriwal, V. Luda di Cortemiglia, Y. Lobuntsova, I. Nnorom, N. Pralat, M. Wagner, Global E-waste Monitor 2024, in: International Telecommunication Union (ITU) and United Nations Institute for Training and Research (UNITAR), Geneva/Bonn, 2024.

[3] X. Zeng, J.A. Mathews, J. Li, Urban mining of e-waste is becoming more cost-effective than virgin mining, Environ. Sci. Techno. 52 (8) (2018) 4835–4841, https://doi.org/10.1021/acs.est.7b04909.

[4] J. Cui, L. Zhang, Metallurgical recovery of metals from electronic waste: a review, J. Hazard. Mater. 158 (2–3) (2008) 228–256, https://doi.org/10.1016/j.jhazmat.2008.02.001.

[5] Metal Focus, Gold Focus 2020. https://www.metalsfocus.com/wp-content/uploads/2020/11/GOLD-FOCUS-2020.pdf, 2020 (accessed 11 June 2024).

[6] A. Mairizal, A. Sembada, K. Tse, N. Haque, M. Rhamdhani, Techno-economic analysis of waste PCB recycling in Australia, Resour. Conserv. Recy. 190 (2023) 106784, https://doi.org/10.1016/j.resconrec.2022.106784.

[7] United Nations, A/RES/70/1, Transforming our World: The 2030 Agenda for Sustainable Development. https://sdgs.un.org/sites/default/files/publications/21252030%20Agenda%20for%20Sustainable%20Development%20web.pdf, 2015 (accessed 11 June 2024).

[8] United Nations, United Nations Sustainable Development Goal 12: Ensure sustainable consumption and production patterns. https://sdgs.un.org/goals/goal12#targets_and_indicators, 2015 (accessed 11 June 2024).

[9] L.H. Xavier, M. Ottoni, L.P.P. Abreu, A comprehensive review of urban mining and the value recovery from e-waste materials, Resour. Conserv. Recy. 190 (2023) 106840, https://doi.org/10.1016/j.resconrec.2022.106840.

[10] A. Zupanc, J. Install, T. Weckman, M.M. Melander, M.J. Heikkilä, M. Kemell, K. Honkala, T. Repo, Sequential selective dissolution of coinage metals in recyclable ionic media, Angew. Chem. Int. Edit. 63 (31) (2024) e202407147, https://doi.org/10.1002/anie.202407147.

[11] M. Baniasadi, F. Vakilchap, N. Bahaloo-Horeh, S.M. Mousavi, S. Farnaud, Advances in bioleaching as a sustainable method for metal recovery from e-waste: a review, J. Ind. Eng. Chem. 76 (2019) 75–90, https://doi.org/10.1016/j.jiec.2019.03.047.

[12] M. Guo, R. Deng, M. Gao, C. Xu, Q. Zhang, Sustainable recovery of metals from e-waste using deep eutectic solvents: advances, challenges, and perspectives, Curr. Opin. Green Sustain. Chem. 47 (2024) 100913, https://doi.org/10.1016/j.cogsc.2024.100913.

[13] T. Ikeda, S. Yoshizawa, N. Koizumi, M. Mitsuishi, Y. Matsumoto, Focused ultrasound and lithotripsy, in: J.M. Escoffre, A. Bouakaz (Eds.), Therapeutic Ultrasound, vol 880, Springer, Cham, 2016, pp. 113–129, https://doi.org/10.1007/978-3-319-22536-4_7.

[14] S. Yoshizawa, T. Ikeda, A. Ito, R. Ota, S. Takagi, Y. Matsumoto, High intensity focused ultrasound lithotripsy with cavitating microbubbles, Med. Biol. Eng. Comput. 47 (8) (2009) 851–860, https://doi.org/10.1007/s11517-009-0471-y.

[15] V.A. Khokhlova, J.B. Fowlkes, W.W. Roberts, G.R. Schade, Z. Xu, T.D. Khokhlova, T.L. Hall, A.D. Maxwell, Y.N. Wang, C.A. Cain, Histotripsy methods in mechanical disintegration of tissue: Towards clinical applications, Int. J. Hyperthermia 31 (2) (2015) 145–162, https://doi.org/10.3109/02656736.2015.1007538.

[16] Z. Xu, T.L. Hall, E. Vlaisavljevich, F.T. Lee Jr, Histotripsy: the first noninvasive, non-ionizing, non-thermal ablation technique based on ultrasound, Int. J. Hyperthermia 38 (1) (2021) 561–575, https://doi.org/10.1080/02656736.2021.1905189.

[17] A. Karimi, J.L. Martin, Cavitation erosion of materials, Int. Met. Rev. 31 (1) (1986) 1–26, https://doi.org/10.1179/imtr.1986.31.1.1.

[18] Y. Tomita, A. Shima, Mechanisms of impulsive pressure generation and damage pit formation by bubble collapse, J. Fluid Mech. 169 (1986) 535–564, https://doi.org/10.1017/S0022112086000745.

[19] W.J. Tomlinson, S.J. Matthews, Cavitation erosion of aluminium alloys, J. Mater. Sci. 29 (4) (1994) 1101–1108, https://doi.org/10.1007/BF00351438.

[20] A. Philipp, W. Lauterborn, Cavitation erosion by single laser-produced bubbles, J. Fluid Mech. 361 (1998) 75–116, https://doi.org/10.1017/S0022112098008738.

[21] M. Dular, O.C. Delgosha, M. Petkovšek, Observations of cavitation erosion pit formation, Ultrason. Sonochem. 20 (4) (2013) 1113–1120, https://doi.org/10.1016/j.ultsonch.2013.01.011.

[22] M. Dular, T. Požar, J. Zevnik, R. Petkovšek, High speed observation of damage created by a collapse of a single cavitation bubble, Wear 418–419 (2019) 13–23, https://doi.org/10.1016/j.wear.2018.11.004.

[23] R.H. Richman, W.P. McNaughton, Correlation of cavitation erosion behavior with mechanical properties of metals, Wear 140 (1) (1990) 63–82, https://doi.org/10.1016/0043-1648(90)90122-Q.

[24] B. Jacobson, S. Li, R.M. Rivera, P. Daly, C.E. Elgar, D.M. Mulvihill, A.P. Abbott, A. Feeney, P. Prentice, A mechanistic study identifying improved technology critical metal delamination from printed circuit boards at lower power sonications in a deep eutectic solvent, Ultrason. Sonochem. 101 (2023) 106701, https://doi.org/10.1016/j.ultsonch.2023.106701.

[25] H.J. Sagar, O. el Moctar, Dynamics of a cavitation bubble near a solid surface and the induced damage, J. Fluid. Struct. 92 (2020) 102799, https://doi.org/10.1016/j.jfluidstructs.2019.102799.

[26] J. Watt, M.J. Austin, C.K. Simocko, D.V. Pete, J. Chavez, L.M. Ammerman, D. L. Huber, Formation of metal nanoparticles directly from bulk sources using ultrasound and application to e-waste upcycling, Small 14 (17) (2018) 1703615, https://doi.org/10.1002/smll.201703615.

[27] ASTM G-32 Standard: Standard Test Method for Cavitation Erosion Using Vibratory Apparatus, ASTM International, West Conshohocken, PA ,United States. https://www.astm.org/g0032-16r21e01.html.

[28] A. Holmström, T. Pudas, J. Hyvönen, T. Sillanpää, P. Lassila, J. Mäkinen, K. Mizohata, A. Kuronen, T. Kotiaho, A. Salmi, and E. Haeggström, Identifying Regions-of-Interest and Extracting Gold from PCBs Using MHz HIFU, in: 2022 IEEE International Ultrasonics Symposium (IUS), Venice, Italy, 2022. https://doi.org/10.1109/IUS54386.2022.9957863.

[29] T. Sillanpää, J. Hyvönen, J. Mäkinen, A. Holmström, T. Pudas, P. Lassila, R. Lepistö, A. Kuronen, T. Kotiaho, E. Hæggström, A. Salmi, Ultrasound-based surface sampling in immersion for mass spectrometry, J. Appl. Phys. 134 (10) (2023) 104901, https://doi.org/10.1063/5.0157705.

[30] J. Hyvönen, A. Holmström, T. Pudas, T. Sillanpää, P. Lassila, J. Mäkinen, A. Kuronen, T. Kotiaho, A. Salmi, and E. Haeggström, Focused-ultrasound-induced cavitation removes material in a controlled fashion, in: 2022 IEEE International Ultrasonics Symposium (IUS), Venice, Italy, 2022. https://doi.org/10.1109/IUS54386.2022.9957310.

[31] T. Pudas, J. Hyvönen, A. Holmström, T. Sillanpää, P. Lassila, J. Mäkinen, A. Kuronen, T. Kotiaho, A. Salmi, E. Haeggström, Machining of aluminium with MHz high-intensity focused ultrasound, in: 2022 IEEE International Ultrasonics Symposium (IUS), Venice, Italy, 2022. https://doi.org/10.1109/IUS54386.2022.9957698.

[32] A. Meriläinen, J. Hyvönen, A. Salmi, E. Hæggström, CESAM—coded excitation scanning acoustic microscope, Rev. Sci. Instrum. 92 (7) (2021) 074901, https://doi.org/10.1063/5.0047351.

[33] A. Holmström, A. Meriläinen, J. Hyvönen, A. Nolvi, T. Ylitalo, K. Steffen, R. Björkenheim, G. Strömberg, H.J. Nieminen, I. Kassamakov, J. Pajarinen, L. Hupa, A. Salmi, E. Hæggström, N.C. Lindfors, Evaluation of bone growth around bioactive glass S53P4 by scanning acoustic microscopy co-registered with optical interferometry and elemental analysis, Sci. Rep. 13 (2023) 6646, https://doi.org/10.1038/s41598-023-33454-y.

[34] P. Villars (Chief Editor), gold (Au, T = 300 K) Crystal Structure: Datasheet from "PAULING FILE Multinaries Edition – 2022" in: Inorganic Solid Phases, SpringerMaterials (online database), Springer, Heidelberg (ed.) SpringerMaterials, 2023. Available: https://materials.springer.com/isp/crystallographic/docs/sd_1628823 (accessed 4 June 2024).

[35] J.I. Thornycroft and S.W. Barnaby, "Torpedo-boat destroyers.(including appendix and plate at back of volume)," in Minutes of the Proceedings of the Institution of Civil Engineers (Thomas Telford-ICE Virtual Library), 122(1895), (1895), pp. 51-69. https://doi.org/10.1680/imotp.1895.19693.

[36] M. Plesset, A. Ellis, On the mechanism of cavitation damage, Trans. ASME 77 (7) (1955) 1055–1064, https://doi.org/10.1115/1.4014587.

[37] F. Reuter, C. Deiter, C.-D. Ohl, Cavitation erosion by shockwave self-focusing of a single bubble, Ultrason. Sonochem. 90 (2022) 106131, https://doi.org/10.1016/j.ultsonch.2022.106131.

[38] X.M. Liu, J. He, J. Lu, X.W. Ni, Effect of surface tension on a liquid-jet produced by the collapse of a laser-induced bubble against a rigid boundary, Opt. Laser Technol. 41 (1) (2009) 21–24, https://doi.org/10.1016/j.optlastec.2008.04.006.

[39] L. Biasiori-Poulanges, B. Lukić, O. Supponen, Cavitation cloud formation and surface damage of a model stone in a high-intensity focused ultrasound field, Ultrason. Sonochem. 102 (2024) 106738, https://doi.org/10.1016/j.ultsonch.2023.106738.

[40] M. Minnaert, XVI. On musical air-bubbles and the sounds of running water, The London, Edinburgh, and Dublin Philosophical Magazine and Journal of Science 16 (104) (1933) 235–248, https://doi.org/10.1080/14786443309462277.

[41] C.K. Holland, R.E. Apfel, An improved theory for the prediction of microcavitation thresholds, IEEE Trans. Ultrason. Ferroelectr. Freq. Control 36 (2) (1989) 204–208, https://doi.org/10.1109/58.19152.

[42] K.B. Bader, E. Vlaisavljevich, A.D. Maxwell, For whom the bubble grows: physical principles of bubble nucleation and dynamics in histotripsy ultrasound therapy, Ultrasound Med. Biol. 45 (5) (2019) 1056–1080, https://doi.org/10.1016/j.ultrasmedbio.2018.10.035.

[43] K. Maeda, A.D. Maxwell, T. Colonius, W. Kreider, M.R. Bailey, Energy shielding by cavitation bubble clouds in burst wave lithotripsy, J. Acoust. Soc. Am. 144 (5) (2018) 2952–2961, https://doi.org/10.1121/1.5079641.

[44] S. Hattori, T. Hirose, K. Sugiyama, Prediction method for cavitation erosion based on measurement of bubble collapse impact loads, Wear 269 (7–8) (2010) 507–514, https://doi.org/10.1016/j.wear.2010.05.015.

[45] P. Riesz, D. Berdahl, C. Christman, Free radical generation by ultrasound in aqueous and nonaqueous solutions, Environ. Health Perspect. 64 (1985) 233–252, https://doi.org/10.1289/ehp.8564233.

[46] E. Lahtinen, L. Kivijärvi, R. Tatikonda, A. Väisänen, K. Rissanen, M. Haukka, Selective recovery of gold from electronic waste using 3D-printed scavenger, ACS Omega 2 (10) (2017) 7299–7304, https://doi.org/10.1021/acsomega.7b01215.

[47] M. Peydayesh, E. Boschi, F. Donat, R. Mezzenga, Gold recovery from e-waste by food-waste amyloid aerogels, Adv. Mater. 36 (19) (2024) 2310642, https://doi.org/10.1002/adma.202310642.

[48] T. Xue, T. He, L. Peng, O.A. Syzgantseva, R. Li, C. Liu, D.T. Sun, G. Xu, R. Qiu, Y. Wang, S. Yang, J. Li, J.-R. Li, W.L. Queen, A customized MOF-polymer composite for rapid gold extraction from water matrices, Sci. Adv. 9 (13) (2023) eadg4923, https://doi.org/10.1126/sciadv.adg4923.

## Appendix A. Supplementary materials

# Gold Removal from E-Waste Using High-Intensity Focused Ultrasound

Axi Holmström[a]*, Topi Pudas[a], Jere Hyvönen[a], Martin Weber[a], Kenichiro Mizohata[b], Tom Sillanpää[a,c], Joni Mäkinen[a], Antti Kuronen[b], Tapio Kotiaho[c,d], Edward Hæggström[a], Ari Salmi[a]

[a] Electronics Research Laboratory, Faculty of Science, University of Helsinki, P.O.B. 64, FIN-00014 University of Helsinki, Finland.

[b] Accelerator Laboratory, Faculty of Science, University of Helsinki, P.O.B. 43, FIN-00014 University of Helsinki, Finland.

[c] Drug Research Program and Division of Pharmaceutical Chemistry and Technology, Faculty of Pharmacy, University of Helsinki, P.O.B. 56, FIN-00014 University of Helsinki, Finland.

[d] Department of Chemistry, Faculty of Science, University of Helsinki, P.O.B 55, FIN-00014 University of Helsinki, Finland.

*Corresponding author: axi.holmstrom@helsinki.fi, Electronics Research Laboratory, Faculty of Science, P.O.B. 64, FIN-00014 University of Helsinki, Finland

## S1: Voltage and pressure measurement with maximum amplitudes at the focus

The voltage and pressure measurements were conducted by driving the transducer (impedance matching included) with maximum settings in water. The maximum input voltage and maximum RF gain (set to 100 %) of the power amplifier (500A100A, Amplifier Research, USA) was used. The voltage signals were stable, and four signals were recorded. An example signal is shown in Fig. S1a. The transducer reaches a maximum amplitude after 5 cycles and settles after 2 µs (20 cycles). To determine the stable peak-to-peak amplitude $U_{\mathrm{PP}}$, one positive peak and its subsequent negative peak were selected manually at ~ 3 µs for each signal. From these values, the peak-to-peak voltage was calculated to be $U_{\mathrm{PP}} = (397.6 \pm 0.4)$ V. As the driving electronics can drift during long sonications, the voltage was reported as an integer value of $U_{\mathrm{PP}} = 398$ V.

The maximum pressure was measured directly at the focus using an optical hydrophone (ONDA HFO-690, Ø = 100 µm, Onda Corporation, USA) and 15 signals were recorded (Fig. S1b). As is seen in Fig. S1b, cavitation commenced after 3-4 cycles (3 rarefactive, 4 compressive), after which the signal was lost. At the third positive and negative peaks, the hydrophone signal was still reasonably stable and the voltage at these peaks were also close to the stable voltage values (10-15 % difference). The peak-positive and peak-negative-pressures, $P_{\mathrm{PPP}}$ and $P_{\mathrm{PNP}}$, were estimated from these peaks (marked with green asterisks in Fig. S1b). To convert the hydrophone's voltage signals to pressure, the Small Signal Sensitivity $SSS = 5.57$ mV/MPa provided by the device and a frequency-dependent tip scattering correction were used (T = 20.3°C) [1]. As the signals end abruptly due to onset of cavitation, the signals were not processed entirely in the frequency domain as described in [1], which introduces errors without careful windowing. Instead, the pressure was first calculated from the voltage signal using the $SSS$ to obtain $P_{\mathrm{SSS}}$, and then corrected with the frequency-dependent tip scattering correction factor $k = 0.459$ calculated for 11.8 MHz, i.e. $P_{\mathrm{corrected}} = k \cdot P_{\mathrm{SSS}}$. Thus, the peak-positive and peak-negative pressures (marked with green asterisks in Fig. S1b) were obtained: $P_{\mathrm{PPP}} = (46 \pm 1)$ MPa and $P_{\mathrm{PNP}} = (-35 \pm 5)$ MPa (mean ± 1 SD).

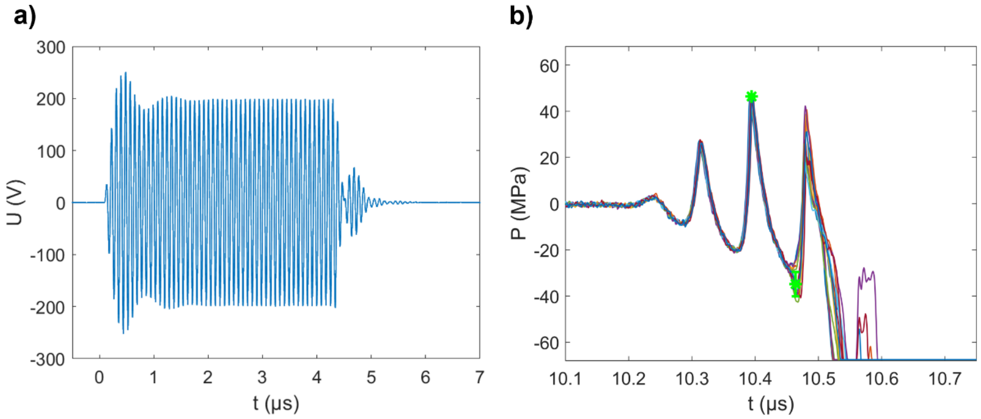

Fig. S1. Maximum voltage and pressure when measured at maximum amplitude at the focus. **a)** Example voltage signal. The $U_{\mathrm{PP}}$ = 398 V was determined from consecutive positive and negative peaks at ~ 3 µs from four measured signals. **b)** 15 pressure signals measured at the focus. The signal was lost when cavitation began (after 10.5 µs). The peaks used to estimate $P_{\mathrm{PPP}}$ and $P_{\mathrm{PNP}}$ are indicated with green asterisks, giving $P_{\mathrm{PPP}} = (46 \pm 1)$ MPa and $P_{\mathrm{PNP}} = (-35 \pm 5)$ MPa (mean ± 1 SD of the signals). The hydrophone signal begins at 10.2 µs, which is the travel time of the sound to the focus 15 mm from the transducer.

## S2: Example of CESAM images from one sonicated gold pad

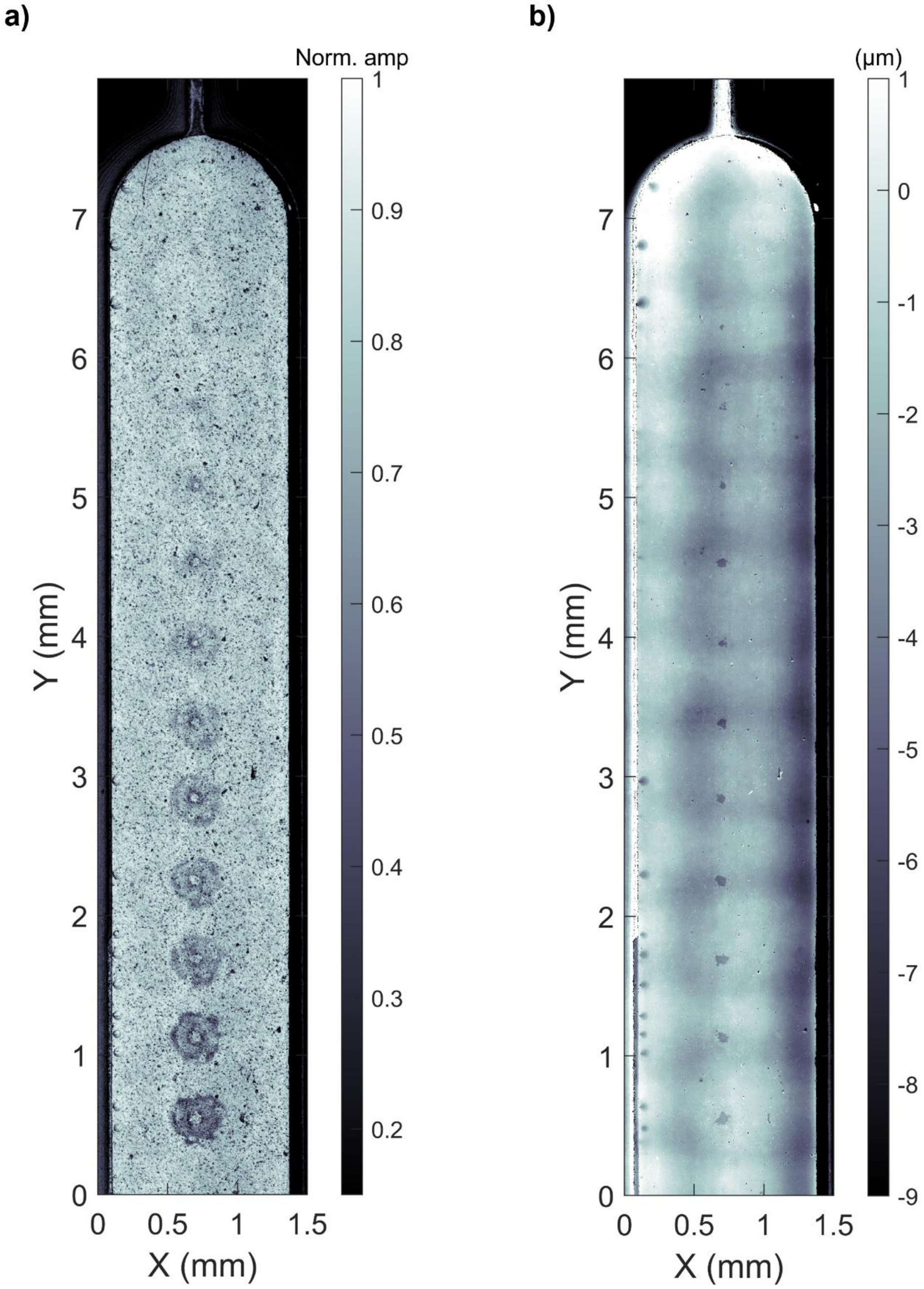

Fig. S2. CESAM images of one gold pad from one burst sweep. The number of bursts increases from top to bottom. Both the **a)** amplitude map and the **b)** topography map are obtained simultaneously. The surface roughening is clearly seen in the amplitude map and the deep holes at the center of the erosion mark, used for removal analysis, are also visible in the topography map. Fig. 3b & c are cut from the region between Y = 1.9 mm and Y = 4.2 mm. The erosion hole shown in Fig. 4b is from a different gold pad, but imaged with CESAM with the same parameters as shown here. The resolution is thus identical in all CESAM images.

## S3: Calculation of used electrical energy

To determine the electrical energy used at the transducer, the four voltage signals (one example shown in Fig. S1a) were used. As the signals were not perfect sinusoids, the energy was calculated for each as the integral

$$E_{elec} = \int_{t_1}^{t_2} \frac{u(t)^2}{R} dt$$

where $u(t)$ is the voltage signal, $t_1$ and $t_2$ are the beginning and end times of the signal, respectively (where the signal first exceeds and last returns to 0 V), and $R$ is the resistance of the load (transducer). Because of the impedance matching to the transducer, a purely resistive load of $R = 50\ \Omega$ was used. This might be slightly inaccurate, but should not introduce errors larger than a few percent. The obtained electrical energy was 1.7 mJ per burst (the difference in energies between signals was < 2 ‰).

To calculate the energy efficiency of the gold removal for different bursts, the masses (mean ± 1 SD) of removed gold were divided by the electrical energy used (i.e., multiplying the number of bursts with 1.7 mJ per burst) and normalized to the maximum mean value.

## References

[1] ONDA HFO-690 User’s manual, section 2. Principle of operations, eq. 1-12.

# Effect of HIFU frequency on gold removal efficiency from e-waste

Topi Pudas[a*], Axi Holmström[a], Jere Hyvönen[a], Tom Sillanpää[a,b], Joni Mäkinen[a], Martin Weber[a], Kenichiro Mizohata[c], Antti Kuronen[c], Tapio Kotiaho[b,d], Edward Hæggström[a], Ari Salmi[a]

[a] Electronics Research Laboratory, Faculty of Science, University of Helsinki, P.O.B. 64, FIN-00014 University of Helsinki, Finland

[b] Drug Research Program and Division of Pharmaceutical Chemistry and Technology, Faculty of Pharmacy, University of Helsinki, P.O.B. 56, FIN-00014 University of Helsinki, Finland

[c] Accelerator Laboratory, Faculty of Science, University of Helsinki, P.O.B. 43, FIN-00014 University of Helsinki, Finland

[d] Department of Chemistry, Faculty of Science, University of Helsinki, P.O.B 55, FIN-00014 University of Helsinki, Finland

*Corresponding author.

E-mail address: topi.pudas@helsinki.fi (T. Pudas).

## Abstract

The depletion of mineable gold reserves, paired with the increase in demand for electronics, underlines the need for sustainable gold recycling methods. Given its high concentration of precious metals, particularly gold, e-waste is a prime candidate for gold recovery. Established e-waste recycling methods, namely pyro- and hydrometallurgy, remain taxing to the environment, involving harmful emissions and toxic byproducts. This study expands on a recently reported green, ultrasound-based, technology for recycling gold from discarded printed circuit boards (PCBs). The method uses localized cloud cavitation in water, driven by high-intensity focused ultrasound (HIFU), to mechanically remove gold from the surface of PCB edge connectors. In this work, the effect of ultrasound frequency on gold removal is studied, and a significant increase in efficiency is shown. Gold removal experiments were conducted with three custom-built HIFU transducers operating at 4.2 MHz, 7.3 MHz, and 11.8 MHz. The electrical driving parameters were kept constant for all transducers. The focal-plane pressure field of each transducer was determined using transient nonlinear acoustic holography. The results revealed that gold removal at 4.2 MHz was 4.6 and 3.8 times more efficient than at 11.8 MHz and 7.3 MHz, respectively. Direct comparison of the erosion marks to the pressure fields revealed that complex frequency-dependent cavitation cloud dynamics are likely responsible for the increase in removal efficiency at the lowest frequency employed. By improving the gold removal efficiency of the proposed HIFU method, this study contributes to ongoing progress towards industrial viability of a scalable and eco-friendly technology for urban mining.

Keywords: urban mining, high-intensity focused ultrasound, e-waste recycling, sustainable technology, cavitation

# 1. Introduction

Beyond its decorative value in jewelry and intrinsic economic reliability throughout human history, gold is important in many industries including electronics, aerospace and biomedicine. By current estimates, 64 kt of gold remains in mineable natural reserves [1]. Based on the average annual output of 3.6 kt over the past decade [2], the known mineable gold reserves are expected to run out within the next 20 years. In addition to mining, 1.2 kt/year of gold is sourced from recycled products, of which e-waste constitutes less than 5 % [3]. In 2022, from the documented 62 000 kt of produced e-waste, less than 25 % was collected and recycled [4]. While printed circuit boards constitute only a fraction of e-waste, they are appealing for recycling due to their high content of rare and precious metals (RPMs). Compared to mined ore, the concentration of gold in PCBs is 400-800 times higher [3]. Although gold accounts for merely 0.02 % of the weight of PCBs, it constitutes 50 % of the raw materials cost, as reported in a 2020 study [5]. Gold in PCBs is predominantly used on the surface of edge connectors due to its corrosion resistance and high electrical conductivity.

PCB recycling is mostly done with traditional methods, comprising a combination of mechanical, pyro-, and hydrometallurgical processes. PCBs typically first undergo manual disassembly and crushing/shredding, followed by the removal of non-metallic substances by incineration (pyrometallurgy), and finally the remaining metals are separated through multiple phases of chemical leaching (hydrometallurgy) [6]. While effective for RPM recovery, these traditional methods are energy intensive and taxing to the environment, involving harmful emissions and toxic byproducts [7–10]. Alternative greener methods are being developed, including bioleaching, electrochemical technology, ionic liquid technology, supercritical fluid technology, and mechanochemical technology [11]. Currently these emerging technologies remain limited in either RPM recovery rates or economic viability.

This paper expands on a recently reported novel green technology for gold recovery from intact PCBs [12]. The method employs high-intensity focused ultrasound (HIFU) in water to mechanically remove gold from the surface of edge connectors. The gold removal relies on imploding cavitation bubbles formed at the focus of a high-intensity acoustic field. Because the method selectively targets surface gold, it can be directly applied to intact PCBs. Here the gold removal efficiency is significantly improved, contributing to the ongoing progress towards industrial viability. The approach towards efficiency improvement is guided by existing literature in the medical field, where HIFU applications are well-documented.

Eroding surfaces with HIFU-induced cavitation is an established technology in the medical field, where it is used for noninvasive comminution of kidney stones (lithotripsy) and ablation of tissue (histotripsy) [13]. Beyond the medical field, applications of HIFU-induced cavitation have been little explored. One reported application involves using HIFU to break down biological samples in water for DNA extraction [14,15]. Two distinct HIFU applications were also demonstrated in previous work: controlled surface machining of aluminum [16] and a non-contact surface sampling technique [17]. While the dynamics of single-bubble cavitation is understood, HIFU involves the formation and subsequent collapse of bubble clusters (cloud cavitation) within the focal volume of the acoustic field. Over the past decade, experiments and simulations have unveiled complex phenomena related to cloud cavitation-induced erosion, including e.g., high-pressure secondary rebound shockwaves, the deviation of cloud resonant frequency from its natural frequency, and the interplay between acoustic pressure, frequency, cloud and bubble size, gas volume fraction and stand-off distance of the initial bubble cloud [18]. Despite impressive progress, the interplay of the complex dynamics associated with cloud cavitation-induced erosion remains to be fully resolved. For instance, there is ambiguity in whether cloud collapse propagates inward in an amplifying manner, or if outer bubbles shield inner ones from the incident pressure waves that induce collapse – the dynamics of which depend on the acoustic field and initial conditions of the cloud and its constituent bubbles.

For single bubbles, the pressure threshold for onsetting cavitation decreases with frequency [19]. Qualitatively this can be understood as lower frequencies imparting a longer bubble growth time during the rarefaction phase, resulting in a larger maximum bubble radius and a more energetic collapse [20]. In focused acoustic fields, higher frequencies (shorter wavelengths) undergo less diffraction, resulting in more confined focal beams, i.e., higher focusing gains. Cloud-cavitation HIFU experiments have shown that bubble density increases and bubble size decreases with increasing frequency [21], which agrees with the aforementioned observations on single-bubble dynamics and focused fields. While high frequencies increase focusing gain and low frequencies reduce the cavitation threshold, the collapse energy of a cavitation bubble ultimately depends on its maximum size. It is therefore expected that lower frequencies are preferable for HIFU-induced cavitation erosion due to both a lower cavitation threshold, and a prolonged bubble expansion phase.

In HIFU applications, nonlinear acoustics plays an important role. As waves propagate towards the focus and the acoustic intensity increases, the propagating waveform becomes distorted through harmonic generation [22]. In experiments the focal acoustic field should be characterized, since it drives cavitation cloud formation and dynamics – and by extension the ensuing cavitation erosion. The focal pressure field cannot be directly measured since cavitation bubbles impede the incident pressure waves from reaching the sensing element (hydrophone). Instead, the focal pressure field can be resolved by nonlinear transient acoustic holography, which involves measuring the pressure waveforms across a plane between the transducer and its focus, and numerically propagating the waveforms to the focus, taking into account cumulative nonlinearity arising from the increasing acoustic intensity [23,24].

In this paper the gold removal efficiency of a novel green e-waste recycling method is improved, indicating progress towards industrial relevance. Improvement is achieved by experiments, whereby the effect of acoustic frequency on the removal efficiency of gold from PCB edge connectors is investigated. Three custom-built transducers, with identical geometries and different resonant frequencies, 4.2 MHz, 7.3 MHz, and 11.8 MHz, were used to first image the PCB at low power to locate the gold, then driven at high power to remove it. Erosion efficiency at the different frequencies is compared, revealing that lowering the frequency indeed improves the gold removal efficiency. Finally, the acoustic field of each transducer is resolved using nonlinear transient acoustic holography to better understand their erosion capabilities.

# 2. Methods

## 2.1 Experimental Setup

A schematic of the experimental setup is shown in Fig. 1. A PCB sample with gold-plated edge connectors was submerged in de-ionized water (RiOs Essential Water Purification Systems, Milli-Q, Germany). The water was degassed for 1 h prior to HIFU experiments to maintain comparable gas concentrations between experiments. A custom-built HIFU transducer was mounted to a 3-axis motorized linear stage (NLS4 NEMA 17 MDrive, Newmark Systems Inc., USA). Three transducers with different resonant frequencies were used, each comprising an epoxy-backed (GlassCast, Easy

Composites Ltd., UK) bowl-shaped piezo (Type Pz26, $f_c$ = [4.2, 7.3, 11.8] MHz, Ø = 19 mm, $R$ = 15 mm, CTS Ferroperm, Denmark) in a 3D-printed acrylonitrile styrene acrylate (ASA) housing, and electrically matched to 50 Ω with LC matching circuits. Excitation signals were produced with a signal generator (AFG31052 series, Tektronix, USA), and amplified with a Class A RF amplifier (500A100A, Amplifier Research, USA). The excitation signal and received echoes were monitored with a digital oscilloscope (Picoscope 5442D, Pico Technology, UK).

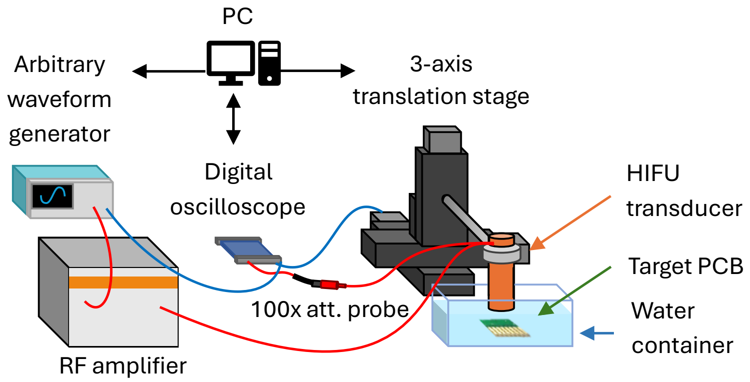

**Figure 1:** Schematic of the experimental setup.

A photo of the target PCB is shown in Fig. 2A. The thickness of the edge connector layers (1.6 µm gold on 1.9 µm nickel) was chara cterized by Rutheford backscattering spectroscopy using a 3 MeV proton beam. To locate the gold pads, the sample was imaged with each transducer using Gaussian amplitude-modulated linear chirps (relative bandwidth 24 %). Example amplitude maps are shown in Fig. 2B. High-amplitude echoes from the connectors are distinguishable from the low-amplitude echoes from the epoxy-fiberglass substrate for all transducers.

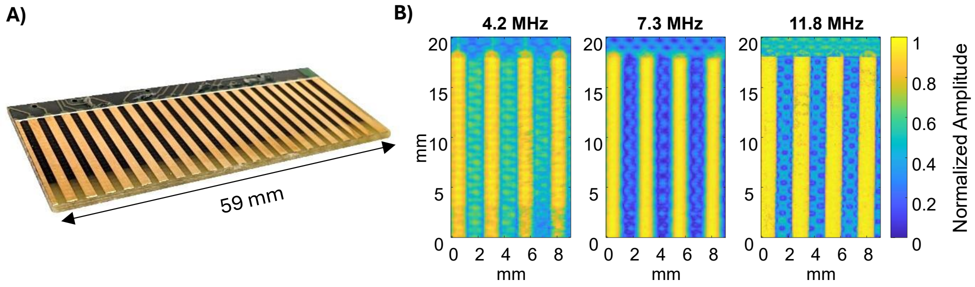

**Figure 2:** A) Photo of the target PCB, B) Amplitude maps of the PCB sample produced with different transducers, showing high amplitude from gold and low amplitude from epoxy-fiberglass substrate.

## 2.2. Characterizing removed gold

The removed gold volume was quantified from optical microscope images (Stemi 2000-C, Carl Zeiss AG, Germany; DCC1645C CMOS camera, Thorlabs, USA). The resolution of the images was calibrated to 1.4 µm/pixel with a calibration target (1951 USAF Resolution Test Targets, Ø = 1", Thorlabs, USA). The gold volume was calculated by converting the number of pixels (depleted of gold) to surface areas, then multiplying with the measured gold thickness.

## 2.3. Gold removal

Two sets of gold removal experiments were conducted. The optimal transducer-sample distance for each transducer was first identified with a sequence of sonications. At the optimal distance for each transducer, a sequence of sonications with a varying number of bursts was then performed to evaluate gold removal efficiency.

### 2.3.1. Transducer-sample distance optimization

Based on preliminary experiments, an appropriate range and increment of transducer-sample distances, and sonication parameters were selected. For each transducer the focus, from which the largest amplitude echo was received, served as the reference zero-position. Positive (negative) distances imply retracting (approaching) the transducer away from (towards) the PCB surface. The range of distances and steps for each transducer were: ±1400 µm at 200 µm steps for 4.2 MHz, (-600 – +2200) µm at 200 µm steps for 7.3 MHz, and (-500 – +900) µm at 100 µm steps for 11.8 MHz. The transducers were driven with a peak-to-peak excitation voltage of $U_{\mathrm{pp}} = 430$ V, and the resultant pressure fields were determined using acoustic nonlinear transient holography (Section 2.4). Other sonication parameters were the same for all frequencies: $500 \times 10^3$ bursts, 50 cycles, and 500 Hz pulse-repetition-frequency (PRF).

### 2.3.2. Removal efficiency optimization

To compare the removal efficiency, sets of sonications were performed with different burst counts. Based on the previous experiment (Section 2.3.1), sonications for each transducer were conducted at the transducer-sample distance yielding the largest gold removal volume. Sonication parameters were kept constant between transducers: $U_{\mathrm{pp}} = 430$ V, 50 cycles, 500 Hz PRF, and burst counts ranging from $(0.1 – 1.9) \times 10^6$ at steps of $0.2 \times 10^6$. These sonications were repeated three times, randomizing the order of burst count values.

## 2.4. Acoustic field characterization

Direct pressure measurements in the focal volume are obscured by the presence of cavitation bubbles. Therefore, a transient nonlinear acoustic holography numerical method, adapted from Jing et al. [23], was implemented in MATLAB. For each transducer, pressure waveforms were measured in the nearfield across a plane perpendicular to the acoustic axis. The measured waveforms were then numerically propagated with a stepping algorithm, derived from the Westervelt equation:

$$P(z+\Delta z) = P(z)\exp(iK\Delta z) + \frac{\beta\omega^2}{2i\rho_0 c_0^4 K} P(z)\exp(K\Delta z) \otimes P(z)\exp(K\Delta z)\Delta z \qquad (1)$$

Where $P$ is the 3D Fourier transform of pressure, $\Delta z$ the propagation step, $K$ the dispersion relation ($K = \omega^2/c_0^2 - k_x^2 - k_y^2 - i\delta\omega^3/c_0^4$, where $k_x$ and $k_y$ are the wave vector components, and $\delta$ the sound diffusivity), $\beta$ the nonlinearity parameter ($\beta = 1 + B/2A$, where $A$ and $B$ are the coefficients of the linear and quadratic terms in the Taylor expansion of pressure as a function of density), $\omega$ the angular frequency, $\rho_0$ the ambient density, $c_0$ the speed of sound, and $\otimes$ is the convolution operator (with respect to $k_x, k_y, \omega$). In place of physical sound diffusivity [22], a small artificial diffusivity (larger than the physical sound diffusivity) was needed to reduce the Gibbs effect, serving as a low-pass filter to counter the accumulation of high-frequency noise and maintain stability of the numerical simulation [24,25]. For each frequency, the diffusivity was incrementally increased until stable results were obtained. The diffusivities used were $8 \cdot 10^{-4}$ m$^2$/s for 4.2 MHz, $3 \cdot 10^{-4}$ m$^2$/s for 7.3 MHz and $2 \cdot 10^{-4}$ m$^2$/s for 11.8 MHz. Pressure measurements were conducted 5 mm above the transducer focus with a fiberoptic hydrophone (HFO-690 [Ø = 100 µm], ONDA, USA), across a (10 x 10) mm$^2$ plane with a step size of 25 µm. Recorded voltage signals were deconvolved with the hydrophone sensitivity using a custom MATLAB script.

# 3. Results

## 3.1. Acoustic field characterization

The average focal radial-pressure-amplitude profiles for the three transducers, obtained by nonlinear acoustic holography, are presented in Fig. 3. Relevant geometric dimensions of the profiles are indicated in the figure: the positive (FWHM$^+$) and negative (FWHM$^-$) full-width half-maxima and the distance between the first side-lobe maxima (DSLM). As expected, all these dimensions decrease with increasing frequency; high frequencies undergo less diffraction than low frequencies, leading to a narrower focal beam width. While the focal maximum pressure increases from 4.2 MHz (152 MPa) to 11.8 MHz (187 MPa), it is smallest for 7.3 MHz (107 MPa). An increase in maximum pressure would be expected for higher frequencies due to tighter focusing and higher harmonic generation. The same discrepancy for 7 MHz is observed for the focal minimum pressures: -40 MPa for 4 MHz, -25 MPa for 7 MHz and -35 MPa for 12 MHz. The ratio of focal maximum to side-lobe maximum gives an indication of the degree of focusing, a higher value indicating that a larger fraction of acoustic energy resides in the focal beam. These ratios for 4.2 MHz, 7.3 MHz, and 11.8 MHz were 9.8, 3.9 and 16.4, respectively. Although the ratio is expected to increase with frequency, it was lowest for 7.3 MHz. This discrepancy could be due to a slight deviation from the expected spherical geometry of the piezo element, or defective epoxy-piezo adhesion.

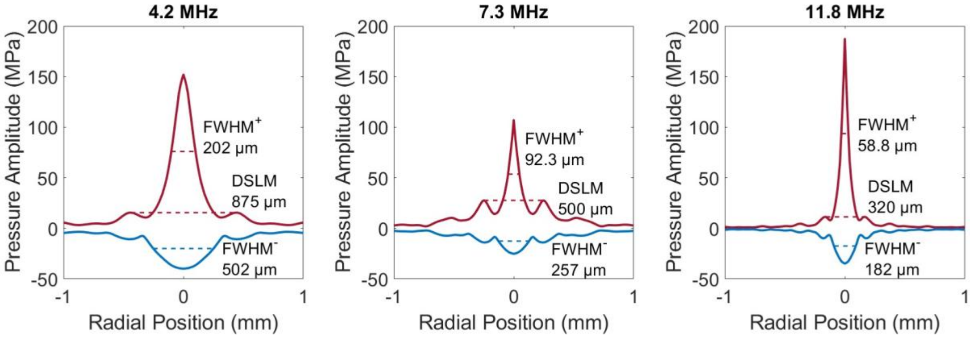

**Figure 3:** Average focal radial positive (red) and negative (blue) pressure amplitude profiles for the three transducers, obtained by nonlinear transient acoustic holography. The positive (FWHM$^+$) and negative (FWHM$^-$) full-width half-maxima, and the distance between the first side-lobe maxima (DSLM) are shown. FWHM$^+$, FWHM$^-$, and DSLM decrease with increasing frequency due to reduced diffraction at higher frequencies. The maximum pressure, and the ratio between the maximum pressure and side-lobe maxima, is highest for 11.8 MHz, indicating a higher focusing gain.

## 3.2. Transducer-sample distance optimization

Optical microscope images and the calculated removed gold volumes for different defocusing distances are presented in Fig. 4, Fig. 5. The defocus is defined as the offset from the transducer-sample distance at which a maximal echo amplitude is observed. Both figures show that gold removal increases progressively to a maximum near the focus (the distance at which recorded echo is maximized), after which the removal tapers off. Two calculated erosion volumes are shown in Fig. 5: the largest volume is calculated from the largest individual erosion area at each position (top), and the total volume is calculated from the sum of the largest erosion area and any smaller peripheral removal areas (bottom). For all frequencies most gold was removed at a slight positive defocus. This result is in agreement with previous work, where it was shown that most effective stone comminution with HIFU was obtained at a slight positive defocus, corresponding to a region where the (ellipsoidal) acoustic beam at the stone surface is widest [26]. Optimal defocuses for removal were selected as: +200 µm, +500 µm and +200 µm for 4.2 MHz, 7.3 MHz and 11.8 MHz, respectively.

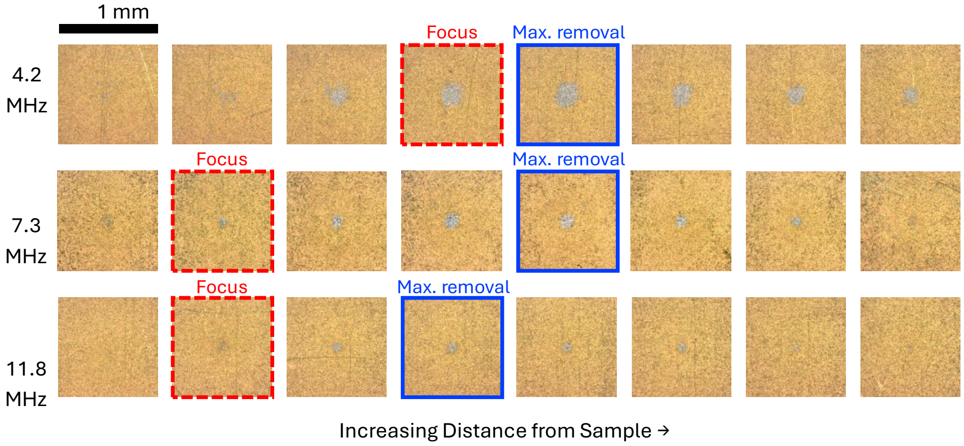

**Figure 4:** Optical microscope images of removed gold at different transducer-sample distances for the three transducers. The focus of each transducer, defined as the position at which the recorded echo is maximized, is indicated with red dashed borders. No values are given for the defocus distances due to differing step sizes between frequencies (200 µm for 4.2 MHz and 7.3 MHz, and 100 µm for 11.8 MHz). Removal increases with transducer-sample distance up to a maximum (indicated with blue borders), after which removal tapers off. For all frequencies maximal removal is observed slightly beyond the focus (Fig. 5).

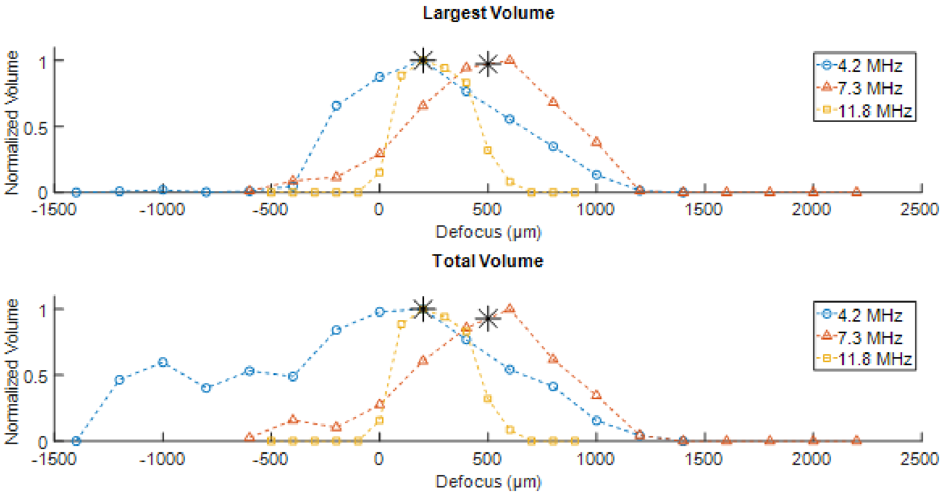

**Figure 5:** Removed gold volume as function of defocus. The largest volume (top) is calculated from the single largest continuous removed gold area, and the total volume (bottom) from the sum of all removed gold areas. For all frequencies, the volumes are normalized to their respective maximum. For all frequencies maximum removal is observed above the focus, around which removal tapers off. For 4.2 MHz significant removal in total volume is observed also at negative defocuses, owing to dispersed small removal spots. Asterisks (*) denote the selected optimal defocuses: +200 µm for 4.2 MHz and 11.8 MHz, and +500 µm for 7.3 MHz. Lines are shown to guide the eye.

## 3.3. Removal efficiency characterization

In this study, removal efficiency is defined as the removed gold volume normalized by the input electrical energy. Optical microscope images of gold removal with an increasing number of burst counts are shown in Fig. 6. Geometric features of the focal pressure fields (Fig. 3) are overlayed on select images. The removal patterns are similar for 7.3 MHz and 11.8 MHz. Removal is mostly confined to a small focal area which grows with increasing bursts. A dark peripheral ring appears at 0.7 × $10^6$ bursts, which for 7.3 MHz develops into sporadic gold removal with higher burst numbers. For 4.2 MHz scattered gold removal is observed already at 0.3 × $10^6$ bursts, which expands in area with increasing bursts. Deep pitting is observed for 4.2 MHz, revealing copper beneath the exposed nickel layer. For all frequencies, at low burst counts the removal area corresponds to the FWHM$^+$, and the largest removal area at high burst counts to the FWHM$^-$. For 7.2 MHz and 11.8 MHz, the peripheral ring corresponds to the DSLM.

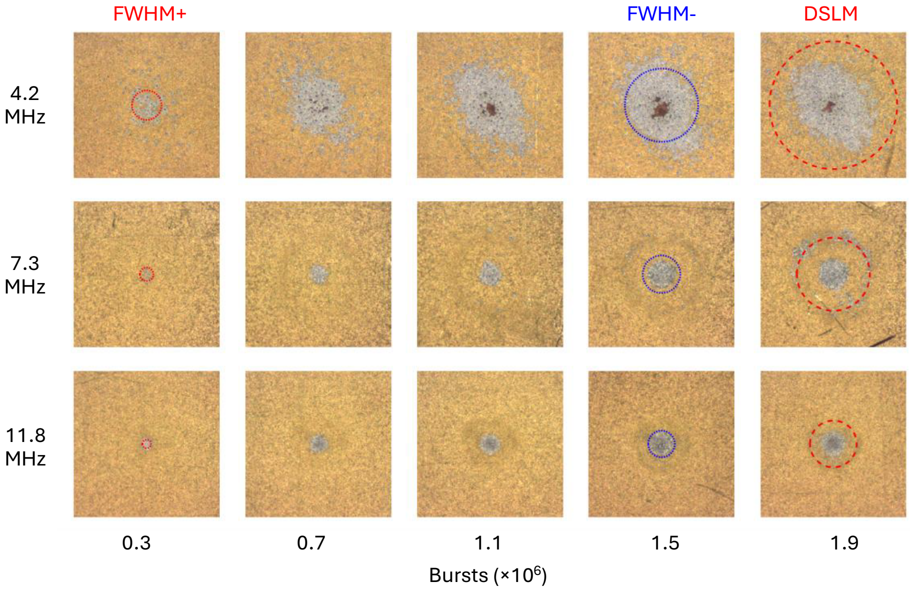

**Figure 6:** Optical microscope images of gold removal using different burst counts for the three transducers. Geometric features of the focal pressure fields (from Fig. 3) are shown as overlayed circles: positive amplitude full-width half-maximum (FWHM+, first column), negative amplitude full-width half-maximum (FWHM-, second last column), and distance between positive side-lobe maxima (DSLM, last column). For all frequencies these features correlate with gold removal progression; at low bursts (0.3 × 106) removal is confined within the FWHM+, at high burst counts (1.5 × 106) the maximum central removal area correlates with the FWHM-. For 7.3 MHz and 11.8 MHz at high burst counts (1.9 × 106), the peripheral removal ring correlates with the DSLM. For all frequencies removal increases with burst count.

The calculated removed gold volumes as a function of sonication burst counts are shown in Fig. 7. For all frequencies increasing the burst counts removes more gold. The removed volume increases with decreasing frequency, although there is only a marginal increase from 11.8 MHz to 7.3 MHz. Only for 7.3 MHz, there is a clear difference in the trends between the largest and total removed volumes. Due to significant gold removal in the side-lobe region, commencing at 1.5 × $10^6$ bursts, the total volume increases more aggressively at high burst counts.

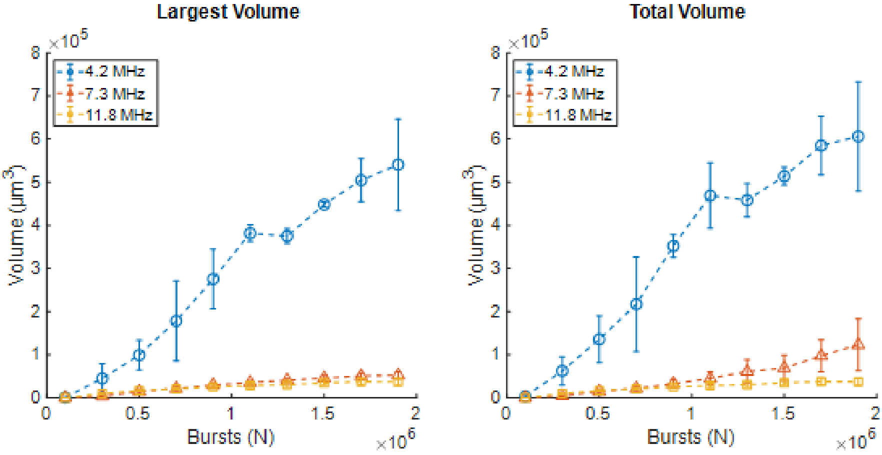

**Figure 7:** Removed gold volume as a function of burst count. The data is the average of three experiments ± 1 SD. Largest volume (left) is calculated from the largest individual removed gold area, and total volume (right) from the sum of all removed gold areas. Lines are shown to guide the eye. The removed gold volume increases with decreasing frequency.

For the three transducers, the electrical excitation signal amplitude and the number of cycles per burst were kept constant. Hence the input electrical energy was not constant at each burst count value; lower frequencies have a longer temporal period, which implies that for the same number of cycles per burst, the energy content will be higher for lower frequencies. It should also be noted that all three transducers were electrically matched to 50 Ω and built with piezos of the same material with the same electromechanical coupling coefficients. To compare gold removal efficiency, the burst sweep data (Fig. 7) was normalized with the total input electrical energy, calculated from burst duration and peak-to-peak voltage ($U_{pp} = 430$ V). The removed gold volumes per input electrical energy as a function of burst count is shown in Fig. 8.

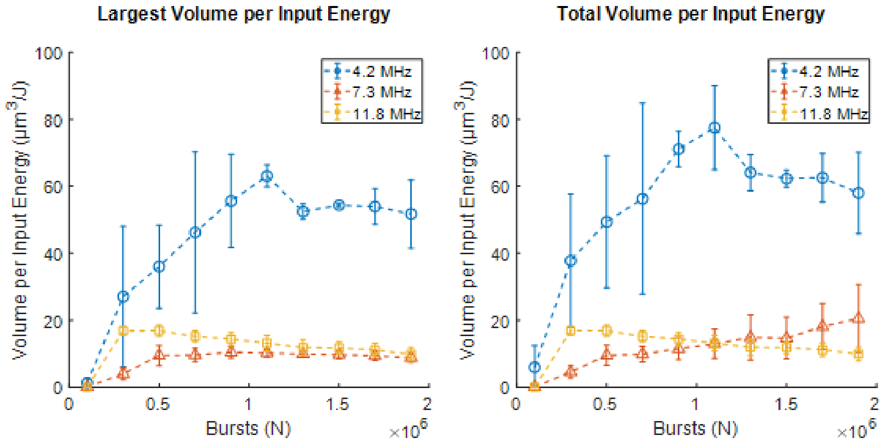

**Figure 8:** Removed gold volume normalized by the input electrical energy, as function of burst count. The data is the average of three experiments ± 1 SD. Largest volume (left) is calculated from the largest individual removed gold area, and total volume (right) from the sum of all removed gold areas. A maximum in largest volume removal efficiency is observed for all frequencies, after which removal rate diminishes. For 7.3 MHz the total volume removal rate does not reach a maximum, owing to significant removal within the sidelobe. Lines are shown to guide the eye.

For the largest gold volumes (Fig. 8, left) all frequencies undergo a rapid increase in gold removal efficiency upto a maximum, followed by a gradual decline. The efficiency maxima indicate that the main lobe has become void of gold, after which subsequent bursts remove gold at a diminished rate. While the rate diminishes, it does not halt entirely; cavitation is evidently most prominent within the high-amplitude main lobe, but less frequent cavitation events are expected to occur in the side-lobes and in the region between the main lobe and the side lobes (pressure amplitude does not drop to zero between the main and side lobes, as seen in Fig. 3). For 7.3 MHz, the total gold volume removal efficiency (Fig. 8, right) does not seem to saturate to a maximum. This can be attributed to the onset of significant gold removal within the sidelobes (Fig. 6), the prominence of which can be attributed to the relatively large side-lobe pressure amplitude (Fig. 3). Comparing the ratio of efficiency maxima for each transducer, 4.2 MHz (at $1.1 \times 10^6$ bursts) is 4.6 times more efficient than 11.8 MHz (at $0.3 \times 10^6$ bursts) and 3.8 times more efficient than 7.3 MHz (at $1.9 \times 10^6$ bursts).

# 4. Discussion

Recovering gold from e-waste is in principle a sustainable solution to the scarcity of mineable gold. However, established recycling methods are harmful to the environment, producing toxic fumes, using caustic substances and generating large volumes of wastewater [7–10]. Environmentally friendly alternatives have emerged over the past decade, but they remain limited in either recovery efficiency, economic viability, or only target one step in traditional methods. This paper builds upon a green, chemical-free HIFU-based method for removing gold from intact PCBs recovered from e-waste using only HIFU in water [12]. Reducing sonication frequency is expected to increase the erosion potential of acoustic cavitation [21]. Due to the complexity of bubble-bubble and shockwave-bubble interactions, the prominence of different erosion mechanisms in cloud cavitation have not been fully resolved.

Here, the effect of frequency on gold removal efficiency was investigated using three custom-built transducers operating at different frequencies (4.2 MHz, 7.3 MHz, 11.8 MHz). The transducers featured identical geometry, were built from the same materials including the piezo element, and were all electrically matched to 50 Ω. In sonication experiments, the transducers were driven with identical parameters (amplitude, cycles per burst, burst count, PRF). For each transducer, the focal pressure field was resolved with nonlinear transient acoustic holography. Direct comparison of erosion marks to the resolved focal pressure fields provides qualitative insight into the cloud dynamics and resulting erosion mechanisms.

The results demonstrated that lower frequencies were more efficient at removing gold; 4.2 MHz was 4.6 and 3.8 times more efficient than 11.8 MHz and 7.3 MHz, respectively. Interestingly, erosion marks with the 4.2 MHz transducer differed from the other two frequencies. At high burst counts, the higher frequencies showed distinct gold removal areas corresponding to the main lobe ($\mathrm{FWHM}^-$, Fig. 6) and the first side-lobe (DSLM, Fig. 6). Removal with 4.2 MHz was confined within the main lobe, although removal at the edges was highly dispersed. Also, with 4.2 MHz, deep pitting occurred at the center of the removal area, revealing copper underneath the exposed nickel. These discrepancies hint at a difference in cloud dynamics. As discussed in the Introduction, low drive frequencies promote the growth of larger cavitation bubbles, which subsequently collapse with high energy [20]. Following the initial collapse of a cavitation bubble, a toroidal ring of small microbubbles typically forms [27]. The size of this toroid increases with the maximum radius of the initial bubble [28], which would imply that rebound microbubbles will be more dispersed at low frequencies than at high frequencies. In the context of this study, over the course of repeated bursts these microbubbles serve as cavitation-facilitating nucleation sites, and would be expected to eventually disperse beyond the focal volume. Particularly at the edges of the cavitating region, the more intense dynamics could explain the less defined and more dispersed erosion area observed at 4.2 MHz. A similar effect of cloud spreading due to remnant microbubbles was recently observed in a study on HIFU ablation of a tissue-mimicking phantom, where the effect of PRF on cloud geometry and lesion formation was investigated [29].

The deep center pitting for 4.2 MHz was mainly confined within the dimension of the positive amplitude main lobe ($FWHM^+$, Fig. 6). Based on literature, lower frequencies are expected to reduce bubble density within the cavitation cloud [21]. A lower bubble density would imply less bubble shielding, effectively allowing the incident pressure waves to penetrate deeper into the cavitating volume. While the negative pressure drives bubble formation, the subsequent positive peak can reflect off the bubble surface. Due to the low impedance of gas compared to liquid water, the incident high-amplitude positive peak can be reflected off and inverted by the bubble, amplifying both bubble growth and the subsequent collapse intensity [30]. This back-scattering amplification, together with a reduced bubble density, could explain the deep central pitting observed with 4.2 MHz. For 7.3 MHz and 11.8 MHz, at low ($0.3 \times 10^6$) bursts where gold removal was first observed, the removal spots corresponded to the width of the positive amplitude main lobe (FWHM+, Fig. 6), which could also be explained by back-scattering. Once the bubble cloud grows over subsequent acoustic cycles, however, due to a higher bubble density, bubble shielding likely reduces the amplification effect.

A decision had to be made on how to best compare frequencies in a fair manner. In the context of the technological application, energy efficiency was of primary interest. The three transducers featured identical geometries and piezo elements of the same material, and all were matched electrically to 50 Ω. The input electrical parameters were kept constant: amplitude, cycles, PRF. Other viable approaches would have been to vary the amplitude or number of cycles to keep the electrical power constant. A constant number of cycles was selected so that bubbles would be exposed to the same number of acoustic cycles regardless of frequency, allowing observed erosion effects to be attributed more directly to frequency-specific dynamics rather than sonication time. The excitation amplitude was selected based on the equipment available, being the maximum output amplitude of the commercial amplifier, which was observed to be sufficient for gold removal at all three frequencies. While the focal acoustic pressures varied between the transducers, as seen in the post hoc nonlinear acoustic holography results (Fig. 3), a constant electrical amplitude was used during experiments. This approach, which was adopted prior to detailed pressure field characterization, ensured consistent input conditions across transducers and simplified interpretation of frequency-dependent erosion trends.

Already previously, it was estimated that the removed gold value exceeded the cost of electricity used even at low gold yields [12]. While the gold removal efficiency was much improved in this study, the method remains slow; the highest gold removal efficiency was obtained with $1.1 \times 10^6$ bursts using the 4.2 MHz transducer, which required 37 min sonication at a PRF of 500 Hz. Presently the PRF was limited by the thermal stability of the piezos used; higher PRFs caused excessive heating, leading to fractures in the piezo. Adding passive or active cooling to the transducer would increase heat dissipation from the piezo, which might allow for higher PRFs.

Further reducing the excitation frequency could improve efficiency, however, a lower frequency generates a larger main lobe and thus a larger cavitation region. The observed approx. 500 µm diameter gold removal spot size for 4.2 MHz is already suitable for PCB edge connectors, which have typical widths of hundreds of micrometers. A larger spot size would both waste energy by initiating cavitation on areas where there is no gold and lead to the removal of adjacent materials (e.g. epoxy). Furthermore, the deep pitting (exposing copper, Fig. 6) would likely increase with lower frequencies.

The purpose of this study was to improve gold removal efficiency; however, no effort was made to collect the removed gold. Recovering and separating the removed metals (gold, nickel, copper), could be carried out with established methods. Recovery should be straightforward with traditional methods e.g. filtration, evaporation, centrifugation. Since nickel is ferromagnetic (unlike gold and copper), it is separable with magnetic separation techniques [31], while copper could be separated e.g. using environmentally friendly electrochemical methods [32].

# 5. Conclusion

Building on the proof-of-concept demonstrated in previous work [12], this study focused on improving the efficiency of a novel green e-waste recycling technology. Three ultrasound transducers operating at different frequencies were used to remove gold from PCB edge connectors via HIFU-induced cavitation. Comparison of the erosion profiles to focal pressure fields, resolved by nonlinear acoustic holography, hints at the complexity of the dynamics at play in cloud cavitation. The lowest frequency (4.2 MHz) showed 3.8 and 4.6 times more efficient gold removal than 7.3 MHz and 11.8 MHz, respectively.

# Acknowledgements

This work was supported by the Research Council of Finland (grant numbers 347459, 349200).

# Data Availability

Data will be made available on request.

# References

[1] Mineral Commodity Summaries 2025, U.S. Geological Survey, 2025. https://pubs.usgs.gov/periodicals/mcs2025/mcs2025.pdf (accessed March 31, 2025).
[2] Gold Demand Trends: Full Year 2024, World Gold Council, 2025.
[3] Precious Metals E-waste Recovery Market: Global Forecast to 2025, Markets and Markets, 2020.
[4] The Global E-waste Monitor 2024, United Nations Institute for Training and Research, 2024. https://ewastemonitor.info/wp-content/uploads/2024/12/GEM_2024_EN_11_NOV-web.pdf (accessed March 31, 2025).
[5] H. Cui, C. Anderson, Hydrometallurgical Treatment of Waste Printed Circuit Boards: Bromine Leaching, Metals 10 (2020) 462. https://doi.org/10.3390/met10040462.
[6] L.H. Xavier, M. Ottoni, L.P.P. Abreu, A comprehensive review of urban mining and the value recovery from e-waste materials, Resour. Conserv. Recycl. 190 (2023) 106840. https://doi.org/10.1016/j.resconrec.2022.106840.
[7] V. Sahajwalla, R. Hossain, The science of microrecycling: a review of selective synthesis of materials from electronic waste, Mater. Today Sustain. 9 (2020) 100040. https://doi.org/10.1016/j.mtsust.2020.100040.
[8] G. Eduljee, R.M. Harrison, eds., Electronic waste management, 2nd edition, Royal Society of Chemistry, London, 2020.

[9] S. Kumar, V. Kumar, John Wiley & Sons, eds., Electronic waste management: policies, processes, technologies, and impact, JW-Wiley, Hoboken, NJ, 2024.

[10] M.N.V. Prasad, M. Vithanage, A. Borthakur, Handbook of electronic waste management: international best practices and case studies, Butterworth-Heinemann, Oxford, 2020.

[11] M. Wang, Q. Tan, J.F. Chiang, J. Li, Recovery of rare and precious metals from urban mines—A review, Front. Environ. Sci. Eng. 11 (2017) 1. https://doi.org/10.1007/s11783-017-0963-1.

[12] A. Holmström, T. Pudas, J. Hyvönen, M. Weber, K. Mizohata, T. Sillanpää, J. Mäkinen, A. Kuronen, T. Kotiaho, E. Hæggström, A. Salmi, Gold removal from e-waste using high-intensity focused ultrasound, Ultrason. Sonochem. 111 (2024) 107109. https://doi.org/10.1016/j.ultsonch.2024.107109.

[13] T. Large, A.E. Krambeck, Emerging Technologies in Lithotripsy, Urol. Clin. North Am. 46 (2019) 215–223. https://doi.org/10.1016/j.ucl.2018.12.012.

[14] H.R. Holmes, M. Haywood, R. Hutchison, Q. Zhang, C. Edsall, T.L. Hall, D. Baisch, J. Holliday, E. Vlaisavljevich, Focused ultrasound extraction (FUSE) for the rapid extraction of DNA from tissue matrices, Methods Ecol. Evol. 11 (2020) 1599–1608. https://doi.org/10.1111/2041-210X.13505.

[15] A. Stettinius, H. Holmes, Q. Zhang, I. Mehochko, M. Winters, R. Hutchison, A. Maxwell, J. Holliday, E. Vlaisavljevich, DNA release from plant tissue using focused ultrasound extraction (FUSE), Appl. Plant Sci. 11 (2023) e11510. https://doi.org/10.1002/aps3.11510.

[16] T. Pudas, J. Hyvönen, A. Holmström, T. Sillanpää, P. Lassila, J. Mäkinen, A. Kuronen, T. Kotiaho, A. Salmi, E. Hæggström, Machining of Aluminium with MHz High-Intensity Focused Ultrasound, in: 2022 IEEE Int. Ultrason. Symp. IUS, IEEE, Venice, Italy, 2022: pp. 1–4. https://doi.org/10.1109/IUS54386.2022.9957698.

[17] T. Sillanpää, J. Hyvönen, J. Mäkinen, A. Holmström, T. Pudas, P. Lassila, R. Lepistö, A. Kuronen, T. Kotiaho, E. Hæggström, A. Salmi, Ultrasound-based surface sampling in immersion for mass spectrometry, J. Appl. Phys. 134 (2023) 104901. https://doi.org/10.1063/5.0157705.

[18] B. Jia, H. Soyama, Non-Spherical Cavitation Bubbles: A Review, Fluids 9 (2024) 249. https://doi.org/10.3390/fluids9110249.

[19] C.K. Holland, R.E. Apfel, An improved theory for the prediction of microcavitation thresholds, IEEE Trans. Ultrason. Ferroelectr. Freq. Control 36 (1989) 204–208. https://doi.org/10.1109/58.19152.

[20] C. Guo, The Relationship between the Collapsing Cavitation Bubble and Its Microjet near a Rigid Wall under an Ultrasound Field, in: W. Borek, T. Tański, M. Król (Eds.), Cavitation - Sel. Issues, IntechOpen, 2018. https://doi.org/10.5772/intechopen.79129.

[21] C. Edsall, E. Ham, H. Holmes, T.L. Hall, E. Vlaisavljevich, Effects of frequency on bubble-cloud behavior and ablation efficiency in intrinsic threshold histotripsy, Phys. Med. Biol. 66 (2021) 225009. https://doi.org/10.1088/1361-6560/ac33ed.

[22] M.F. Hamilton, D.T. Blackstock, eds., Nonlinear acoustics, Academic Press, San Diego, CA, 1998.

[23] Y. Jing, M. Tao, G.T. Clement, Evaluation of a wave-vector-frequency-domain method for nonlinear wave propagation, J. Acoust. Soc. Am. 129 (2011) 32–46. https://doi.org/10.1121/1.3504705.

[24] Y. Jing, J. Cannata, T. Wang, Experimental verification of transient nonlinear acoustical holography, J. Acoust. Soc. Am. 133 (2013) 2533–2540. https://doi.org/10.1121/1.4796120.

[25] G. Arfken, H.J. Weber, G.B. Arfken, H.-J. Weber, Mathematical methods for physicists, 6. ed., 5. [print., international ed.], Elsevier Academic Press, Amsterdam, Heidelberg, 2008.

[26] L. Biasiori-Poulanges, B. Lukić, O. Supponen, Cavitation cloud formation and surface damage of a model stone in a high-intensity focused ultrasound field, Ultrason. Sonochem. 102 (2024) 106738. https://doi.org/10.1016/j.ultsonch.2023.106738.

[27] W. Lauterborn, W. Hentschel, Cavitation bubble dynamics studied by high speed photography and holography: part one, Ultrasonics 23 (1985) 260–268. https://doi.org/10.1016/0041-624X(85)90048-4.

[28] A. Philipp, W. Lauterborn, Cavitation erosion by single laser-produced bubbles, J. Fluid Mech. 361 (1998) 75–116. https://doi.org/10.1017/S0022112098008738.

[29] A. Simon, C. Edsall, A. Maxwell, E. Vlaisavljevich, Effects of pulse repetition frequency on bubble cloud characteristics and ablation in single-cycle histotripsy, Phys. Med. Biol. 69 (2024) 025018. https://doi.org/10.1088/1361-6560/ad11a1.

[30] A.D. Maxwell, T.-Y. Wang, C.A. Cain, J.B. Fowlkes, O.A. Sapozhnikov, M.R. Bailey, Z. Xu, Cavitation clouds created by shock scattering from bubbles during histotripsy, J. Acoust. Soc. Am. 130 (2011) 1888–1898. https://doi.org/10.1121/1.3625239.

[31] B. Elvers, G. Bellussi, eds., Ullmann’s encyclopedia of industrial chemistry, 7th, completely rev. ed ed., Wiley-VCH, Weinheim, 2011.

[32] S. Fogarasi, F. Imre-Lucaci, A. Egedy, Á. Imre-Lucaci, P. Ilea, Eco-friendly copper recovery process from waste printed circuit boards using Fe3+/Fe2+ redox system, Waste Manag. 40 (2015) 136–143. https://doi.org/10.1016/j.wasman.2015.02.030.

www.nature.com/scientificreports

scientific reports

OPEN

# Evaluation of bone growth around bioactive glass S53P4 by scanning acoustic microscopy co-registered with optical interferometry and elemental analysis

Axi Holmström[1]✉, Antti Meriläinen[1], Jere Hyvönen[1], Anton Nolvi[1], Tuomo Ylitalo[1], Kari Steffen[1], Robert Björkenheim[2], Gustav Strömberg[3], Heikki J. Nieminen[1,4], Ivan Kassamakov[1], Jukka Pajarinen[5], Leena Hupa[6], Ari Salmi[1], Edward Hæggström[1] & Nina C. Lindfors[3]

Bioactive glass (BAG) is a bone substitute that can be used in orthopaedic surgery. Following implantation, the BAG is expected to be replaced by bone via bone growth and gradual degradation of the BAG. However, the hydroxyapatite mineral forming on BAG resembles bone mineral, not providing sufficient contrast to distinguish the two in X-ray images. In this study, we co-registered coded-excitation scanning acoustic microscopy (CESAM), scanning white light interferometry (SWLI), and scanning electron microscopy with elemental analysis (Energy Dispersive X-ray Spectroscopy) (SEM–EDX) to investigate the bone growth and BAG reactions on a micron scale in a rabbit bone ex vivo. The acoustic impedance map recorded by the CESAM provides high elasticity-associated contrast to study materials and their combinations, while simultaneously producing a topography map of the sample. The acoustic impedance map correlated with the elemental analysis from SEM–EDX. SWLI also produces a topography map, but with higher resolution than CESAM. The two topography maps (CESAM and SWLI) were in good agreement. Furthermore, using information from both maps simultaneously produced by the CESAM (acoustic impedance and topography) allowed determining regions-of-interest related to bone formation around the BAG with greater ease than from either map alone. CESAM is therefore a promising tool for evaluating the degradation of bone substitutes and the bone healing process ex vivo.

Bone substitutes are commonly used in orthopaedic surgery when bone tissue is missing due to trauma, infection, or bone tumour surgery. The most commonly used bone substitutes are autograft bone, allograft bone, and different kinds of synthetic bone substitutes, such as bioactive glass (BAG), calcium sulphate, ß-tricalcium phosphate (ß-TCP), hydroxyapatite (HA) or (ß-TCP)/(HA)-based bone substitutes[1]. The expected biological response of the implanted material is integration with bone followed by gradual remodelling or dissolution of the bone substitute with simultaneous bone ingrowth. Eventually, the implanted material should be replaced by bone.

BAG, invented by Larry Hench and co-workers in the late 1960s, is a synthetic silica-based bone substitute with proven bone bonding, osteoconductive, and osteostimulative properties[2]. The bone-formation-supporting

[1]Electronics Research Laboratory, Department of Physics, University of Helsinki, Helsinki, Finland. [2]Department of Orthopaedics and Traumatology, Department of Surgery, Helsinki University Hospital, University of Helsinki, Helsinki, Finland. [3]Department of Hand Surgery, Department of Surgery, Helsinki University Hospital, University of Helsinki, Helsinki, Finland. [4]Medical Ultrasonics Laboratory (MEDUSA), Department of Neuroscience and Biomedical Engineering, Aalto University, Espoo, Finland. [5]Department of Plastic Surgery, Department of Surgery, Helsinki University Hospital, University of Helsinki, Helsinki, Finland. [6]Johan Gadolin Process Chemistry Centre, Åbo Akademi University, Turku, Finland. ✉email: axi.holmstrom@helsinki.fi

characteristics of BAG are known to depend on controlled dissolution and precipitation processes at the surface of the BAG starting immediately after implantation. A rapid ion exchange of alkalis at the surface of the glass to hydrogen ions in the solution, followed by dissolution and repolymerization of soluble silica (Si), results in a Si-rich layer. Finally, calcium phosphate (CaP) nucleates and crystallizes to hydroxyapatite on top of the Si-layer at the surface of the BAG[3].

BAG-S53P4 (in wt.%: 53% $SiO_2$, 23% NaO, 20% CaO and 4% $P_2O_5$) has documented osteoconductive, osteostimulative, angiogenetic, and antibacterial properties[4–7]. Antimicrobial overuse has led to increased antibiotic resistance worldwide, and therefore, new innovations to combat infections are needed. The verified antibacterial properties of BAG-S53P4 makes it a promising tool in bone infection treatment. Due to its chemical reactions at the glass surface with subsequent elevation of pH and osmotic pressure, BAG-S53P4 has been shown to kill both planktonic bacteria and bacteria in biofilm[8], thus making it one of the most interesting and promising bone substitutes to combat infections. Clinically, BAG-S53P4 is used in bone cavity filling and infection treatment in orthopaedic surgery[9–11].

Radiographs are a common approach to characterize bone healing. However, as the HA-layer forming around BAGs resembles bone mineral, the contrast between the bone substitute and bone, and subsequently the evaluation of bone formation, is limited using current clinical applications, such as X-ray and computed tomography (CT). During the bone healing process, while new bone forms and the bone substitute disappears, the treated region appears more and more dense on X-rays and CT, making evaluation of the bone remodelling area difficult. Furthermore, studies have shown that bone mass density, determined from degree of mineralised bone as measured by synchrotron-radiation μCT, does not correlate significantly with elastic properties of bone[12,13]. Acoustic impedance, measured by scanning acoustic microscopy (SAM), is a more reliable measure[12,13].

Scanning Acoustic Microscopy (SAM) employs highly-focused scanning ultrasound (US) at frequencies typically in the range of 10 MHz–2 GHz[12,14–16]. Since sound is a travelling density disturbance, the wave propagation of US is associated with the elasticity of materials with which it interacts. US, therefore, provides a mechanical contrast mechanism for imaging. More explicitly, in SAM, at each measured point, an ultrasonic pulse is transmitted from a focused transducer towards the sample and the reflected echo recorded. The Time-of-Flight of the echo provides the distance to the sample and allows constructing a topography map of the sample surface. The amplitude of the reflected echo, on the other hand, is determined by the difference in acoustic impedance of the imaging medium (typically water, $Z=1.5$ MRayl) and the surface material (provided that the sample is flat and non-scattering). The acoustic impedance $Z$ is the product of a material's density, ρ, and speed of sound, $c$, ($Z=\rho c$) and is also related to the material stiffness $C$ as $C=Zc$. The unit of $Z$ is Rayl = $kg/(m^2 \cdot s)$. The amplitudes of the reflected echoes in SAM thus provide an acoustic impedance map. Therefore, SAM has been used to spatially map elasticity-associated properties of materials, such as acoustic impedance, as well as shear and bulk moduli[15,17]. Practical bone-related applications include spatial characterization of bone[12,13,18–21] and cartilage[22–24].

The lateral resolution of SAM is limited by diffraction, typically enabling microscopic resolutions of 2–23 μm[12,19,20,25]. In SAM surface imaging (as opposed to subsurface imaging), axial resolution is dependent on the accuracy of determining the Time-of-Flight of the received echoes, provided that the surface is in focus. Usually, short pulses are used to obtain high axial resolution. Unfortunately, short pulses contain little energy, and hence the amplitudes of received echoes are low. This decreases the signal-to-noise ratio (SNR) of the acoustic impedance map, which is problematic for imaging soft samples. Utilizing coded excitation in SAM, i.e., transmitting long signals (to deposit more energy) with modulated frequency content (to allow accurately determining the Time-of-Flight), improves both the axial resolution and signal-to-noise ratio (SNR)[26]. With coded-excitation scanning acoustic microscopy (CESAM), features as small as ~ 150 nm in height can be distinguished on a surface[26]. CESAM could therefore provide an improved imaging modality, especially for bone-related samples, which contain both hard materials and soft tissue.

Scanning White Light Interferometry (SWLI) is a rapid contactless and label-free optical microscopy imaging method that can resolve topographical heights of spatially large areas down to sub-nanometer scale[27]. It relies on the short coherence length of white light to compare the optical distances from a light source to the sample and to a reference mirror[28]. The sample is imaged by scanning axially with a piezo actuator and recording images as a function of height. The recorded light-intensity changes from each pixel are then calculated with surface detection algorithms and a 3D topographical map of the sample is generated[29]. SWLI is feasible for imaging bio-related samples, such as oral implants[30] and printed drug-laden polymer structures[31]. The spatial resolution of the SWLI is in practice mainly limited by the objective magnification. Higher magnifications can be used to gain higher resolution down to the diffraction limit, but the imaging area of a single scan is then reduced. Stitching methods can be used to combine partially overlapping multiple sub-aperture scans into a single large image[32]. This way, high spatial resolution can be achieved, while maintaining large area coverage. As with SAM, the maximum achievable lateral resolution is limited by the diffraction limit to approximately half of the centre wavelength of the used light[33]. As the wavelength of light (400–700 nm) is much shorter than that of ultrasound (6 μm in this study), SWLI is less sensitive to surface roughness and local inclinations in the sample surface.

The aim of this study was to determine the feasibility of our custom-built coded-excitation SAM (CESAM)[26,34,35] for discerning differences in mechanical properties in the BAG structure and surrounding bone tissue in a leporine bone sample. This was achieved by co-registering the measured acoustic impedance with elemental analysis of SEM–EDX and the CESAM topography map with SWLI. All three techniques require an ex vivo bone sample, but studying bone formation ex vivo can still provide valuable insight into remodelling mechanisms and stages. The results suggest that CESAM could allow investigating bone healing with BAG ex vivo. The acoustic impedance map of CESAM is, however, sensitive to surface roughness, as the amplitude and frequency content of the reflected echoes can be distorted due to scattering. SWLI, which operates at shorter wavelengths than SAM, was used to validate the CESAM surface topography map. The topography maps were compared to evaluate the possibility of using only the CESAM topography map to determine scattering regions, i.e., regions with higher uncertainty in acoustic impedance. Furthermore, utilizing information from both the acoustic impedance and topography maps generated by the CESAM allowed determining regions-of-interest related to bone formation around the BAG with greater confidence. CESAM, therefore, can serve as a stand-alone tool for investigating bone formation ex vivo.

## Results

To validate the CESAM, a leporine femoral epicondyle with a BAG-S53P4 implant was imaged ex vivo. Quantitative images recorded with SEM (including elemental analysis with EDX), SWLI, and CESAM were manually co-registered (Fig. 1, left). For close inspection, we obtained data about the composition of the sample (SEM–EDX), its surface topography (CESAM and SWLI), and acoustic impedance (CESAM) along one scan-line (Fig. 1). This scan line was chosen to intersect with both the centre of a glass granule and surrounding newly-forming bone, featuring several different materials of interest. Similarities in the structures apparent in the different images allowed the manual co-registration. Regions-of-interest along the scan line (i–vii) were selected as shown in Fig. 1.

**Region (i).** Along the scan line, from 0 to 140 µm, the region shows high silicon content as well as intermediate sodium and calcium content (Fig. 1a). The elemental composition (high Si content, moderate and similar Na and Ca content) matches that of the glass granules in BAG. In the topography maps from both the SWLI (Fig. 1b) and the CESAM (Fig. 1c, black curve), a comparatively flat region is visible. The acoustic impedance (Fig. 1c, red curve) in this region is high, $Z = 7.7 \pm 1.2$ MRayl (mean ± 1 SD). The dip in acoustic impedance at the very beginning of Region (i) is caused by a small surface defect also visible in both topography maps. Excluding this dip yields an acoustic impedance for Region (i) of $Z = 8.0 \pm 0.9$ MRayl. The high acoustic impedance confirms the presence of a hard material, i.e. glass. This is further supported by the presence of a flat surface in both SWLI and CESAM topography maps.

**Region (ii–iii).** As the BAG is implanted, a thick Si-layer is formed immediately at the glass surface, onto which a thin HA-layer, containing CaP, is formed[36,37]. In Region (ii) (140–160 µm), the SEM–EDX shows a spike in Si and C along with a gradual increase in both Ca and P. This gradual increase in Ca and P, starting in Region (ii) and continuing into Region (iii), supports the hypothesis that the HA-layer is located at the border between Regions (ii) and (iii). Bone formation occurs gradually on top of the HA-layer, which is indicated by constant Ca and P contents accompanied by decreasing Si-content and increasing C-content in Region (iii) (160–205 µm). The acoustic impedance of the flat Region (iii) shows a moderate acoustic impedance, reaching $Z = 5.4 \pm 0.3$ MRayl, with a curve shape resembling the Si-, Ca-, and P-content. Both the SWLI and the CESAM topography maps show a notch, containing a minute particulate, in Region (ii) between the glass granule and the surrounding bone formation layer. Similar narrow notches are also visible between all other glass granules and their surrounding bone formation layers. The apparent low acoustic impedance in Region (ii), $Z = 1.8 \pm 0.2$ MRayl, which is based on the amplitude of the reflected echo, can be explained by significant sound scattering in the vicinity of this narrow notch.

**Region (iv).** SEM–EDX shows a high C content in Region (iv) (205–320 µm) with no Si, Ca, P, or Na, and CESAM shows a low acoustic impedance, $Z = 2.5 \pm 0.3$ MRayl (for comparison, the acoustic impedance of water is 1.5 MRayl). These properties could be indicative of the presence of connective tissue. However, the homogeneity of the acoustic impedance map in this area (Fig. 1c, left) suggests that the material is not tissue, but the fixing agent epoxy. Similar homogeneous patches are seen elsewhere between glass granules in the impedance map, supporting this proposition. The topography maps from both SWLI and CESAM further support this, as they show a smooth ridge ~ 5 µm higher than the surroundings. Connective tissue would not form such a smooth ridge. This ridge could be the product of insufficient polishing time with the initial coarse sandpaper of the sample. The sample was polished with P4000 sandpaper in the final polishing phase, which should remove sharp edges, but a smooth ridge has remained.

**Region (v–vi).** Region (v) (320–375 µm) displays an increase in Ca and P, which indicates the presence of bone tissue. In this region, the shape of the acoustic impedance curve follows the shape of the Ca- and P-curve. The low acoustic impedance, peaking at $Z = 3.2$ MRayl simultaneously with Ca and P, suggests that this tissue has not yet mineralized. The topography maps from SWLI and CESAM differ somewhat in this area; both display a notch in Region (vi) (375–395 µm), but the flatter region in Region (v) is almost 1 µm higher when measured with CESAM. The notch is also visible in SEM–EDX. At the right edge of Region (vi), the Si, Ca and P levels begin to increase, as the line starts intersecting the bone formation layer around granule (B).

**Region (vii).** In the left part of Region (vii), from 395 to 435 µm, the Si content continues to increase, and C, Ca and P are present. This is accompanied by an increase in acoustic impedance, reaching $Z = 5.4$ MRayl, again in phase with the Ca and P content, similar to that seen in Region (iii). This suggests bone formation on top of the HA-layer of granule (B), containing Si and CaP. At 450 µm, CaP is no longer present and Si has further increased, which suggest that the scan line intersects the thick Si-layer around granule (B) in a tangential direction. In Region (ii), the scan line intersects the Si-layer around granule (A) radially for a short distance and the notch induces scattering, resulting in an apparent low acoustic impedance. In Region (vii), the acoustic impedance estimate from 435 µm to the end of the line is more reliable (both the CESAM topography map and SWLI show a flat region). The acoustic impedance in this Si-layer is $Z = 3.1 \pm 0.4$ MRayl.

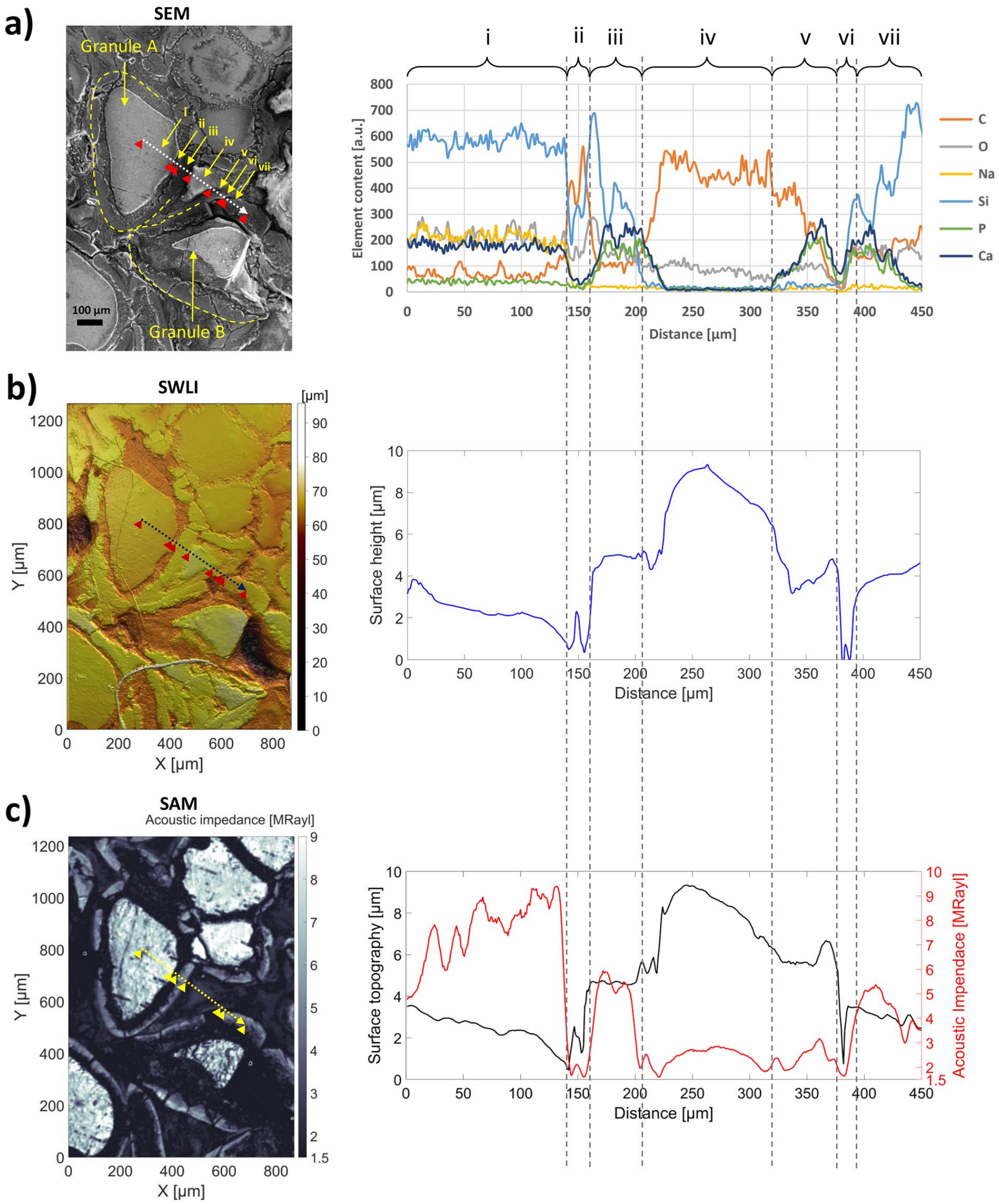

**Figure 1.** Bone growth measured with SEM–EDX (**a**), SWLI (**b**), and CESAM (**c**). (**a**) SEM image of BAG granules A and B (left) and EDX elemental analysis of the content along the indicated scan line (right). (**b**) SWLI image of the sample (left) and topography along the scan line (right). (**c**) CESAM acoustic impedance map of the sample (left), and acoustic impedance (red) and topography (black) along the scan line. Regions of interest (i–vii) related to stages of bone formation (glass granule, Si-layer, HA-layer, epoxy, non-mineralized bone tissue, HA-layer, Si-layer) are indicated in each figure and discussed in detail in corresponding paragraphs. The acoustic impedance (**c**, red line) along the scan line is well explained by the elemental analysis from SEM–EDX (**a**), and the topography maps from SWLI (**b**) and CESAM (**c**) are in good agreement. Thus, CESAM encapsulates the relevant information for bone growth estimation.

Thus, most of the different materials expected to be present along the scan line have significantly different acoustic impedances, allowing tissue/material identification: glass granules ($Z \approx 8$ MRayl) (Region (i)), bone formation on top of the HA-layer ($Z = 5.4 \pm 0.3$ MRayl) (Region (iii)), and Si-layer surrounding the glass granules $Z = 3.1 \pm 0.4$ MRayl. The non-mineralised bone tissue in Region (v) ($Z = 2.4 \pm 0.4$ MRayl) and the epoxy in Region (iv) ($Z = 2.5 \pm 0.3$ MRayl) have similar acoustic impedances, but the homogeneity of the epoxy makes it distinguishable from non-mineralised bone tissue.

**ROI determination from simultaneous acoustic impedance and topography maps.** As the CESAM provides both an acoustic impedance map and a topography map, it facilitates determining regions-of-interest (ROIs) related to bone formation with higher certainty and ease than with only SWLI or other topography-based techniques. To demonstrate this, three areas (Area 1–3) showing ambiguous features in the topography maps of both the SWLI (Fig. 2a) and CESAM (Fig. 2b) are highlighted in Fig. 2.

**Area 1.** Area 1 illustrates the difficulty in distinguishing borders between bone formation layers surrounding glass granules (A) and (B) from topography maps. From the acoustic impedance map (Fig. 2c), it is evident that both granules are surrounded by a bone formation layer (hard boundaries surrounding the glass granules, *cf.* Region (iii), Fig. 1) and the border between the layers is easily distinguishable. In both topography maps (SWLI, Fig. 2a, and CESAM, Fig. 2b), the exact border between the two boundary layers is imperceptible, despite the improved lateral resolution of SWLI compared to CESAM.

**Area 2.** In both topography maps (SWLI, Fig. 2a, and CESAM, Fig. 2b), Area 2 shows a flat feature similar to the two adjacent glass granules (to the left). This could indicate another glass granule. However, when examining the acoustic impedance map, one can determine that the two adjacent larger granules are glass (high acoustic impedance, *cf.* Region (i), Fig. 1), while the smaller feature is a different material. Based on the acoustic impedance value and the acoustic homogeneity of the smaller feature, one can conclude that it is epoxy (*cf.* Region (iv), Fig. 1).

**Area 3.** Area 3 constitutes an uneven region, whose interpretation from topography maps is elusive. From SWLI (Fig. 2a) or CESAM (Fig. 2b) topography maps, one can only conclude that this region is not a flat glass granule. The acoustic impedance map (Fig. 2c), on the other hand, provides valuable information: The edges of Area 3 comprise bone formation layers around glass granules (hard boundaries surrounding the glass granules, *cf.* Region (iii), Fig. 1), whereas the middle contains softer material (low acoustic impedance). The inhomogeneity of Area 3 further suggests that the material is not epoxy (*cf.* Area 2), leading to an interpretation that it could be connective tissue or non-mineralised bone.

The presented results show that not only does the CESAM acoustic impedance map correspond expectedly with SEM–EDX elemental analysis, but that the CESAM topography map agrees with the SWLI topography map as well. The CESAM topography map is accurate enough to display narrow notches (Region (ii) and (vi), Fig. 1)) that might confound the acoustic impedance values. Hence, CESAM provides an internal reference showing where acoustic impedance values should be treated carefully. Furthermore, utilizing information from both the acoustic impedance and topography maps, generated simultaneously by the CESAM, allows determining regions-of-interest related to bone formation around the BAG with greater confidence and ease (Fig. 2).

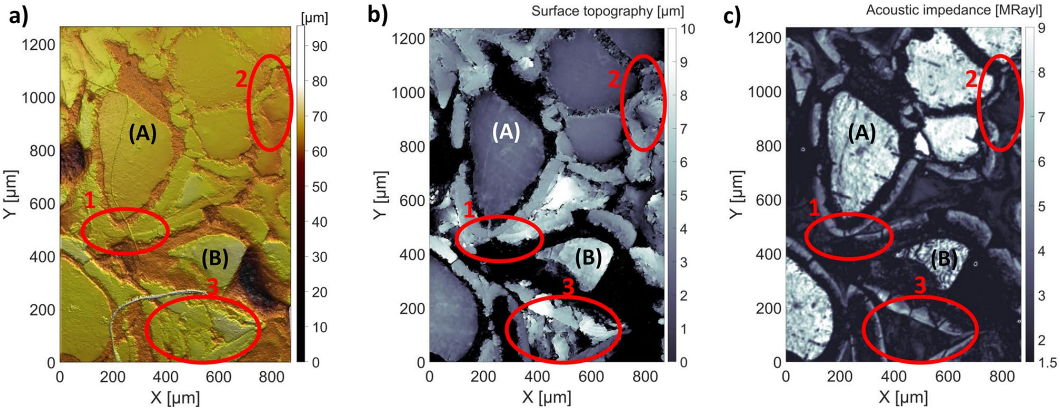

**Figure 2.** Comparison of (**a**) SWLI image, (**b**) CESAM topography map, and (**c**) CESAM acoustic impedance map to determine regions-of-interest (ROIs) related to bone formation. Three areas (Area 1–3), showing ambiguous features in the topography maps, are indicated in all images. The acoustic impedance information in these regions assists in determining ROIs. Glass granules (A) and (B) are indicated.

## Discussion

As the use of bone substitutes becomes more common, research into the bone formation encompassing them is needed. BAG-S53P4, with its osteoconductive, osteostimulative, angiogenetic[4,5], and antibacterial properties[6,7], is of particular interest. However, as the HA-layer forming on the glass granules is indistinguishable from bone mineral in X-rays, the remodelling process is difficult to assess. The proposed SAM method provides a tool for estimating bone formation ex vivo, due to the mechanical contrast between glass granules, HA-layer and forming bone tissue, which is visible in the acoustic impedance map. While SAM can only be used ex vivo for this purpose, it still enables research into the bone formation process on a micron scale in animal models, which can provide important information. Ideally, the information obtained by SAM ex vivo measurements could be used to construct models of bone healing for BAG bone substitutes in the future. These might enable designing in vivo acoustic imaging methods for bone growth evaluation.

SAM, especially coded-excitation SAM (CESAM) as was used here, is capable of fast imaging of quite large areas (a few mm$^2$) with a lateral resolution of a few microns[26,34,35]. In most SAM applications, several C-scans (acoustic impedance/topography of a 2D plane) are imaged and then averaged. With CESAM, the imaging speed is significantly higher, as the increased SNR reduces or even eliminates the need for averaging[26]. Another benefit of SAM is that it concurrently provides both an acoustic impedance and a topography map. Having both maps, from a single instrument, of large areas and with high resolution, assists in evaluating regions-of-interest in the samples (Fig. 2). While SAM has been used to image bone previously (e.g.[12,13,18–22,38]), this study is the first to study bone formation with BAG substitutes using a single-C-scan approach and is a continuation of our work described in[34]—the first SAM study of bone formation with BAG substitutes. Furthermore, as the CESAM used in this study improves SNR, it abets imaging of samples with low mechanical contrast[26].

The advantage of SAM over topography-based techniques is the obtained mechanical contrast from the acoustic impedance map. However, SAM-obtained acoustic impedance values depend on several factors, e.g. tilt, scattering, and frequency. The frequency and focusing of the transducer affect the lateral and axial size of the focus, which affects the reflected echoes. The impact of these effects, their minimisation, and comparison of our impedance values to those presented in the literature are discussed in the following paragraphs.

In this study, a single C-scan of a rectangular area of the sample surface was performed with CESAM. Normal incidence was assumed between the transducer axis and sample surface. This assumption enables straight-forward acoustic impedance estimation from amplitude changes in the reflected echoes caused by different materials present in the sample. However, a tilted surface can deflect part of the reflected acoustic energy past the transducer, causing a drop in amplitude. To ensure that the sample surface was properly aligned to the focal plane of the transducer, a series of B-scans was performed and the sample angle subsequently adjusted with a goniometer. A B-scan shows the Time-of-Flight along one line across the surface. Tilt was removed by ensuring the B-scans in both lateral directions, over long scan lines, showed a straight line. As can be seen from the topography along the line in Fig. 1c, the surface is uneven, but there are flat sections (Region (i), (iii) and (vii)), which on average show no tilt. Also, a tilted sample would show that one edge of the CESAM topography map (Fig. 2b) would be elevated compared to the other. This would be seen in Fig. 2b as a lighter-to-darker colour gradient across the entire sample, which is absent. Figure 2b (SAM topography map) therefore shows that the sample was well aligned. Local height differences and tilts within the sample might also affect the reflected amplitude. However, the depth of focus of our ultrasound transducer was 49 µm (− 6 dB, in water), and therefore the ± 10 µm height variations were well within the focus. Narrow and steep notches, as in Region (ii) and (vi), Fig. 1c, might still cause artefacts in the recorded acoustic impedance. Such notches cause very local and large drops in amplitude (in only a few measurement points), as most of the acoustic pulse is reflected away from the transducer.

In addition to tilt and height variations, surface roughness causes scattering, which affects the reflected amplitude. Especially with high-frequency ultrasound, careful sample preparation and alignment is vital[19,20]. Therefore, for C-scans, the samples should be flat and well-polished. However, many interesting samples, especially biological ones, cannot be polished to a mirror finish. Polishing heterogeneous samples comprising varying mechanical properties presents problems, as softer materials are removed with less effort than stiff ones[19]. Hence, some surface roughness will always remain. To properly account for surface roughness, a multi-layer analysis technique should be used, where the sample is imaged in several planes along the axial direction[19,34]. This allows accounting for local inclinations[19] or reconstructing the image from several image planes, hence ensuring that each sample point has been imaged at least once in focus[34]. Neglecting scattering, as in our C-scan, tends to decrease the acoustic impedance estimate in regions and samples with high heterogeneity[19]. The benefit of using a single C-scan is that it is fast and requires less post-processing than the aforementioned techniques. In Hyvönen et al.[34], our CESAM was used to image both fixed and non-fixed leporine femoral BAG samples in several layers, because the height differences across the samples were in excess of 100 µm, i.e. much larger than the depth of focus. For studying the bone formation process around a BAG-implant, using a single C-scan with our CESAM seems sufficient, as the image contrast in both acoustic impedance and topography maps of the single- and multilayer approaches are comparable[34]. A single C-scan with CESAM provides enough contrast to discern areas of different mechanical properties and areas of interest, as shown in Fig. 1 and Fig. 2.

A higher frequency of SAM produces a tighter focus, thereby improving lateral resolution. Raum et al. 2004[20] demonstrated that a lower frequency (25 MHz) SAM produced lower impedance values of human femoral cortical bone (e.g., 20-year-old female, $Z = 7.5 \pm 0.2$ MRayl), than those recorded with a 50 MHz and a 100 MHz SAM (20-year-old female, $Z = 8.1 \pm 0.3$ MRayl and $Z = 8.4 \pm 0.3$ MRayl, respectively). The large focal width of the 25 MHz SAM (150 µm) made it impossible to separate the Haversian canals (typical width 45–65 µm[13]) from the bone matrix, causing averaging and apparent lowering of the acoustic impedance, dependent on number, size, distribution, and content of the canals. On the other hand, when high-frequency SAM (900 MHz) is used, there are other effects that cause lower apparent impedance values[18,19]. While the tight focus of a high-frequency

SAM improves resolution, scattering caused by surface roughness and local inclinations has an ever-larger impact on the acoustic impedance estimation. In Raum et al. 2003[19], this effect was studied using high-frequency SAM (900 MHz) of proximal cortical bone from human femora. Three methods were compared: (1) ignoring inclination, i.e. assuming normal incidence, (2) using a mask removing points with > 10° local inclination, and (3) extrapolation from angular-dependence plots. These methods produced average acoustic impedances of osteons Z = 3.9 MRayl, Z = 4.4 MRayl, and Z = 5.10 MRayl, respectively. The authors concluded that neglecting local inclination and surface roughness tends to decrease acoustic impedance estimates, especially with high-frequency SAM. In this study, our CESAM was used with a 256 MHz centre-frequency transducer and coded excitation (linear frequency-modulated chirp, 130–370 MHz, with a Gaussian envelope). This centre frequency presents a compromise between sufficient lateral resolution (5.9 µm) and a depth of focus (49 µm) larger than twice the height variation of the sample. This depth of focus alleviates scattering effects to some degree. The linear chirp concentrates energy into the centre of the band, thus providing high SNR[26]. In conventional SAM, short US bursts are used. Shorter bursts improve axial resolution, while simultaneously reducing the acoustic energy of the back-reflected echo. This causes a trade-off between resolution of the topography map and SNR of the acoustic impedance map. Meriläinen et al.[26] compared different chirps and a conventional 6-cycle short burst (with comparable bandwidth) with our CESAM on a USAF 1951 resolution sample. Using the 130–370 MHz linear chirp improved both the axial resolution of the topography map (27% decrease in pulse length) and the SNR of the acoustic impedance map (16 dB increase compared to 6-cycle burst)[26].

As described in the previous paragraphs, acoustic impedance estimation depends on several factors. Thus, a comparison of our impedance values to those found in the literature is necessary. The acoustic impedances related to bone formation in Fig. 1c, as measured with our 256 MHz SAM, were $Z = 5.4 \pm 0.3$ MRayl and $Z = 4.9 \pm 0.3$ MRayl for the bone mineral on the HA-layer forming around the BAG granules in Regions (iii) and (vi), and $Z = 2.4 \pm 0.4$ MRayl for the probable non-mineralized bone tissue in Region (v). The acoustic impedances for the, at least partly, mineralised bone in our leporine femoral epicondyle are similar to those measured by Schulz et al. for newly formed bone tissue in leporine femoral condyles (averages in the range $Z = 4.2$–$6.9$ MRayl)[39]. Our values are also similar to average acoustic impedances of osteons in human femoral cortical bone measured with 900 MHz SAM[19]. Raum et al. 2003 measured $Z = 5.10 \pm 0.05$ MRayl, when compensating for scattering by extrapolation from angular-dependence plots[19]. However, the acoustic impedances of femoral cortical bone in[19] are low compared to other studies, probably due to underestimation of tilt and hence impedances, when using high-frequency SAM[19]. As mentioned, Raum et al. 2004[20] demonstrated how 25 MHz SAM produced lower impedance values than the 50 and 100 MHz SAM, but even with 25 MHz SAM, the acoustic impedance of a 76-year-old female (with the lowest acoustic impedance of the study) was $Z = 7.2 \pm 0.2$ MRayl. A study of human cortical bone in radii using 200 MHz SAM also produced higher impedance values, in the range 7.2–9.3 MRayl[12]. However, as the bone tissue in our study is from a leporine femoral epicondyle, consisting of trabecular bone, and furthermore is only in the process of bone formation, it is reasonable that we obtain lower impedances. Acoustic impedances of human trabecular bone measured with SAM are in the range $Z = 6.2 \pm 0.6$ MRayl (50 MHz, calcanei)[38] and $Z = 6.1 \pm 0.6$ MRayl (100 MHz, femoral neck)[21], when samples are embedded in poly(methyl methacrylate). Fresh trabecular bone samples have impedances as low as $Z = 3.5 \pm 0.3$ MRayl to $Z = 3.7 \pm 0.5$ MRayl, when polished with grit P1000 and P4000 sandpaper, respectively[21]. Our sample was not fresh, but had first been stored in formalin at + 4 °C prior to embedding in epoxy, polished with P4000 sandpaper, and lastly dried in a vacuum oven (40 °C) for four weeks. However, if the measured bone tissue is not yet mineralised, the acoustic impedance might even resemble that of cartilage. Cartilage measured in human tibia with 50 MHz SAM had an acoustic impedance of $Z = 2.12 \pm 0.02$ MRayl[22]. Hence, our obtained acoustic impedances of non-mineralised and partly mineralised bone (from $Z = 2.4 \pm 0.4$ MRayl to $Z = 5.4 \pm 0.3$ MRayl and $Z = 4.9 \pm 0.3$ MRayl) are in reasonable agreement with the literature.

The main purpose of this proof-of-concept study was to determine the feasibility of the CESAM single-C-scan approach for studying BAG samples, i.e., to validate the acoustic impedance map against SEM–EDX and the topography map against the SWLI map. Despite the difficulty in obtaining reliable absolute acoustic impedance values, the CESAM produced an acoustic impedance map with enough mechanical contrast to distinguish between different tissues, the surrounding epoxy and the glass granules. Identifying ROIs was further aided by the simultaneously measured topography map. Future study directions would be to investigate the bone formation process at different stages of healing. This could also entail a statistical analysis of the presence of different tissue types in the samples and an estimate for uncertainties in acoustic impedance values based on the local flatness of the topography map. Another interesting line of inquiry would be to image fresh samples. For example Ojanen et al.[21] imaged fresh bone samples, and the ability to image wet leporine BAG samples has already been demonstrated with our CESAM[34]. As our SAM uses coded excitation, it would be interesting to see if the increased SNR and axial resolution could reduce the need for sample polishing, especially if combined with imaging of multiple focal layers.

## Conclusions

We established a method for investigating the bone healing process around BAG implants ex vivo. While X-rays cannot distinguish BAG from the forming bone, coded-excitation SAM produces sufficient mechanical contrast to differentiate between different bone tissue stages, BAG granules, and the surrounding epoxy. The acoustic impedance map of SAM was compared against SEM–EDX and the topography map against SWLI. SAM produces both acoustic impedance and topography maps simultaneously, which simplifies determining regions-of-interest relating to bone formation. CESAM, therefore, constitutes a promising stand-alone tool for investigating bone remodelling around BAG ex vivo.

## Materials and methods

**Bioactive glass.** The BAG implants were manufactured as described in[40,41]. BAG-S53P4 (in wt.%: 53% $SiO_2$, 23% NaO, 20% CaO and 4% $P_2O_5$) was melted from analytical reagents ($Na_2CO_3$, $CaCO_3$ and $CaHPO_4 \times 2H_2O$, Belgian quartz sand) at 1360 °C for 3 h in a platinum crucible. To achieve homogeneous BAG, the glass was melted twice. The melt was cast as a block in a graphite mould, then annealed for 4 h at 520 °C and finally cooled overnight in the annealing furnace. The BAG block was crushed and sieved into 300–500 µm granules. The granules were sintered in a graphite mould in nitrogen atmosphere at 720 °C for 90 min to cylinder-shaped porous scaffolds of 5 mm × 15 mm size (diameter x height).

**Bone sample.** A direct lateral approach to the knee and exposure of the femoral lateral epicondyle was performed under aseptic conditions on a skeletally mature rabbit (NZW, Harlan laboratories) under general anaesthesia (medetomidine hydrochloride s.c. + ketamine hydrochloride s.c.). A horizontal bone defect of 6 mm was drilled without penetrating the medial cortex. The defect was filled with the 5 mm × 15 mm (diameter x height) scaffold of BAG-S53P4. Cefuroxime, buprenorphine, and carprofen were given postoperatively for 3 days for infection prophylaxis and pain relief. The animal was euthanized at 8 weeks post treatment with an overdose of pentobarbital. The distal part of the femur was cut and stripped from soft tissues and stored in formalin at + 4 °C. The Animal Experimental Board of Finland approved the study (ESAVI/440/04.10.07/2014) and the laboratory animal care guidelines of the University of Helsinki, the ARRIVE guidelines, and the Directive 2010/63/EU of the European Parliament and the Council of the European Union were strictly followed in all aspects of the project.

The bone sample was prepared as described in[41]. The sample was first moulded in epoxy and then ground in ethanol in the axial plane to the centre of the scaffold with increasingly fine sandpaper, lastly with P4000 sandpaper. The sample was subsequently dried in a vacuum oven (40 °C) for four weeks.

**Scanning acoustic microscope.** A custom-built CESAM[26] was used to characterize the sample (Fig. 3a) (transducer centre frequency 256 MHz, lateral width of focus 5.9 µm, depth of focus 49 µm, working distance 577 µm, − 6 dB bandwidth: 144–368 MHz). The transducer was translated horizontally using two orthogonally aligned translation stages (MLS203-1, controller BBD202, Thorlabs, New Jersey, USA) with 50 nm encoder resolution. The transducer was excited with a linear FM chirp signal, 130–370 MHz, with a Gaussian envelope. The chirp was selected based on[26] for improved SNR and axial resolution. The ultrasonic echo was received with the same transducer, amplified by a low-noise pre-amplifier (ZFL-1000LN+, Mini Circuits, New York, USA) and recorded with a PCIe digital oscilloscope (M4i.2233-x8, 2.5 GS/s Spectrum Instrumentation GmbH, Grosshansdorf, Germany). The scanned area was 0.88 mm × 1.26 mm, and 1 µm stepping was used. Imaging was performed in water immersion.

The acoustic reflections from the top surface of the sample provided the Time-of-Flights producing the topography map. Simultaneously, the amplitude changes of the reflected echoes provided the elastic contrast of the sample comprising both bone and BAG. At each scanned point, the amplitude of the reflected echo depends on the acoustic impedance mismatch at the water-sample interface. To obtain the acoustic impedance of the leporine

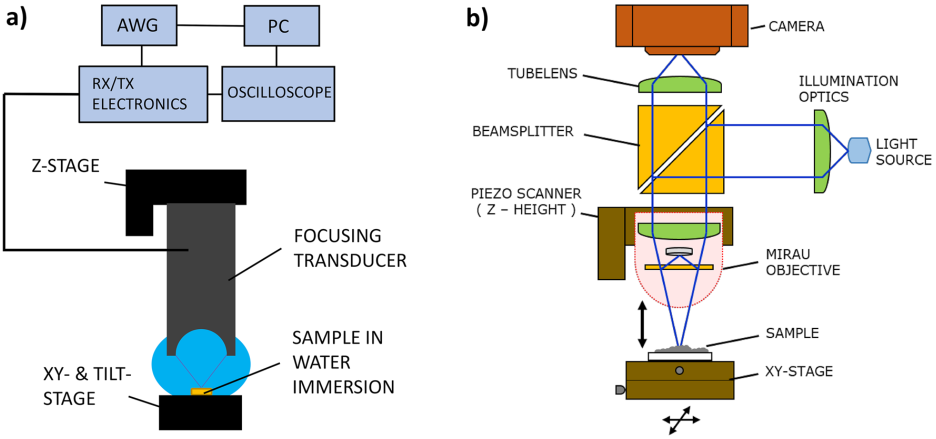

**Figure 3.** Schematics of (**a**) CESAM and (**b**) SWLI. (**a**) The focused transducer transmits a frequency-modulated coded signal (linear chirp, 130–370 MHz), which is reflected from the sample surface, recorded with the same transducer and post-processed. Both topography and acoustic impedance maps are obtained from one scan. The sample is scanned in the XY-plane in water immersion. (**b**) The light is divided within the Mirau-type objective to two interfering optical paths: scanning and fixed reference. The resulting interference images are recorded by a camera as a function of piezo-controlled objective-to-sample distance, which are used to calculate the topographic map of the sample.

bone sample, the acoustic amplitude was calibrated using a calibration method described in[19]. All samples were carefully aligned to allow assuming normal incidence of the acoustic pulse at each scanned point. At normal incidence, the reflection coefficient of the acoustic pressure, i.e., the ratio of the reflected pressure amplitude to the transmitted pressure amplitude, is:

$$R = \frac{Z_{sample} - Z_{water}}{Z_{sample} + Z_{water}} \tag{1}$$

where $Z_{water}$ and $Z_{sample}$ are the acoustic impedances of water (1.5 MRayl) and the sample (in each measured point). Three different calibration samples were used with the same transmission settings as with the leporine bone sample: acrylic (PMMA), silicon, and sapphire, with acoustic impedances $Z = 3.3$ MRayl, 22.0 MRayl and 41.7 MRayl, respectively. These calibration materials were selected because they have well-defined acoustic impedances and are available as flat samples. The surfaces of the aligned calibration samples were measured with different defocus distances and the focal amplitude (maximum amplitude) was used in the calibration calculations. The amplitudes of the reflected echoes from the bone sample were subsequently compared to the calibrated amplitudes to obtain the acoustic impedance map in Fig. 1c and Fig. 2c. Normal incidence was assumed within each measurement point also for the carefully aligned bone sample. As the focal width was 5.9 µm, this is a fair assumption, except in the vicinity of the narrow notches (Regions (ii) and (iv)).

**SWLI.** A custom-built SWLI (Fig. 3b)[31] was used to image the sample comprising both bone and BAG. The system is built on a Nikon side-illuminated microscope frame. A CMOS camera (Hamamatsu Orca-Flash 2.8, Hamamatsu, Japan) records images through a 10 × objective (10X Nikon CF IC Epi Plan DI, Tokyo, Japan) and through a 1 × tubelens (Nikon 200 mm, Tokyo, Japan). The vertical scanning of the sample was done by moving the objective inside a 100 µm range with a piezo actuator (PI Pifoc P-721-CDQ, Physik Instrumente (PI) GmbH & Co. KG, Karlsruhe, Germany). The sample was scanned in the lateral direction with a xy-translation stage (8MTF-102LS05, Standa Ltd, Vilnius, Lithuania) having a range of 10.2 cm and resolution of 0.31 µm. Spatial overlapping (30%) of sub-aperture scans was used. Data acquisition and surface detection was performed with custom-made software and surface stitching and 3D analysis was done with the commercial software MountainsMap (Digital Surf).

The sample was SWLI imaged with 17 sub-aperture scans and stitched together. As the SWLI is based on reflected light from the sample surface, it has measurement limitations with steep topographical slopes, which tend to scatter most of the light. This can be seen as increased measurement noise on the slopes of steep crevices/protrusions resulting in noisy surface detection in the steep edge areas.

**Scanning electron microscopy (SEM) and EDX elemental analysis.** SEM images were obtained with a scanning electron microscope (Coxem SEM EM-30 AX Plus) using an in-lens upper secondary electron (SE) detector (magnification 150x). The sample was coated with a 5 nm Pt/Pd layer. The acceleration voltage was 15.0 kV with a take-off angle of 25.8° and resolution 133 eV (at 5.89 keV Mn). The elemental analysis was performed with an Edax EDX detector of SDD type. The elemental analysis was applied along a 450 µm long scan-line (Fig. 1).

**Co-registration of images.** The same area of the sample was imaged with SWLI, SEM combined with EDX, and CESAM. The images were manually co-registered and the image contrast from SWLI (topography) and CESAM (acoustic impedance and topography) were obtained along the same scan line as the elemental analysis (Fig. 1). The SEM, SWLI, and SAM images are all based on different contrast methods, which is challenging for automated algorithm-based co-registration methods. Therefore, the co-registration was performed manually.

## Data availability

The data presented in this study are available on reasonable request from the corresponding author.

Received: 9 December 2022; Accepted: 13 April 2023

## References

1. Van der Stok, J., Van Lieshout, E. M., El-Massoudi, Y., Van Kralingen, G. H. & Patka, P. Bone substitutes in the Netherlands–A systematic literature review. *Acta Biomater.* **7**, 739–750 (2011).
2. Hench, L. L. & Paschall, H. Direct chemical bond of bioactive glass-ceramic materials to bone and muscle. *J. Biomed. Mater. Res.* **7**, 25–42 (1973).
3. Hench, L. L. The story of Bioglass®. *J. Mater. Sci. Mater. Med.* **17**, 967–978 (2006).
4. Detsch, R. *et al.* Increase in VEGF secretion from human fibroblast cells by bioactive glass S53P4 to stimulate angiogenesis in bone. *J. Biomed. Mater. Res. Part A* **102**, 4055–4061 (2014).
5. Day, R. M. Bioactive glass stimulates the secretion of angiogenic growth factors and angiogenesis in vitro. *Tissue Eng.* **11**, 768–777 (2005).
6. Zhang, D. *et al.* Antibacterial effects and dissolution behavior of six bioactive glasses. *J. Biomed. Mater. Res. Part A* **93**, 475–483 (2010).
7. Munukka, E. *et al.* Bactericidal effects of bioactive glasses on clinically important aerobic bacteria. *J. Mater. Sci. Mater. Med.* **19**, 27–32 (2008).
8. Bortolin, M. *et al.* Antibiofilm agents against MDR bacterial strains: Is bioactive glass BAG-S53P4 also effective?. *J. Antimicrob. Chemother.* **71**, 123–127 (2016).

9. Lindfors, N. C., Koski, I., Heikkilä, J. T., Mattila, K. & Aho, A. J. A prospective randomized 14-year follow-up study of bioactive glass and autogenous bone as bone graft substitutes in benign bone tumors. *J. Biomed. Mater. Res. Part B Appl. Biomater.* **94**, 157–164 (2010).
10. Lindfors, N. C., Heikkilä, J. T., Koski, I., Mattila, K. & Aho, A. J. Bioactive glass and autogenous bone as bone graft substitutes in benign bone tumors. *J. Biomed. Mater. Res. Part B Appl. Biomater.* **90**, 131–136 (2009).
11. Lindfors, N. *et al.* Bioactive glass S53P4 as bone graft substitute in treatment of osteomyelitis. *Bone* **47**, 212–218 (2010).
12. Raum, K., Cleveland, R. O., Peyrin, F. & Laugier, P. Derivation of elastic stiffness from site-matched mineral density and acoustic impedance maps. *Phys. Med. Biol.* **51**, 747–758 (2006).
13. Raum, K. *et al.* Site-matched assessment of structural and tissue properties of cortical bone using scanning acoustic microscopy and synchrotron radiation μCT. *Phys. Med. Biol.* **51**, 733–746 (2006).
14. Lemons, R. & Quate, C. F. Acoustic microscope—Scanning version. *Appl. Phys. Lett.* **24**, 163–165 (1974).
15. Cheeke, J. D. N. *Fundamentals and Applications of Ultrasonic Waves ch. 14.1* 1st edn, 297–303 (CRC Press, 2002).
16. Briggs, G. A. D. & Kolosov, O. V. *Acoustic Microscopy ch. 4.2, 52–57* 2nd edn. (Oxford University Press, 2010).
17. Briggs, G. A. D. & Kolosov, O. V. *Acoustic Microscopy* 2nd edn. (Oxford University Press, 2010).
18. Smitmans, L., Raum, K., Brandt, J. & Klemenz, A. Variations in the microstructural acousto-mechanical properties of cortical bone revealed by a quantitative acoustic microscopy study. In *2000 IEEE Ultrasonics Symposium. Proceedings. An International Symposium (Cat. No. 00CH37121)* 1379–1382 (2000).
19. Raum, K., Jenderka, K. V., Klemenz, A. & Brandt, J. Multilayer analysis: Quantitative scanning acoustic microscopy for tissue characterization at a microscopic scale. *IEEE Trans. Ultrason. Ferroelectr. Freq. Control* **50**, 507–516 (2003).
20. Raum, K., Reißhauer, J. & Brandt, J. Frequency and resolution dependence of the anisotropic impedance estimation in cortical bone using time-resolved scanning acoustic microscopy. *J. Biomed. Mater. Res. Part A* **71**, 430–438 (2004).
21. Ojanen, X. *et al.* Differences in acoustic impedance of fresh and embedded human trabecular bone samples—Scanning acoustic microscopy and numerical evaluation. *J. Acoust. Soc. Am.* **140**, 1931–1936 (2016).
22. Leicht, S. & Raum, K. Acoustic impedance changes in cartilage and subchondral bone due to primary arthrosis. *Ultrasonics* **48**, 613–620 (2008).
23. Hagiwara, Y. *et al.* Changes of articular cartilage after immobilization in a rat knee contracture model. *J. Orthop. Res.* **27**, 236–242 (2009).
24. Hagiwara, Y. *et al.* Comparison of articular cartilage images assessed by high-frequency ultrasound microscope and scanning acoustic microscope. *Int. Orthop.* **36**, 185–190 (2012).
25. Briggs, G. A. D. & Kolosov, O. V. *Acoustic Microscopy ch. 2.3, 22–25* 2nd edn. (Oxford University Press, 2010).
26. Meriläinen, A., Hyvönen, J., Salmi, A. & Hæggström, E. CESAM—Coded excitation scanning acoustic microscope. *Rev. Sci. Instrum.* **92**, 074901 (2021).
27. de Groot, P. Principles of interference microscopy for the measurement of surface topography. *Adv. Opt. Photonics* **7**, 1–65 (2015).
28. Wyant, J. C. White light interferometry. In *Proc. SPIE*, Vol. 4737 98–107 (2002).
29. Harasaki, A., Schmit, J. & Wyant, J. C. Improved vertical-scanning interferometry. *Appl. Opt.* **39**, 2107–2115 (2000).
30. Svanborg, L. M., Andersson, M. & Wennerberg, A. Surface characterization of commercial oral implants on the nanometer level. *J. Biomed. Mater. Res. Part B Appl. Biomater.* **92**, 462–469 (2010).
31. Sandler, N. *et al.* Rapid interferometric imaging of printed drug laden multilayer structures. *Sci. Rep.* **4**, 1–5 (2014).
32. Wyant, J. C. & Schmit, J. Large field of view, high spatial resolution, surface measurements. *Int. J. Mach. Tools Manuf.* **38**, 691–698 (1998).
33. Williams, C. S. & Becklund, O. A. *Introduction to the Optical Transfer Function* Vol. 112 (SPIE Press, 2002).
34. Hyvönen, J. *et al.* Three megapixel ultrasonic microscope imaging. In *2019 IEEE International Ultrasonics Symposium (IUS)* 1886–1889 (2019).
35. Hyvönen, J. *et al.* Coded acoustic microscopy to study wood mechanics and development. In *2019 IEEE International Ultrasonics Symposium (IUS)* 1989–1991 (2019).
36. Andersson, Ö. & Kangasniemi, I. Calcium phosphate formation at the surface of bioactive glass in vitro. *J. Biomed. Mater. Res.* **25**, 1019–1030 (1991).
37. Lindfors, N. & Aho, A. Granule size and composition of bioactive glasses affect osteoconduction in rabbit. *J. Mater. Sci. Mater. Med.* **14**, 365–372 (2003).
38. Leguerney, I. *et al.* Trabecular bone properties evaluated by scanning acoustic microscopy. In *Proceedings WCU* 295–298 (2003).
39. Schulz, M., Brandt, J., Raum, K. & Brehme, K. Quantitative assessment of bone properties during defect healing in an animal defect model by scanning acoustic microscopy. In *World Congress on Medical Physics and Biomedical Engineering* 289–292 (2009).
40. Björkenheim, R. *et al.* Polymer-coated bioactive glass S53P4 increases VEGF and TNF expression in an induced membrane model in vivo. *J. Mater. Sci.* **52**, 9055–9065 (2017).
41. Björkenheim, R. *et al.* Bone morphogenic protein expression and bone formation are induced by bioactive glass S53P4 scaffolds in vivo. *J. Biomed. Mater. Res. Part B Appl. Biomater.* **107**, 847–857 (2019).

## Acknowledgements

We gratefully acknowledge the financial support provided by a research grant from Helsinki University Hospital and the Finnish Medical Association.

## Author contributions

A.H. compiled the figures, analysed, and interpreted the results, and wrote the first draft of the manuscript. A.M. and J.H. constructed the scanning acoustic microscope and performed measurements with the device. J.H. participated in writing the manuscript. A.N., T.Y. and I.K. developed the scanning white light interferometer and performed measurements. K.S. performed the scanning electron microscopy imaging and the elemental analysis with Energy Dispersive X-ray Spectroscopy. H.J.N. contributed to the analysis and interpretation of the data and the writing of the manuscript. H.J.N., A.S., E.H. and N.C.L. conceived the original idea for the study. H.J.N, I.K., and A.S. supervised the instrumentation part of the study with E.H. being principal investigator. N.C.L. was the principal investigator of the biomaterial animal study and participated in writing the manuscript. R.B., G.S. and J.P. planned and performed the animal study. L.H. participated in the planning of the biomaterial animal study and in manufacturing the bioactive glass implant. All authors reviewed the manuscript.

## Competing interests

The authors declare no competing interests.

## Additional information

**Correspondence** and requests for materials should be addressed to A.H.

# Identifying Regions-of-Interest and Extracting Gold from PCBs Using MHz HIFU

Axi Holmström
*Electronics Research Lab.,*
*University of Helsinki*
Helsinki, Finland
axi.holmstrom@helsinki.fi

Tom Sillanpää
*Electronics Research Lab. and*
*Faculty of Pharmacy,*
*University of Helsinki*
Helsinki, Finland
tom.sillanpaa@helsinki.fi

Kenichiro Mizohata
*Department of Physics,*
*University of Helsinki*
Helsinki, Finland
kenichiro.mizohata@helsinki.fi

Ari Salmi
*Electronics Research Lab.,*
*University of Helsinki*
Helsinki, Finland
ari.salmi@helsinki.fi

Topi Pudas
*Electronics Research Lab.,*
*University of Helsinki*
Helsinki, Finland
topi.pudas@helsinki.fi

Petri Lassila
*Electronics Research Lab.,*
*University of Helsinki*
Helsinki, Finland
petri.j.lassila@helsinki.fi

Antti Kuronen
*Department of Physics,*
*University of Helsinki*
Helsinki, Finland
antti.kuronen@helsinki.fi

Edward Hæggström
*Electronics Research Lab.,*
*University of Helsinki*
Helsinki, Finland
edward.haeggstrom@helsinki.fi

Jere Hyvönen
*Electronics Research Lab.,*
*University of Helsinki*
Helsinki, Finland
jere.hyvonen@helsinki.fi

Joni Mäkinen
*Electronics Research Lab.,*
*University of Helsinki*
Helsinki, Finland
joni.mk.makinen@helsinki.fi

Tapio Kotiaho
*Faculty of Pharmacy and*
*Department of Chemistry,*
*University of Helsinki*
Helsinki, Finland
tapio.kotiaho@helsinki.fi

*Abstract* — **Increased digitalization and technological development raises the demand for rare and precious metals (RPM). Due to their rarity, mining RPMs from the earth is becoming increasingly difficult. Traditional urban mining methods to recover RPMs from printed circuit boards (PCB) need to separate the RPMs from non-metallic substances, e.g. plastic. This separation requires toxic substances and causes unwanted and toxic by-products and emissions. The ability to identify regions-of-interest on PCBs, i.e. the gold pads, and to extract RPMs from only the desired areas would reduce the need for toxic substances. In this study, a single 12 MHz high-intensity focused-ultrasound transducer was used to 1) image a PCB to locate the gold pads, and 2) to subsequently induce inertial cavitation to remove gold from three extraction areas on the selected gold pad. The sonication was performed in water without additional chemicals. Gold removal was verified by imaging the pad with a coded-excitation scanning acoustic microscope ($f_c = 375$ MHz). Average areas and volumes of the three extraction regions were $A = (12.2 \pm 0.5) \cdot 10^3$ µm$^2$ and $V = (18 \pm 2) \cdot 10^3$ µm$^3$, respectively. The total amount of removed gold and nickel (from beneath the gold plating) from all three extraction areas was estimated to $m_{Au,tot} = (570 \pm 20)$ ng and $m_{Ni,tot} = (440 \pm 30)$ ng. This study constitutes a first step towards more environmentally friendly, non-toxic urban mining of RPMs.**

***Keywords—Urban mining, cavitation erosion, MHz high-intensity focused ultrasound***

## I. INTRODUCTION

Increasing digitalization and technological development has benefitted humanity as increased prosperity, longevity, and health. However, this development has also increased the demand for electronic devices, which contain printed circuit boards (PCBs). Rare and precious metals (RPMs), for example gold, are used in PCBs because of their excellent physical and chemical properties, such as corrosion resistance, desirable thermoelectrical properties, and high conductivity. Thus, RPMs are still used despite their rarity, as they cannot easily be substituted for other materials. Due to their rarity, mining of RPMs from the earth is becoming increasingly difficult. For example, the total gold reserves have been estimated to approx. 244 000 t, of which 57 000 t are unexploited [1]. The global gold mine output in 2018 was 3310 t/year, while only 1178 t of gold was sourced from recycling [2]. At this pace, all gold would be mined within 20 years. To solve this, urban mining from electronic waste, e.g. discarded PCBs, is an expanding field [3, 4]. Electronic waste contains high concentrations of RPMs and could thus be used to enrich RPMs back into usable form [3, 4].

Traditional urban mining methods are faced with the task of separating RPMs from non-metallic materials found in PCBs, e.g. plastic casings of components. The separation process usually comprises three processing steps, as no single process is efficient enough as a stand-alone method: mechanical pre-processing, pyrometallurgy, and hydrometallurgy [3, 4]. The mechanical pre-processing constitutes e.g. manual PCB disassembly and/or PCB crushing [3]. In the pyrometallurgic step, the pre-processed PCBs are incinerated to separate the metals from other materials. This process causes harmful emissions and toxic waste [3]. In the final hydrometallurgic process, metals are leached. The leaching uses substances which cause toxic fumes or by themselves are highly toxic or caustic, for example cyanide and acids [3, 4]. Bioleaching, which utilizes microorganisms or their metabolites for leaching, is an emerging field that would be environmentally friendly [3, 4]. Unfortunately, leaching rates are low and the microorganisms are easily poisoned by toxic by-products, stopping the leaching process. Hence, bioleaching is currently only performed on a laboratory scale.

In this study, we propose a novel and environmentally friendly urban mining solution: Using high-intensity focused ultrasound (HIFU), in water, to first identify regions-of-interest (ROIs) on PCBs, i.e. locate the gold pads, and to

---

This work was funded by the Academy of Finland (grant 347459).

subsequently extract gold from the desired areas using HIFU-induced inertial cavitation. Identifying the gold pads and removing gold only from them eliminates the need for further separation of metals from non-metallic materials. HIFU-induced inertial cavitation can be applied in water, without any chemicals or toxins, and is a well-known material erosion phenomenon that has been utilized e.g. on aluminium [5, 6] and in lithotripsy to break kidney stones [7]. We used a 12 MHz custom-built HIFU transducer to obtain both imaging and material extraction capability. Material removal was quantified with a coded-excitation scanning acoustic microscope (CESAM) [8, 9].

## II. METHODS

### A. Experimental Setup and Sample

The HIFU setup is shown in Fig. 1. The 12 MHz HIFU-transducer contained a custom-built piezo bowl (F5265018, Meggitt A/S, Kvistgaard, Denmark) (bandwidth 2 MHz, element diameter 1.9 cm, focal distance 1.5 cm, focal width 140 µm). Signals were generated with an arbitrary waveform generator (FG31052 SERIES, Tektronix, Oregon, USA) and sent to a power amplifier (500A100A, Amplifier Research, Pennsylvania, USA, bandwidth 10 kHz–100 MHz) at either low (imaging) or high (material extraction) settings. Echoes were recorded with an oscilloscope (PicoScope 5442D, Pico Technology, Cambridgeshire, UK) through a 100x attenuating voltage probe (TT-HV250, TESTEC Elektronik GmbH, Hesse, Germany) and saved to a computer. A 3D translation stage (Techno Isel router table, Isel Germany AG, Hesse, Germany) was used to scan the sample during imaging. Both imaging and extraction was performed in reverse-osmosis purified water (RiOs Essential Water Purification Systems, Milli-Q, Hesse, Germany) that had been under vacuum for 20 min. This was done to remove contaminants and to control the concentration of dissolved gas, as both particulates and gas bubbles act as nucleation sites for cavitation.

The sample was an obsolete PCB containing gold pads (Fig. 2A). Gold pads comprise a copper base, coated by a 6 µm intermediate nickel layer and coated with gold. As the gold-layer thickness on gold pads varies depending on the manufacturing method, the gold layer was measured using Rutherford backscattering spectrometry ($^7$Li-beam, beam energy 5 MeV) to be (870 ± 20) nm.

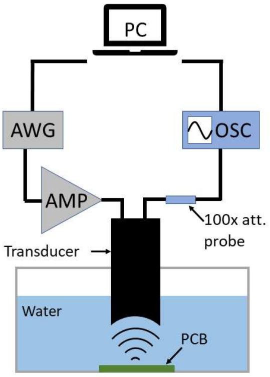

Fig. 1. Schematic of HIFU-setup. Signals are transmitted from the computer (PC) via an arbitrary waveform generator (AWG) to a power amplifier (AMP) at low (imaging) or high (extraction) settings and to a 12 MHz focused transducer. In imaging, sample echoes are recorded with the oscilloscope (OSC) as the sample is scanned with 3D translation stages.

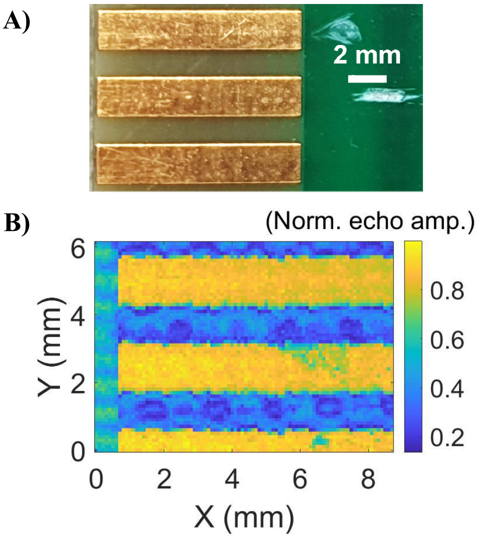

Fig. 2. PCB sample. A) Photograph of the gold pads. B) Amplitude map of the sample imaged with the HIFU-transducer.

### B. Identifying Regions-of-Interest

A 6 mm x 8 mm area of the gold pads was scanned with the HIFU-transducer ($f$ = 12 MHz, 20-cycle bursts, 100 µm step size). An amplitude map was constructed from the echoes (Fig. 2B), showing higher reflection amplitude from the gold pads, distinguishing them from the board.

### C. Gold Extraction

One gold pad was selected for gold extraction. Three separate extraction areas, 520 µm apart, were sonicated. Each area consisted of a 5 x 5 grid of sonication spots with 20 µm spacing (area 80 µm x 80 µm), each sonication was performed with constant acoustic parameters: $f$ = 12 MHz, 30 cycles/burst, 250k bursts, $PRF$ = 1 kHz, $P_{PPP}$ = 40 MPa). Extraction was quantified using a coded-excitation scanning acoustic microscope (CESAM) [8, 9] with a 375 MHz transducer (bandwidth 140 MHz, beam width 2.5 µm, scanning step size 1 µm). The Tx-signal was a 300–500 MHz linear chirp with 1 µs burst length (Gaussian envelope). The measured topography map was used to calculate the amount of removed material from each extraction area.

## III. RESULTS AND DISCUSSION

The topography map and depth profile of one extraction area is shown in Fig. 3 as an example. For each extraction area, a ROI-mask, containing only the areas of cavitation extraction (including small cavitation pits), was made manually. The surface zero-level was determined, and the depth profile was used to calculate the amount of removed gold and nickel. The average extraction areas, volumes, and amounts of removed gold and nickel were calculated to determine the repeatability of the extraction (average ± standard deviation): $A$ = $(12.2 \pm 0.5)\cdot 10^3$ µm$^2$,

© 2022 IEEE. Reprinted, with permission, from A. Holmström, T. Pudas, J. Hyvönen, T. Sillanpää, P. Lassila, J. Mäkinen, K. Mizohata, A. Kuronen, T. Kotiaho, A. Salmi, and E. Hæggström, “Identifying regions-of-interest and extracting gold from PCBs using MHz HIFU”, 2022 IEEE International Ultrasonics Symposium (IUS), Venice, Italy, 10-13 October 2022, doi: 10.1109/IUS54386.2022.9957863.

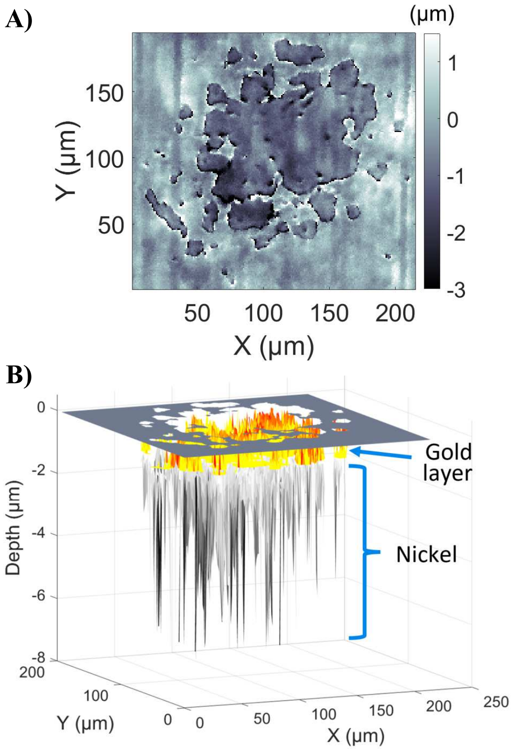

Fig. 3. CESAM topography map of one extraction area. A) Top view showing the shape of the cavitation extraction. B) Depth profile showing extraction depth into gold and nickel.

$V = (18 \pm 2)\cdot 10^3\ \mu\text{m}^3$, $m_{Au} = (190 \pm 20)$ ng and $m_{Ni} = (150 \pm 30)$ ng. The variation in volume was larger than that in area, because the bottoms of the extraction areas were uneven, *cf.* Fig. 3B. The uncertainty in removed gold and nickel masses are attributed to the uncertainty in the gold-layer thickness (± 20 nm). The standard deviation of the calculated masses and the uncertainty caused by variation in volume were orders of magnitude smaller than the contribution from the layer-thickness uncertainty. Finally, the total amount of removed material from all three extraction areas was calculated, which was $m_{Au,tot} = (570 \pm 20)$ ng and $m_{Ni,tot} = (440 \pm 30)$ ng.

The extracted material was not collected in this study. To collect the gold particles, the extracted particulates could be filtered from the water. Nickel is ferromagnetic and could thus easily be separated from gold. In the literature, one can find more complex methods for separating gold particles from complex water solutions, such as metal-organic-framework/polymer composites, which have been successfully used to collect 99 % of gold particles in river water [10].

Further work is needed to improve both the benefit-cost ratio and energy efficiency of this method. An estimate for the required removal work of this total amount of material was made from the cohesive energy of gold and nickel, which amounted to 4.4 mJ. The used electric energy was calculated from measured power being delivered to the transducer, which amounted to 3.8 kJ. Losses can occur in many parts of the process, for example as losses in the transducer, absorption in water, and bubble shielding [11] causing acoustic energy to be reflected rather than attributing to desired inertial cavitation. Though the energy efficiency is low, the benefit-cost ratio, i.e. the monetary value of the extracted gold divided by the cost of the used electricity, was 12 %. As such, the method is not yet cost effective, but this ratio is clearly higher than the energy efficiency, hinting that the method could be economically feasible with further developments. As seen in Fig. 3B, nickel was also removed superfluously. Only 16 % of the extraction area had pure gold removal, without any nickel. Optimizing the sonication parameters to only remove gold or using a different transducer-sample geometry (e.g. transducer at an angle, not perpendicular, possibly inducing a peeling effect) could improve this. Yet another possibility could be to use a lower centre frequency HIFU-transducer, which would result in a larger focal region and a lower cavitation threshold. The current 12 MHz transducer has a 140 µm focus, providing imaging capability, but the small focal region also restricts the area where extraction can occur. Imaging with a lower frequency transducer might be improved by using 2nd or 3rd harmonic imaging, thus achieving a reasonable trade-off between imaging and extraction capability.

## IV. CONCLUSION

Gold extraction from an obsolete PCB – from only desired regions-of-interest – was achieved in water (without added chemicals or toxins) using a single 12 MHz HIFU-transducer. This demonstrates a first step towards more environmentally friendly, non-toxic urban mining of rare and precious metals.

## REFERENCES

[1] United States Geological Survey. "How much gold has been found in the world?" https://www.usgs.gov/faqs/how-much-gold-has-been-found-world (accessed 09.09.2022).

[2] K. N. Sheaffer, "2018 Minerals Yearbook-Gold," United States Geological Survey, 2018. [Online]. Available: https://pubs.usgs.gov/myb/vol1/2018/myb1-2018-gold.pdf.

[3] M. Wang, Q. Tan, J. F. Chiang, and J. Li, "Recovery of rare and precious metals from urban mines—A review," Front Environ Sci Eng, vol. 11, no. 5, pp. 1-17, 2017.

[4] J. Cui and L. Zhang, "Metallurgical recovery of metals from electronic waste: A review," J. Hazard. Mater., vol. 158, no. 2-3, pp. 228-256, 2008.

[5] A. Karimi and J. Martin, "Cavitation erosion of materials," Int. Met. Rev., vol. 31, no. 1, pp. 1-26, 1986.

[6] W. Tomlinson and S. Matthews, "Cavitation erosion of aluminium alloys," J. Mater. Sci., vol. 29, no. 4, pp. 1101-1108, 1994.

[7] S. Yoshizawa, *et al.*, "High intensity focused ultrasound lithotripsy with cavitating microbubbles," Med Biol Eng Comput vol. 47, no. 8, pp. 851-860, 2009.

[8] A. Meriläinen, J. Hyvönen, A. Salmi, and E. Hæggström, "CESAM—Coded excitation scanning acoustic microscope," Rev. Sci. Instrum, vol. 92, no. 7, p. 074901, 2021.

[9] J. Hyvönen, *et al.*, "Three Megapixel Ultrasonic Microscope Imaging," IEEE International Ultrasonics Symposium (IUS), Glasgow, UK, 2019: IEEE, pp. 1886-1889.

[10] D. T. Sun, N. Gasilova, S. Yang, E. Oveisi, and W. L. Queen, "Rapid, selective extraction of trace amounts of gold from complex water mixtures with a metal–organic framework (MOF)/polymer composite," J. Am. Chem. Soc., vol. 140, no. 48, pp. 16697-16703, 2018.

[11] K. Maeda, A. D. Maxwell, T. Colonius, W. Kreider, and M. R. Bailey, "Energy shielding by cavitation bubble clouds in burst wave lithotripsy," J. Acoust. Soc., vol. 144, no. 5, pp. 2952-2961, 2018.

# Focused-Ultrasound-Induced Cavitation Removes Material in a Controlled Fashion

Jere Hyvönen[1], Axi Holmström[1], Topi Pudas[1], Tom Sillanpää[1,2], Petri Lassila[1], Joni Mäkinen[1], Antti Kuronen[3], Tapio Kotiaho[2,4],
Ari Salmi[1], Edward Hæggström[1]
[1] Electronics Research Lab., Dept. of Physics, University of Helsinki,, Helsinki, Finland
[2] Faculty of Pharmacy, University of Helsinki, Helsinki, Finland
[3] Dept. of Physics, University of Helsinki, Helsinki, Finland
[4] Dept. of Chemistry, University of Helsinki, Helsinki, Finland
Email: jere.hyvonen@helsinki.fi

***Abstract*—Most HIFU-induced cavitation applications use low frequencies (< 5 MHz), limiting the spatial precision of material erosion. Here, high-frequency (12 MHz) HIFU-induced cavitation was used to locally remove material from aluminium and thin film samples. Control over pit volume and surface area (pits with 20 - 200 µm diameter) was demonstrated by varying sonication parameters. Pit surface areas and volumes were quantified with a scanning acoustic microscope. Increasing the number of bursts increased the eroded volume but also caused a greater variation in pit area, owing to the stochasticity of inertial cavitation. Increasing the sonication amplitude increased the erosion area, as a larger area of the beam exceeded the local cavitation threshold. These results will be used to find suitable sonication parameters for localized HIFU surface-sampling.**

***Keywords— Cavitation erosion, MHz high-intensity focused ultrasound***

## I. INTRODUCTION

Ultrasound (US) has been used since the first half of the 20th century for medical and industrial applications. Low-intensity (< 1 W/cm²) applications include imaging and non-destructive testing and sensing [1], whereas high intensity (> 1 W/cm²) applications include ultrasonic cleaning [2], acoustic levitation [3] and sonochemistry [4]. Low intensity applications are based on measuring how the target or medium affects the sound, whereas high-intensity applications are usually based on energy transfer to the target either by heating- or cavitation-related phenomena. Focusing US enables high local energy densities and associated phenomena.

The erosion of different materials using HIFU-induced cavitation has been documented in previous studies. Aluminium is a commonly used metal to study cavitation erosion due to its high susceptibility to erosion [5, 6]. Another example of HIFU erosion is the breaking of kidney stones in lithotripsy. This has been done with frequencies at least as high as 4 MHz [7]. HIFU applications with higher frequencies have been demonstrated [8, 9], but they are often based on heating-related phenomena and seldom employ cavitation.

In this paper we demonstrate the use of 12 MHz HIFU-induced cavitation to remove material from solid surfaces. We characterized the eroded surfaces with a coded-excitation scanning acoustic microscope (CESAM) [10, 11]. We studied the effect of sonication parameters on cavitation erosion with two samples: flat aluminium surface and soft polymer thin film on glass.

## II. METHODS

Our setup (Fig. 1A) was built to drive a 12 MHz focusing bowl piezoceramic (F5265018, Meggitt A/S, Kvistgaard, Denmark). Device control and data storage were handled with a PC. An arbitrary waveform generator (AWG) (AFG31052 SERIES, Tektronix, Oregon, USA) was connected to a power amplifier (500A100A, Amplifier Research, Pennsylvania, USA), whose output was connected to the piezoceramic. An oscilloscope (PicoScope 5442D, Pico Technology, Cambridgeshire, UK) was used to record the signals from the piezo via a 100x attenuating probe (TT-HV250, TESTEC Elektronik GmbH, Hesse, Germany). A hydrophone (SN:PA11023, Precision Acoustics LTD, Dorchester, UK) was used to calibrate the transducer. Hydrophone signals were recorded from the hydrophone preamplifier. A microcontroller (Elegoo Uno R3, Elegoo, Guangdong (Shenzen), China) was used to control XYZ-translation stages and to trigger the AWG and oscilloscope.

We performed experiments on two different types of samples: polished aluminium plates (AW-5754) and marker ink (Art. 2836, Centropen) thin films on microscope slides (Fisherbrand 12373118, Fisher Scientific). All sonication experiments were done in reverse-osmosis purified water, which was degassed in a vacuum before the experiments to provide comparable gas contents for each experiment.

We performed a voltage-to-pressure amplitude calibration of our transducer. This was done at the focus for small amplitudes (1-10 MPa) and 1 mm away from the focus for high amplitudes (> 10 MPa) to prevent cavitation damage to the hydrophone. Linear extrapolation was performed for the high amplitude signals at the focus. Because we calibrated high amplitudes out of focus, we cannot measure saturation of the negative amplitudes, thus positive amplitude, which saturates less, is reported.

Before applying HIFU we focused the transducer onto the surface of the sample by using coded excitation pulse-echo measurements and tracking focal echo time-of-flight (ToF). We used a 20 µs long 11 MHz to 13 MHz linear chirp with a gaussian envelope. Coded excitation provided sufficient signal-to-noise-ratio (SNR) and ToF-resolution despite the transducer being narrowband. Precise focusing was important, since sonicating out of focus decreases the pressure amplitude at the sample surface significantly. We studied the effect of total acoustic energy on the erosion of

---

This work was funded by the Academy of Finland (grant 349200).

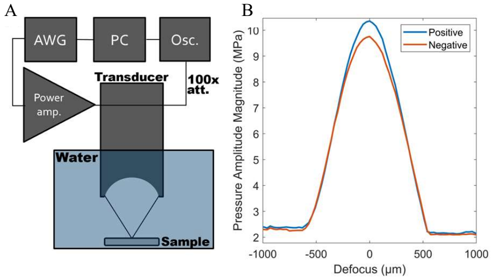

Fig. 1. Setup and calibration. A) A block diagram of the actuation setup. B) Hydrophone measurements to study the focal depth of the transducer.

aluminium by varying the number of sonication bursts. We sonicated 15 different spots with burst counts from 1000 to 15000 with steps of 1000 bursts, which were observed to produce detectable erosion in preliminary tests. The focal positive-pressure amplitude was kept constant at 24 MPa and the acoustic cycles per burst at 80. The experiment was repeated 5 times. The erosion pits were imaged with a CESAM (300 - 500 MHz, lateral imaging resolution of 3 µm) [10,11] and the resulting surface topography maps were analyzed to determine the area and volume of each pit.

To study HIFU-induced cavitation erosion of thin films (marker ink on a microscope glass), we sonicated the surface with 12 different positive amplitude values: from 9 to 21 MPa with 1 MPa steps. The number of acoustic cycles was kept constant at 80 and burst count was 5000, which were chosen based on preliminary tests. The resulting erosion pits were imaged with the CESAM and the resulting topography maps were analyzed to determine the areas and volumes of the pits.

## III. RESULTS AND DISCUSSION

Fig. 2 shows the average erosion pit volumes in aluminium for each burst count from 5 repeated experiments. The error bars are the standard errors of the means. The erosion pit volume increases as the burst count increases, which can be attributed to a corresponding increase in total acoustic energy. With increasing burst count, the deviation of eroded volumes between repeated experiments also increases. This trend is the result of the stochastic nature of cavitation; increasing the burst count causes irregular erosion of the pit edges. To achieve full erosion (all material removed inside the beam), an even higher number of bursts would be needed. Using longer bursts (more acoustic cycles per burst) might reduce this variation, as it would increase the probability of producing inertial cavitation during the burst. However, using too long bursts might result in excessive bubble formation (bubble shielding [12]), which could impede energy propagation to the sample surface due to scattering.

Fig 3. shows a CESAM topography image of a single erosion pit on an aluminium surface sonicated with 5000 bursts, each comprising 80 cycles with a 24 MPa positive pressure amplitude. With these parameters the HIFU produces relatively small erosion pits in the center of the focal region of the acoustic beam. In this case, the pit width is 20 µm, corresponding to 1/6 of the acoustic wavelength.

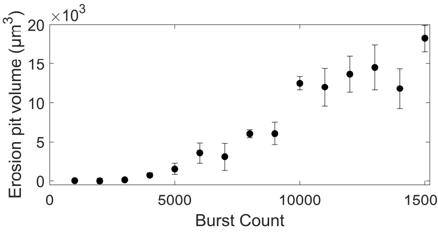

Fig. 2. The erosion pit volume was extracted from CESAM surface topography images. Error bars are the standard errors of the means of 5 experiments.

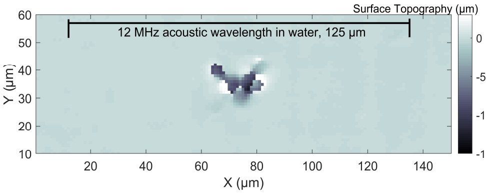

Fig. 3. CESAM image of an erosion pit on an aluminum surface sonicated with pressure amplitude of 24 MPa, burst count = 5000 and cycle count = 80. The width of the center pit is approx. 20 µm, i.e. 1/6 wavelength.

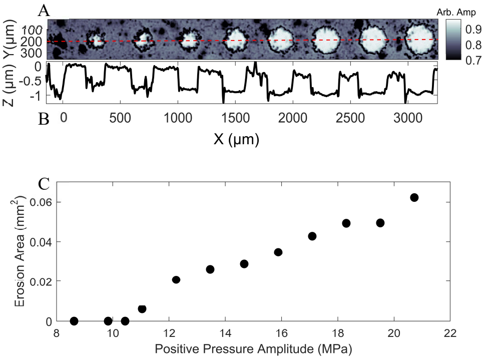

Fig. 4. A) CESAM image of the thin film sample post HIFU experiments. Acoustic pressure amplitude of the sonicating beam is increasing towards the right. B) A plot of the surface topography values along the dashed red line in A). C) Erosion areas of A) as a function of pressure amplitude of the actuating ultrasound.

Fig. 4A&B show a CESAM amplitude map and the surface topography along the red dashed line of the thin film sample post sonication. The three lowest amplitude sonications were excluded from these images since they showed no visible erosion in the sample. The acoustic microscope measures high amplitude values when the reflecting surface is flat and/or has a high reflection coefficient. In the areas where the thin film material has been removed and the glass underneath is revealed, the image shows high amplitude values. This is confirmed by the topography map measured with the same device (Fig. 4B). The diameter of the sonication pits increased with increasing excitation amplitude. This can be attributed to a widening of the active focal beam; a larger part of the focal area surpasses the pressure threshold required for initiating cavitation [13,14].

Fig. 4C shows the area of the erosion pits on the thin film sample shown in Fig. 4A. The three lowest excitation amplitude sonications produced no detectable erosion, but after 11 MPa a clear trend of erosion area increase is visible.

The results show that material removal by cavitation erosion can be controlled by adjusting the parameters affecting the acoustic pressure and total energy. We will use these results in our future research to find suitable sonication values for example to minimize erosion area in surface sampling. To increase the resolution of the material removal (smaller cavitation pits), it is probably necessary to increase the sonication frequency and to use a lens with higher numerical aperture. This comes with limitations of piezo disks getting thinner at high frequencies (less voltage tolerance) and cavitation threshold increasing with frequency.

## IV. CONCLUSIONS

We demonstrated the use of HIFU-induced cavitation erosion for controlled material removal in two different samples.

## REFERENCES

[1] D. Ensminger and L. J. Bond, Ultrasonics: Fundamentals, Technologies, and Applications, 3rd ed. Boca Raton: CRC Press, 2014.

[2] T. J. Mason, “Ultrasonic cleaning: An historical perspective,” Ultrason Sonochem, vol. 29, pp. 519–523, Mar. 2016.

[3] M. A. B. Andrade, N. Pérez, and J. C. Adamowski, “Review of Progress in Acoustic Levitation,” Braz J Phys, vol. 48, no. 2, pp. 190–213, Apr. 2018.

[4] N. Pokhrel, P. K. Vabbina, and N. Pala, “Sonochemistry: Science and Engineering,” Ultrason Sonochem, vol. 29, pp. 104–128, Mar. 2016.

[5] A. Karimi and J. L. Martin, “Cavitation erosion of materials,” Int. Met. Rev., vol. 31, no. 1, pp. 1–26, Jan. 1986.

[6] W. J. Tomlinson and S. J. Matthews, “Cavitation erosion of aluminium alloys,” J. Mater. Sci., vol. 29, no. 4, pp. 1101–1108, Feb. 1994.

[7] S. Yoshizawa, T. Ikeda, A. Ito, R. Ota, S. Takagi, and Y. Matsumoto, “High intensity focused ultrasound lithotripsy with cavitating microbubbles,” Med. Biol. Eng. Comput., vol. 47, no. 8, pp. 851–860, Aug. 2009.

[8] T. Bove, T. Zawada, J. Serup, A. Jessen, and M. Poli, “High-frequency (20-MHz) high-intensity focused ultrasound (HIFU) system for dermal intervention: Preclinical evaluation in skin equivalents,” Skin Res Technol, vol. 25, no. 2, pp. 217–228, Mar. 2019.

[9] K. D. Evans, B. Weiss, and M. Knopp, “High-Intensity Focused Ultrasound (HIFU) for Specific Therapeutic Treatments: A Literature Review,” J Diagn Med Sonogr, vol. 23, no. 6, pp. 319–327, Nov. 2007.

[10] A. Meriläinen, J. Hyvönen, A. Salmi, and E. Hæggström, “CESAM-Coded excitation scanning acoustic microscope,” Rev Sci Instrum, vol. 92, no. 7, p. 074901, Jul. 2021.

[11] J. Hyvönen, A. Meriläinen, A. Salmi, L. Hupa, N. Lindfors, and E. Hæggström, “Three Megapixel Ultrasonic Microscope Imaging,” IEEE Int. Ultrason. Symp. (IUS), pp. 1886–1889, Oct. 2019,

[12] K. Maeda, A. D. Maxwell, T. Colonius, W. Kreider, and M. R. Bailey, “Energy shielding by cavitation bubble clouds in burst wave lithotripsy,” J Acoust Soc Am, vol. 144, no. 5, pp. 2952–2961, Nov. 2018.

[13] E. Herbert, S. Balibar, and F. Caupin, “Cavitation pressure in water,” Phys. Rev. E, vol. 74, no. 4, p. 041603, Oct. 2006.

[14] A. Briggs and O. Kolosov, Acoustic Microscopy: Second Edition. OUP Oxford, 2010.

# Machining of Aluminium with MHz High-Intensity Focused Ultrasound

Topi Pudas
*Electronics Research Lab.,*
*University of Helsinki*
Helsinki, Finland
topi.pudas@helsinki.fi

Tom Sillanpää
*Electronics Research Lab. and*
*Faculty of Pharmacy,*
*University of Helsinki*
Helsinki, Finland
tom.sillanpaa@helsinki.fi

Antti Kuronen
*Department of Physics,*
*University of Helsinki*
Helsinki, Finland
antti.kuronen@helsinki.fi

Edward Hæggström
*Electronics Research Lab.,*
*University of Helsinki*
Helsinki, Finland
edward.haeggstrom@helsinki.fi

Jere Hyvönen
*Electronics Research Lab.,*
*University of Helsinki*
Helsinki, Finland
jere.hyvonen@helsinki.fi

Petri Lassila
*Electronics Research Lab.,*
*University of Helsinki*
Helsinki, Finland
petri.j.lassila@helsinki.fi

Tapio Kotiaho
*Faculty of Pharmacy and*
*Department of Chemistry,*
*University of Helsinki*
Helsinki, Finland
tapio.kotiaho@helsinki.fi

Axi Holmström
*Electronics Research Lab.,*
*University of Helsinki*
Helsinki, Finland
axi.holmstrom@helsinki.fi

Joni Mäkinen
*Electronics Research Lab.,*
*University of Helsinki*
Helsinki, Finland
joni.mk.makinen@helsinki.fi

Ari Salmi
*Electronics Research Lab.*
*University of Helsinki*
Helsinki, Finland
ari.salmi@helsinki.fi

***Abstract*—Cavitation-induced surface erosion has been studied for decades. High-intensity focused ultrasound (HIFU) enables localized erosion, with applications in many fields. However, no research has been published on machining solely with HIFU. Compared to existing micro-machining technologies, HIFU exhibits a unique set of benefits: inexpensive, minimal maintenance due to non-contact machining without slurry, mitigated chemical load, and monitoring capability. We demonstrate controlled surface machining of mirror-polished aluminium (AW-5754) using high-frequency (12 MHz) HIFU-induced cavitation erosion. Optimal sonication parameters (transducer-sample distance, amplitude, cycles per burst, number of bursts, and pulse repetition frequency) for stationary surface erosion were first identified experimentally. These parameters served as a basis for studying the effect of sonication parameters during on-the-fly erosion, i.e., engraving lines. The effect of stage translation velocity and the number of repeated passes across the engraved line were also studied. Subsequently, the acronym of our laboratory, "ETLA", was engraved, with a 500 µm letter height and an average line width of 53 µm.**

***Keywords— Micromachining, cavitation erosion, MHz high-intensity focused ultrasound***

## I. INTRODUCTION

Micrometer-scale machining has become an essential tool in many fields, e.g. medicine, biotechnology, electronics, and optics. Notable applications include drug delivery systems, chemical microreactors, and micro-electromechanical systems [1, 2, 3]. Various micrometer-scale machining technologies have been developed over the past decades, each with its own benefits and limitations.

Micro-cutting involves material removal by the mechanical grinding of a tool against a workpiece [4]. A related mechanical approach is ultrasonic machining, involving surface erosion by grinding a slurry of abrasive particles with a sonotrode against a workpiece surface [5]. Micro-electro-discharge machining removes material via an electric spark discharge between an oppositely charged tool and workpiece in liquid dielectric immersion [4]. Laser micro-machining uses high-power lasers to vaporize material from the workpiece, although prolonged treatment can risk thermal damage (e.g. microcracks, recast layers) to the workpiece [4]. Focused ion-beam milling employs a beam of high velocity ions to cause erosion [4]. Etching lithography utilizes a sequence of chemical treatments and light exposure to produce patterned surfaces [3]. Mechanical machining technologies, while relatively inexpensive, require tool maintenance due to wear [6]. Laser and ion-beam milling can produce µm and nm-scale features, respectively, but are expensive relative to alternative technologies. Etching lithography can also create nm-scale features, but it requires a chemically compatible workpiece material and involves multi-stage chemical processing.

Acoustic cavitation is a phenomenon where pressure waves cause the formation and oscillation of bubbles in liquids. Once the quantity and concentration of oscillating bubbles surpasses a critical point, bubbles form unstable gas clouds (cloud cavitation) [7]. With sufficient negative pressure amplitudes, the formed bubbles can collapse at speeds approaching the speed of sound in the liquid (inertial cavitation) [8]. In the proximity of a solid surface, the inertial collapse of a single bubble can result in an inrush of liquid towards the surface, i.e. microjetting (Fig. 1).

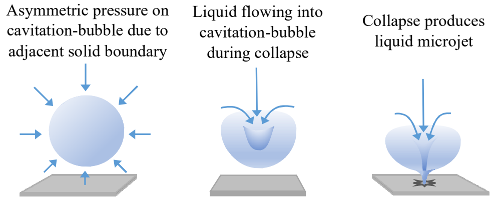

Fig. 1. Evolution of cavitation-bubble collapse near solid surface.

---

This work was funded by the Academy of Finland (grant 349200).

The microjet imparts a water hammer pressure on the surface. Successive collapses with sufficient water hammer pressures can cause material fatigue, resulting in localized erosion [9]. An increase in the magnitude of the acoustic rarefaction pressure (up to saturation) can therefore be expected to reduce the number of acoustic pulses required to initiate surface erosion. In practice, cavitation erosion is caused by mechanisms associated with the collective collapse of adjacent bubbles (cloud collapse). In addition to microjet impact, secondary rebound bubble implosion (the formation and subsequent collapse of bubbles generated from the primary collapse) and intermediate radical oxides (water-derived volatile gasses formed due to the high local pressures and temperatures) can play a significant role in producing erosion [10, 11].

High-intensity focused ultrasound (HIFU)-induced cavitation has been applied as a localized ablation method in a range of medical treatments, including non-invasive erosion of hard materials (lithotripsy), e.g. kidney stones [12], and soft tissues (histotripsy), e.g. scarring heart tissue to mitigate irregular electrical signals [13]. Non-focused ultrasound-induced cavitation has been widely researched as a means of surface modification, e.g. surface roughening and nanofoam formation [14, 11]. Rather surprisingly, no research has been published on machining solely with HIFU. HIFU-induced cavitation machining would introduce a unique set of benefits compared to existing machining technologies: inexpensive, minimal maintenance due to non-contact machining without slurry, mitigated chemical load due to water immersion operation, and feasibility for thermally sensitive materials.

Here we demonstrate controlled surface machining of aluminium (AW-5754) using high-frequency (12 MHz; 125 µm wavelength in water) with HIFU-induced cavitation erosion. The effect of sonication parameters on engraving linewidth, depth and line uniformity were studied. Finally, the acronym of our research laboratory, “ETLA”, was engraved. Engraved features were quantified with a coded-excitation scanning acoustic microscope (CESAM) [15].

## II. METHODS

### A. Experimental Setup

Fig. 2 illustrates the experimental setup. A custom-built transducer was prepared by epoxying (bisphenol-A/epichlorohydrin-based epoxy) a piezo bowl ($f_c = 12$ MHz, Ø = 1.9 cm, focal distance = 1.5 cm) to a 3D-printed support. The sonication target was an aluminium (AW-5754) plate, placed in a container filled with 400 ml of water. A mirror surface was prepared on the aluminium plate using a grinder-polisher (TegraPol-25, Stuers, Copenhagen, Denmark) with polishing paste (Aka-mono+, monocrystalline diamond suspensions, 15 µm & 6 µm). To control the concentration of contaminants and dissolved gas, the water was purified with a purification system (RiOs Essential Water Purification Systems, Milli-Q, Hesse, Germany) and kept in vacuum for 20 min.

The 12 MHz focused transducer was mounted onto a 3-axis motorized linear translation stage (NLS4 NEMA 17 MDrive, Newmark Systems Inc., California, USA). Actuation signals were produced with a waveform generator (AFG31052 SERIES, Tektronix, Oregon, USA). The actuating signal was amplified using an RF amplifier (500A100A, Amplifier Research, Pennsylvania, USA). A 100x attenuation probe (TT-HV250, TESTEC Elektronik GmbH, Hesse, Germany) was used with a digital oscilloscope (Picoscope 5442D, Pico Technology, Cambridgeshire, UK) to record the amplified signal for conversion to pressure values. Triggers to the waveform generator, oscilloscope and translation stages were provided by PC (via the translation stages).

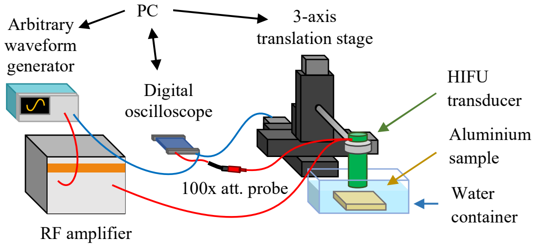

Fig. 2. Experimental setup. A HIFU transducer, mounted onto a 3-axis translation stage, is lowered into a water-filled container with the aluminium sample. Amplified signals are delivered from a waveform generator to the transducer. A digital oscilloscope monitors the signal received by the transducer and acoustic echoes returning from the aluminium surface. Signal triggers for both actuation and monitoring are delivered by PC via the translation stage. Red lines indicate actuation signal paths, blue lines trigger signal paths.

### B. Pressure Calibration

Conversion of measured voltage values produced by the amplifier to acoustic pressure values was based on calibration measurements. Pressure values were measured with a needle hydrophone (Ø = 75 µm, Precision Acoustics Ltd., Dorchester, UK) at the focal point at low amplitudes (< 90 V), and 1 mm from the focal point along the optical axis of the transducer at high (> 140 V) and low amplitudes. Based on the linear trend across high and low amplitudes in recorded off-focus pressures, a linear function for extrapolating focal amplitude values for high excitation voltages was used to convert excitation voltages to peak-positive-pressures.

### C. Sonication Parameter Study

Preliminary experiments were carried out to identify optimal sonication parameters for producing erosion at stationary sites. The resultant parameters were: transducer-sample distance of 15.24 mm, peak-positive-pressure amplitudes of ~30 MPa, 50 cycles per burst, 10 000 bursts. Continuing from stationary sonication to sonication on-the-move (engraving), parameters were varied around these values.

Engraving was done by performing repeated passes over the target while sonicating. While keeping the total input energy constant, the effect of movement velocity, number of passes, pulse repetition frequency (PRF) and cycles per burst was studied. Two velocities of 50 µm/s and 500 µm/s were used to engrave 1 mm long lines, the first with 20 passes and the latter with 200 passes. PRF and burst cycles were varied together: 250 Hz and 100 cycles, 500 Hz and 50 cycles, 1 kHz and 25 cycles.

Next the effect of total input energy was studied by altering acoustic amplitude, cycles per burst, and the number of passes. Velocity and PRF were kept constant at 50 µm/s and 250 Hz. Peak-positive-pressure amplitudes were 26 MPa, 33 MPa, and 38 MPa. For each amplitude value, 9 engravings were performed with varying cycles per burst and passes: 50, 100, and 200 cycles, and 10, 20, and 30 passes.

Based on these experiments, 33 MPa, 200 cycles, 250 Hz PRF and 20 passes were selected to engrave the text "ETLA". The letters were 500 µm long, with 125 µm spacing between letters.

### D. *Coded-Excitation Scanning Acoustic Microscope*

The cavitation erosion of sonicated samples was imaged with a CESAM [15]. Measured surface topography maps enabled quantification of erosion depth and surface area profiles. The specific configuration and principles of operation of the microscope have been outlined by Hyvönen *et al.* [16] and Meriläinen *et al.* [15].

## III. RESULTS AND DISCUSSION

A SAM topography map of 1 mm long engraved lines produced with varying sonication parameters, while maintaining constant total energy input, is presented in Fig. 3. Lines produced with 20 passes at 50 µm/s translation velocity are slightly thicker than those produced with 200 passes at 500 µm/s (in order of increasing cycles: 51 µm vs. 45 µm, 51 µm vs. 45 µm, 53 µm vs. 50 µm). In contrast, the relative standard deviation of line width tends to be greater for lines produced with 200 passes (0.28 vs. 0.29, 0.27 vs. 0.35, 0.27 vs. 0.37). These slight variations could be attributed to differences in the spatial separation between consecutive acoustic pulses. At 50 µm/s and 250 Hz PRF the spatial separation between acoustic pulses along the engraved line is 200 nm, while at 500 µm/s and 250 Hz PRF the corresponding separation is 20 µm. Using standard equations from optics, the theoretical focal beam diameter (at full-width-half-maximum) of our transducer is 140 µm [17]. Evidently, a 20 µm spatial separation between acoustic pulses is significant relative to the focal beam diameter, while a 200 nm movement comprises virtually stationary sonications. Since the cavitation cloud is confined within the focal beam, a smaller translational step between consecutive sonications can be expected to improve the symmetry of bubble distribution within the subsequent cavitation cloud.

SAM topography maps of 1 mm long engraved lines produced with constant velocity and PRF, and varying amplitudes, cycles per burst and number of passes are shown in Fig. 4. A similar trend can be seen for all varied parameters: Increasing amplitude, cycles per burst or passes produces wider lines. This is to be expected, since all three parameters are proportional to the total acoustic energy input. All lines display a degree of nonuniformity, which can be attributed to the stochasticity of cloud cavitation caused by variations in environmental conditions, e.g., the number of bubbles, bubble distribution, and surface irregularities acting as bubble nucleation sites. All lines engraved with 50 cycles (top rows) display some degree of segmentation, excluding 33 MPa, 30 passes. This segmentation suggests that 50 cycles is insufficient to reliably onset inertial cavitation at the used amplitudes, i.e., the effective cavitation probability is inadequate for consistent engraving.

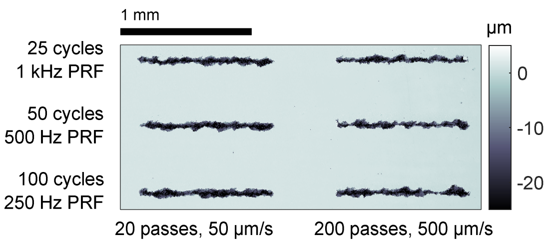

Fig. 3. SAM surface topography map of lines engraved on aluminium with 12 MHz HIFU-induced cavitation. A positive acoustic amplitude of 33 MPa was kept constant. Other sonication parameters were varied to maintain constant total energy input.

Evidently the most consistent erosion is produced with the highest amplitude. While a higher amplitude increases cavitation probability, it also causes a larger portion of the transducer focal zone to surpass the cavitation threshold pressure. To allow for sufficiently high cavitation probability with minimal expansion of the active focal zone, 33 MPa, 200 cycles and 20 passes were selected as the sonication parameters for subsequent engraving. The average line width and depth of the corresponding line in Fig. 4 were (43 ± 13) µm and (20 ± 8) µm, respectively, where uncertainties are standard deviations. Peripheral surface roughening was present around each engraved line (not visible in the SAM images due to color axis window), which can be attributed to infrequent cavitation events induced in the side lobes of the focal beam, and microjet-induced rebound cavitation events [18]. Intermediate gaseous radicals formed during cavitation also participate in the erosion of oxidizable metals by forming unstable oxides [19, 11]. However, the magnitude of this effect in comparison to microjets, i.e., the interplay of chemical and physical erosion mechanisms, is poorly understood in literature.

A SAM topography map of engraved letters "ETLA" is presented in Fig. 5. The average line width and depth were (53 ± 22) µm (corresponding to 0.42 λ) and (23 ± 10) µm, respectively, where uncertainties are expressed as standard deviations. Line width appears to increase near the

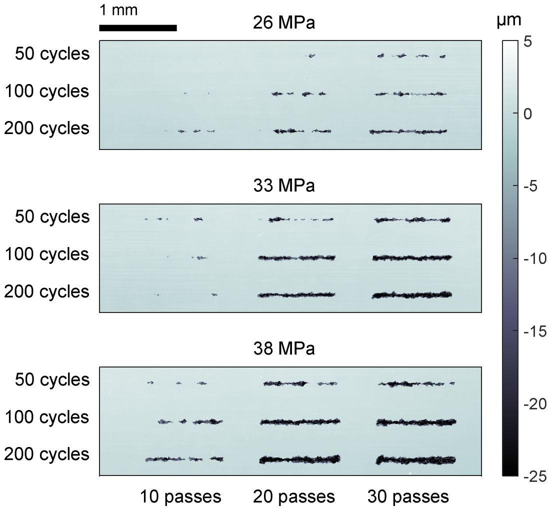

Fig. 4. SAM surface topography maps of lines engraved on aluminium with 12 MHz HIFU-induced cavitation. Translational velocity and PRF were kept constant at 50 µm/s and 250 Hz. Acoustic peak-positive-pressure, cycles per burst and number of repeated passes were varied.

© 2022 IEEE. Reprinted, with permission, from T. Pudas, J. Hyvönen, A. Holmström, T. Sillanpää, P. Lassila, J. Mäkinen, A. Kuronen, T. Kotiaho, A. Salmi, and E. Hæggström, "Machining of aluminium with MHz high-intensity focused ultrasound", 2022 IEEE International Ultrasonics Symposium (IUS), Venice, Italy, 10-13 October 2022, doi: 10.1109/IUS54386.2022.9957698.

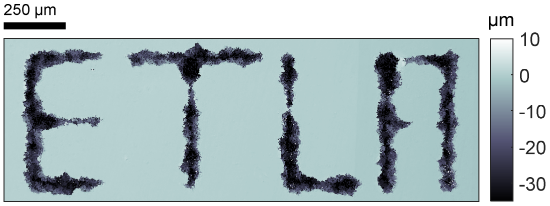

Fig. 5. SAM surface topography map of text “ETLA” engraved on aluminium with 12 MHz HIFU-induced cavitation. Engraving parameters: translational velocity 50 µm/s, 250 Hz PRF, 200 cycles, 20 passes, 33 MPa peak-positive-pressure amplitude.

intersection of lines. This can be attributed to the engraving procedure. Overlapping lines were engraved such that there was no spacing between them, i.e., line intersections received twice the sonication cycles compared to other locations. The poorly formed horizontal lines in the letter “A” can be attributed to the same mechanism; vertical lines were engraved first, likely serving as preferential bubble nucleation sites during engraving of the horizontal lines in close proximity.

From the surface topography maps micrometer-scale micropits and scratches were visible throughout the aluminium surface. This non-uniformity likely produced preferential bubble nucleation sites, potentially contributing to the non-uniformity of engraved lines. A more rigorous polishing method would improve surface uniformity, mitigating this effect. Alternatively, consistent surface roughness could facilitate cavitation uniformly. Using HIFU to initialize surface roughness before engraving calls for future research. Additionally, controlled and localized micrometer-scale surface roughening could be of interest in chemical processing, for instance for producing highly localized catalytic surfaces.

## IV. CONCLUSIONS

This work demonstrates HIFU-induced surface erosion as a viable micrometer-scale machining technology. Control over line width and depth in engraving aluminium was achieved by varying sonication parameters. Compared to existing methods, HIFU-induced cavitation provides a unique combination of advantages: it is inexpensive, non-contact, performed in water immersion, and applicable to thermally sensitive materials.

## REFERENCES

[1] M. L. Crichton, C. Archer-Jones, S. Meliga, G. Edwards, D. Martin, H. Huang and M. A. Kendall, "Characterising the material properties at the interface between skin and a skin vaccination microprojection device," Acta Biomater., vol. 36, pp. 186-194, 2016.

[2] M. Vaezi, H. Seitz and S. Yang, "A review on 3D micro-additive manufacturing technologies," Int. J. Adv. Manuf. Technol., vol. 67, pp. 1721-1754, 2013.

[3] A. A. Bojang and H.-S. Wu, "Design, fundamental principles of fabrication and applications of microreactors," Processes, vol. 8, 2020.

[4] S. Gao and H. Huang, "Recent advances in micro- and nano-machining technologies," Front. Mech. Eng., vol. 12, no. 1, pp. 18-32, 2017.

[5] D. Ensminger and L. J. Bond, Ultrasonics: fundamentals, technologies, and applications, Boca Raton, Florida: CRC Press, 2011.

[6] S. Kalpakjian and S. Schmid, Manufacturing: engineering and technology, New Jersey: Pearson Prentice Hall, 2010.

[7] L. Wijngaarden, "Mechanics of collapsing bubbles," Ultrason. Sonochem., vol. 29, pp. 524-527, 2016.

[8] K. B. Bader, E. Vlaisavljevich and A. D. Maxwell, "For whom the bubble grows: physical principles of bubble dynamics in histotripsy ultrasound therapy," Ultrasound Med. Biol., vol. 45, no. 5, pp. 1056-1080, 2019.

[9] W. J. Tomlinson and S. J. Matthews, "Cavitation erosion of aluminium alloys," J. Mater. Sci., vol. 29, pp. 1101-1108, 1994.

[10] C.-T. Hsiao, A. Jayaprakash, A. Kapahi, J. Choi and G. L. Chahine, "Modelling of material pitting from cavitation bubble collapse," J. Fluid Mech., vol. 755, pp. 142-175, 2014.

[11] E. Skorb, D. Shchukin, H. Möhwald and D. Andreeva, "Ultrasound-driven design of metal surface nanofoams," Nanoscale, vol. 2, no. 5, pp. 722-727, 2010.

[12] S. Yoshizawa, T. Ikeda, A. Ito, R. Ota, S. Takagi and Y. Matsumoto, "High intensity focused ultrasound lithotripsy with cavitating microbubbles," Med. Biol. Eng. Comput., vol. 47, no. 8, pp. 851-860, 2009.

[13] Y. Zhou and X. Wang, "Effect of pulse duration and pulse repetition frequency of cavitation histotripsy on erosion at the surface of soft material," Ultrasonics, vol. 84, pp. 296-309, 2018.

[14] A. Jayaprakash, J.-K. Choi, G. L. Chahine, F. Martin, M. Donnelly, J.-P. Franc and A. Karimi, "Scaling study of cavitation pitting from cavitating jets and ultrasonic horns," Wear, vol. 296, pp. 619-629, 2012.

[15] A. Meriläinen, J. Hyvönen, A. Salmi and E. Hæggström, "CESAM-coded excitation scanning acoustic microscope," Rev. Sci. Instrum., vol. 92, no. 7, p. 074901, 2021.

[16] J. Hyvönen, A. Meriläinen, A. Salmi, L. Hupa, N. Lindfors and E. Hæggström, "Three Megapixel Ultrasonic Microscope Imaging," in IEEE Int. Ultra. Sym., Glasgow, 2019.

[17] R. C. Preston, Output measurements for medical ultrasound, London: Springer-Verlag, 1991.

[18] J. Yin, Y. Zhang, J. Zhu and L. Lv, "An experimental and numerical study on the dynamical behaviors of the rebound cavitation bubble near the solid wall," Int. J. Heat Mass Tran., vol. 177, no. 10, p. 121525, 2021.

[19] A. V. Pandit, V. P. Sarvothaman and V. V. Ranade, "Estimation of chemical and physical effects of cavitation by analysis of cavitating single bubble dynamics," Ultrason. Sonochem., vol. 77, p. 105677, 2021.